Magnetische Eigenschaften von selbst-organisierten Nanomaterialien

von
Genevieve Wilbs

Masterarbeit im Studienfach Nanoengineering

Erstprüfer:
Prof. Dr. Claus Michael Schneider
Universität Duisburg-Essen: Fakultät für Physik
und
Peter Grünberg Institut: Electronic Properties PGI-6

Zweitprüfer:
Prof. Dr. Thomas Brückel
RWTH Aachen: Lehrstuhl für Experimentalphysik IV C
und
Jülich Centre for Neutron Science: Scattering Methods JCNS-2, PGI-4

angefertigt am
Jülich Centre for Neutron Science: Scattering Methods JCNS-2, PGI-4
Forschungszentrum Jülich

Duisburg, im September 2013

Versicherung an Eides Statt

Ich versichere an Eides statt durch meine untenstehende Unterschrift,

- dass ich die vorliegende Arbeit - mit Ausnahme der Anleitung durch die Betreuer - selbstständig ohne fremde Hilfe angefertigt habe und
- dass ich alle Stellen, die wörtlich oder annähernd wörtlich aus fremden Quellen entnommen sind, entsprechend als Zitate gekennzeichnet habe und
- dass ich ausschließlich die angegebenen Quellen (Literatur, Internetseiten, sonstige Hilfsmittel) verwendet habe und
- dass ich alle entsprechenden Angaben nach bestem Wissen und Gewissen vorgenommen habe, dass sie der Wahrheit entsprechen und dass ich nichts verschwiegen habe.

Mir ist bekannt, dass eine falsche Versicherung an Eides Statt nach § 156 und nach § 163 Abs. 1 des Strafgesetzbuches mit Freiheitsstrafe oder Geldstrafe bestraft wird.

_____ _____

Ort, Datum Unterschrift

Acknowledgements

It is a great pleasure for me to express my sincere gratitude to all members of the JCNS-2 for their warm welcome in this group and the comfortable working environment as well as their support throughout the whole time I was allowed to spend here. Additionally I want to thank several people in particular:

Prof. Dr. Thomas Brückel for offering me the opportunity to work in this very interesting field and for his support. I could profit from a rich pool of methods and knowledge within this group.

Prof. Dr. Claus Michael Schneider from PGI-6 for agreeing to take the first revision and helping me in overcoming bureaucratic obstacles. In addition I want to thank him for his valuable ideas in solving several problems.

PD Dr. Oleg Petracic for his extremely well mentoring. I deeply appreciate his patient guidance, enthusiastic encouragement and useful critiques of this work throughout the whole development process as supervisor.

Alice Klapper for familiarizing me with the subject of magnetic nanoparticles. I really appreciate her assistance concerning any arising problem.

Markus Schmitz for demonstrating how to use the AFM.

Dr. Ulrich Rücker for his assistance in operating the MBE.

Dr. Elmar Neumann from PGI-8 for the cooperation giving me access to their REM. I am grateful for his assistance and all those hours he worked overtime because of me.

René Borowski from PGI-7 for the cooperation that gave me access to the cleanroom.

Astrid Zimmermann from ZEA-3 for analyzing the oleic acid.

Franz-Josef Köhne from PGI-6 for his prompt support in magnetron sputtering.

Alexandra Steffen for initiating the cooperation with the Max-Planck-Institute for Intelligent Systems as well as her advice concerning PlotScript and Gwyddion.

Joachim Gräfe from the Max-Planck-Institute for Intelligent Systems for the cooperation that supplied me with samples covered with metal that was deposited by ion beam sputtering.

Additionally I want to thank my colleagues not only for the scientific discussions, but especially for creating such a friendly and positive working atmosphere: Paul Hering, Marcus Herlitschke, Christel Horriar-Esser, Giorgi Khazaradze, Alice Klapper, Benedikt Klobes, Barbara Köppchen, Dr. Abdelfattah Mahmoud, Thomas Müller, Jörg Perßon, Dr. Vasily Potapkin, Johannes Reim, Wilbert Röhrig, Bertold Schmitz, Markus Schmitz, Werner Schweika, Alexandra Steffen, Ronnie Simon, Xiao Sun, Pankaj Thakuria, Markus Waschk, Dr. Alexander Weber, Hailey Williamson and Paul Zakalek (I sincerely hope that I did not forget anyone…).

Finally I wish to thank my family and especially my husband Martin: Thank you so much for your support, encouragement and understanding not only during this thesis but ever since we met, I love you.

Contents

List of symbols

$<r^2>$	Mean square distance
μ	Magnetic moment
μ_0	Vacuum permeability
μ_B	Bohr magneton
μ_l	Orbital magnetic moment
μ_s	Spin magnetic moment
A	Area / Unit area
a	Lattice constant
B	Magnetic field
b	Characteristic length of Kuhn Monomers
$\vec{B}_A$; $\vec{B}_B$	Exchange field
$\vec{B}_{ext}$	External magnetic field
C_{debye}	Debye interaction
C_{Keesom}	Keesom interaction
C_{london}	London dispersion interaction
C_R	Richardson constant
d	Layer thickness
e	Electron charge
E	Free energy
E_B	Energy barrier
E_{th}	Thermal energy
F	Capillary force
g	g-factor
H	Magnetic field strength
h	Planck's constant
$\hat{H}$	Hamiltonian
$\hbar$	Reduced Planck's constant
H_A	Anisotropy field
H_E	Shift in hysteresis curve
H_N	Nucleation field
H_{sw}	Switching field
I	Current
J	Exchange integral
J_{int}	Effective interface coupling constant
J_R	Current density
K	Uniaxial anisotropy constant
k_B	Boltzmann constant

k_c	Spring constant
l	Orbital quantum number / Chain length / Azimuthal radius
L	Angular momentum / Sample length
L(x)	Langevin function
l_0	Equilibrium chain length
M	Magnetization
$\vec{M}_A$; $\vec{M}_B$	Spontaneous magnetization
m_e	Electron mass
m_l	Magnetic quantum number
m_s	Spin projection number
M_S	Saturation magnetization
n	Principle quantum number / Degeneracy
N	Number of atoms per unit volume / Demagnetizing factor / Degree of polymerization
p	Effective number of Bohr magnetons
p_0	Vapor pressure in thermodynamic equilibrium
r	Radius / Distance / Principal radius of curvature
R	Gas constant
$\vec{r}_{1,2}$	Position
S	Spin
S	Exchange stiffness
T	Temperature
t	Time
t_a	Aging time
T_a	Aging temperature
T_B	Blocking temperature
T_C	Curie temperature
T_f	Freezing temperature
T_g	Glass temperature
T_M	Morin temperature
T_N	Néel temperature
U	Energy density
u	Orientational polarizability
U_{ddSPM}	Dipole-dipole potential for SPM NP
U_{vdW}	van der Waals potential
v	Speed / Orbiting frequency of an electron
V	Particle volume
V_{cr}^{SPM}	Critical volume for superparamagnetism
V_m	Molar volume
W_A	Work function
Z	Number of electrons
z	Distance to the surface
α	Angle between antiferromagnetic magnetization and easy axis

α_0	Electronic polarizability
β	Angle between ferromagnetic magnetization and easy axis
Γ	Chain density
γ	Surface tension / Interfacial tension
ΔE	Height of energy barrier
ΔF	Force
Δp	Laplace pressure
Δz	Displacement in z-direction
ε_0	Vacuum permittivity
ε_r	Relative permittivity
θ	Angle between easy axis and magnetization
Θ	Angle between external field and ferromagnetic easy axis / Contact angle
σ_w	Wall area
τ	Relaxation time
τ_0	Attempt time
τ_{NP}	Relaxation time of superparamagnetic nanoparticles
ϕ	Angle
χ	Magnetic susceptibility / Spin part of wave function
χ_{AF}	Antiferromagnetic susceptibility
χ_{dia}	Diamagnetic susceptibility
χ_{Fi}	Ferrimagnetic susceptibility
χ_{FM}	Ferromagnetic susceptibility
χ_{para}	Paramagnetic susceptibility
ψ	Spatial part of the wave function / Angle between easy axis and external field
Ψ	Overall wave function
ω	Excluded volume parameter

List of acronyms

AF	Aniferromagnetism
AFM	Atomic force microscope
CCP	Cubic closest packed
CDM	Coupled Dipole Method
CFM	Chemical force microscopy
DE	Direct exchange
DLP	Dzyaloshinskii Lifshitz Pitaevskii theory
DM	Dzyaloshinski-Moriya exchange
EDX	Energy dispersive x-ray spectroscopy
FC	Field cooled
FCC	Face centered cubic
FFM	Frictional force microscopy
Fi	Ferrimagnet
FM	Ferromagnetism
GKA	Goodenough-Kanamori-Anderoson rules
GMR	Giant magnetoresistance
HCP	Hexagonal close packed
HRTEM	High resolution transmission electron microscope
MPMS	Magnetic property measurement system
NP	Nanoparticle
PE	Primary electrons
RKKY	Rudermann-Kittel-Kasuya-Yoshida exchange
SE	Super exchange
SE	Secondary electrons
SEM	Scanning electron microscope
SQUID	Scanning quantum interference device
TEM	Transmission electron microscope
XRD	X-ray diffraction
ZFC	Zero field cooled

List of figures

List of tables

1 Introduction

1.1. Motivation

The phenomenon of magnetism was already known by mankind at the time of Thales (640-546 B.C) when the Greeks and Romans found fragments of iron ore attracting nothing but iron [1]. Despite its fascinating properties it took up to A.D. 1000 until the Chinese found a useful application for the material as compass, and it was almost another 300 years until Petrus Peregrinus of Maricourt did some experiments providing initial knowledge of magnetism [2]. During the following centuries natural philosophers gave little consideration to the investigation of magnetism except for William Gilbert who published his famous book “De Magnete” in 1600 and is therefore often referred to as the father of magnetism [3]. As Oersted then discovered the relationship between electricity and magnetism in 1820 a revolution was launched that caused intense research [2].

This led to a huge number of applications like wireless communication or data storage alongside with a constantly rising demand for miniaturization. When common materials reached their limits a new approach called nanotechnology arose that provided new material properties due to size effects [4]. One of the best known examples for 2D nanomaterials is the giant magnetoresistance (GMR) discovered independently by Albert Fert and Peter Grünberg in 1988 which was honored with the Nobel Prize for Physics in 2007 [5] [6].

However, nanotechnology was already used in the middle ages when glass manufacturers utilized gold nanoparticles to produce red glass for church windows [7] [8]. Nevertheless, it took until 1931 when Max Knoll and Ernst Ruska demonstrated the first electron microscope that enabled researchers to view structures in the nanometer range and led to increasing research in this area [9] [10].

The combination of the phenomena of magnetism and nanotechnology opens up completely new properties like superparamagnetism or new types of spin structures. Especially magnetic nanoparticles like iron oxide are of major interest, because they can serve as building blocks for nanostructured materials. They could be used in biomedical applications like hypothermia for tumor therapy or as data storage media providing high data density. Therefore it is important to understand interactions between nanoparticles [11].

1.2. Concept

The scope of this work is the self-assembly of commercially available 20 nm iron oxide nanoparticles on the one hand and their magnetic properties and interaction on the other.

Chapter two provides general information about self-assembly and nanomagnetism. Several phenomena and interactions are presented. Additionally the properties of iron oxides are given. The third chapter introduces devices and measuring principles that are used to analyze the samples. In chapter four, as main part of this thesis, the results are shown and explained as far as possible. A summary and outlook finally concludes this thesis in chapter five.

1.3. Current state of research

Among all the opportunities that are offered by the wide range of magnetic nanotechnology, the assembly of nanoparticles upon a solid substrate is of major interest especially in two scientific branches: As shown by B. D. Terris et al. those structures could lead to a breakthrough in data storage performance and areal density [12]. On the other hand, the opportunity to build so-called 'artificial materials' that emerge new physical properties has huge potential for a broad range of applications since their behavior is neither identical to that of bulk material nor corresponding to isolated particles [13] [14].

The interactions that lead to specific arrangements of nanoparticles have been analyzed in detail for several materials, shapes and sizes. Most authors conclude that the van der Waals interaction and the dipolar interaction are the main causes for the results observed [15] [16] [17] [14] [18] [19] [20] [21].

The extraordinary properties reported for such systems are mainly caused by interactions between the particles. As explained by A. P. Guimaraes, magnetic particles transform to single domain state due to energetic reasons below a critical volume [22]. At elevated temperatures their behavior is comparable to the Langevin paramagnetism of moment-bearing atoms but with a magnetic moment 10^6 times higher which was already found by C. P. Bean and J. D. Livingston in 1959 and is therefore called 'superparamagnetism' (SPM) [23]. Later on it was shown in several studies that the switching behavior of SPM can be blocked below a so-called 'blocking temperature' [24] [25] [26] [27] [28]. Depending on the strength of interaction of single domain particles different magnetic systems can be distinguished: If there is no interaction the system is purely superparamagnetic. If the superspins are fully frustrated and random with a sufficiently strong interaction to induce collective behavior the system is referred to as 'super spin glass' (SSG). For the intermediate case with a non-negligible interaction that is not strong enough to produce any collective state the system is called 'modified SPM'. If the interaction becomes strong enough to cause domain formation similar to a ferromagnetic material, authors refer to it as 'superferromagnet' (SFM) with superspins instead of atomic spins [29] [30] [31] [32]. The mechanism that mediates this interaction is often assumed to be dipolar [33] [34] [35] [36] or RKKY [37].

Since the comprehension of these mechanisms has become quite well, several attempts have been made to tune the properties with an interacting material. Most of the researchers concentrated on a core/shell system [38] [39] [40] [41] [42] [43] [44] but there are also approaches in embedding [45], adsorption [46], capping [47] or interacting substrates [48]. It was shown by several authors that a Pt matrix can get polarized and enhance e.g. exchange interactions [49] [50] [51] [52].

2 Theoretical Background

2.1 Iron oxides

The term iron oxide summarizes sixteen different configurations of iron, oxygen and hydrogen including oxides, hydroxides and oxide-hydroxides as shown in Table 2.1 [53]. The iron oxides which are relevant for this thesis are described in detail below.

Table 2.1: *Configurations of iron oxide* ***[53]***.

Oxides	Oxide-hydroxides and hydroxides
Hematite α-Fe_2O_3	Goethite α-FeOOH
Maghemite γ-Fe_2O_3	Lepidocrocite γ-FeOOH
Magnetite Fe_3O_4 ($Fe^{II}Fe_2{}^{III}O_4$)	Akaganéite β-FeOOH
Wustite FeO	Schwertmannite $Fe_{16}O_{16}(OH)_y(SO_4)_z \cdot nH_2O$
β-Fe_2O_3	δ-FeOOH
ε-Fe_2O_3	Feroxhyte δ'-FeOOH
	High pressure FeOOH
	Ferrihydrite $Fe_5HO_8 \cdot 4H_2O$
	Bernalite $Fe(OH)_3$
	$Fe(OH)_2$
	Green Rusts $Fe_x{}^{III}Fe_y{}^{II}(OH)_{3x+2y=z}(A^-)_z$:$A^-$=$Cl^-$:$\frac{1}{2}SO_4{}^{2-}$

2.1.1 Hematite

Hematite (α-Fe_2O_3) is the most stable bulk phase of iron oxide in air and can be found in sediments and solids near the earth's surface [54]. It can also be obtained by heating maghemite to T = 770 K [55]. As powder it exhibits a blood-red color and is abundant in water why it can be applied as pigment. The compact form is blue to blue-black and shows a mirror-like metallic lustre after polishing, so it is often used for jewelry [56]. Due to its thermodynamic stability and nontoxicity in combination with a band gap of 2.2 eV, hematite nanoparticles can be utilized as catalysts, magnetic recording media, gas sensors etc. [57]. As shown in Figure 2.1 the material has a hexagonal close packed (HCP) unit cell with alternating layers of O^{2-} and Fe^{3+} along the [001] axis. The lattice constants are a = 0.5034 nm and c = 1.375 nm [19]. Its magnetic behavior depends on the temperature. Below the Morin temperature T_M = 263 K there are two antiparallel magnetic sublattices which are aligned along the c-axis, hence is antiferromagnetic. If the temperature raises, a slight canting of the moments occurs (first-order-spin-reorientation transition). This results in a small net moment due to an antisymmetric Dzyaloshinskii-Moriya interaction. Above the Néel temperature T_N = 955 K the material is paramagnetic [54] [57].

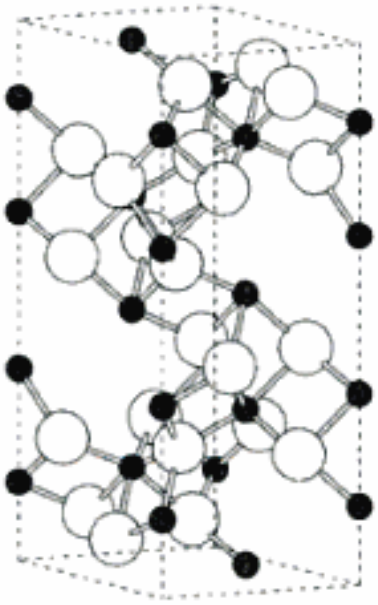

Figure 2.1: *Unit cell of hematite: White spheres represent oxygen- and black spheres iron-atoms. Image taken from* ***[53]****.*

2.1.2 Maghemite

Maghemite (γ-Fe_2O_3) is a red-brown material [58] which can be produced by calcination of magnetite at 570 K [59]. Possible applications are magnetic recording, medical applications or magnetic sensors [59]. The crystal structure can be described as inverse spinel consisting of 32 O^{2-} and $21\frac{1}{3}$ Fe^{3+} ions with a lattice constant of 0.834 nm. The oxygen atoms are arranged in eight face centered cubic (FCC) structures along the [111] direction. There are eight tetrahedral and sixteen octahedral sites. While the former are completely occupied by iron atoms, the latter are occupied by $13\frac{1}{3}$ iron atoms and $2\frac{1}{3}$ vacancies [19] as shown in Figure 2.2. The magnetic structure consists of two antiparallel sublattices. Because of the vacancies they do not completely compensate each other leading to a ferrimagnetic behavior. Above the Curie Temperature T_C = 820 K the material becomes paramagnetic [19].

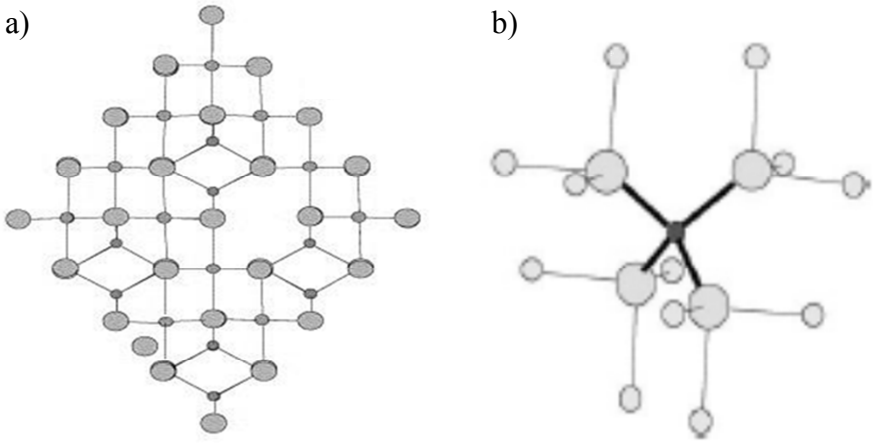

Figure 2.2: *Structure of maghemite: Large spheres represent oxygen- and small spheres iron-atoms.* ***a)*** *Projection of the lattice in the xy-plane .* ***b)*** *Surroundings of iron in a unit cell. Images taken from* ***[60]****.*

2.1.3 Magnetite

Magnetite (Fe_3O_4), also known as loadstone, is the magnetic material that has been known and used longest by mankind [2]. It is often found in rocks and has a remarkable combination of properties that make it interesting for environmental applications and spintronics [55]. In addition it is often used as pigment because of its black color and great water solubility [58]. As shown in Figure 2.3 the unit cell contains 32 O^{2-}, 8 Fe^{2+} and 16 Fe^{3+} ions forming an inverse spinel similar to maghemite: A CCP structure (a = 0.839 nm) along the [111] direction contains the oxygen ions while the divalent and half of the trivalent iron ions occupy octahedral sites. The other half of trivalent iron ions are located on tetrahedral sites [19]. Below the Curie Temperature of $T_C = 858$ K the magnetic moments of tetrahedrically and octahedrically coordinated ions are oriented antiparallel so the spins of Fe^{3+} ions cancel each other out. The remaining spin of Fe^{2+} ions results in a ferrimagnetic behaviour [61]. Besides, magnetite exhibits semi-metallic properties above the Verwey temperature $T_V = 122$ K because of the double-exchange interaction. At T_v the material undergoes a phase transition due to a charge ordering mechanism and becomes insulating below T_v [61].

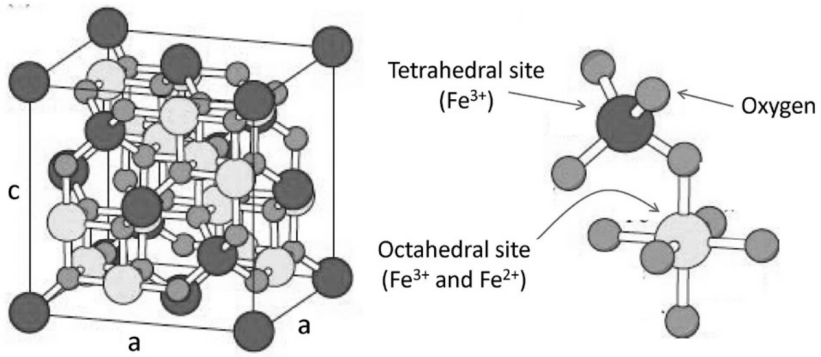

Figure 2.3: *Unit cell of magnetite: Grey spheres represent oxygen, black spheres tetrahedrically coordinated iron and white spheres octahedrically coordinated iron-atoms. Image taken from* ***[55]****.*

2.1.4 Wustite

Wustite (Fe_xO) is a black material sometimes found in rocks that is a potentially useful precursor for the preparation of other iron oxides [62]. At atmospheric pressure it is only stable above 840 K but can be quenched to room temperature leading to a metastable state [63] [64]. It crystalizes in a rock salt structure as shown in Figure 2.4 with distributed iron vacancies and a composition of x = 0.84 to 0.95 depending on temperature and pressure [62] [65]. The lattice parameter of a = 0.428 nm to 0.431 nm depends on composition [19]. If the material is cooled slowly, it disproportionates to Fe and Fe_3O_4 [63]. The magnetic behavior also depends on the temperature. Below the Néel temperature $T_N = 198$ K the spins of a layer along the [111] direction point in the same direction. They are antiparallel to the spins of the adjacent layers leading to an antiferromagnetic behavior. If the temperature is higher, the material becomes paramagnetic [65]. The conductivity is slightly temperature dependent [64].

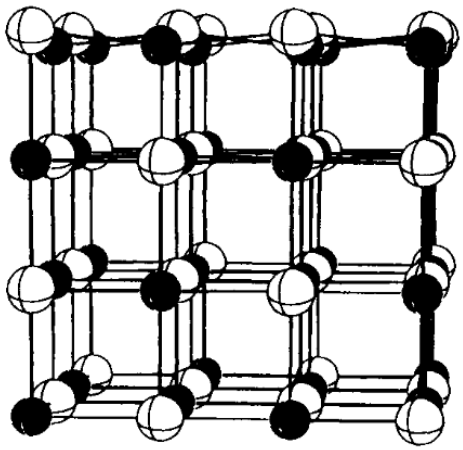

Figure 2.4: *Crystal structure of wustite: Black spheres represent iron- and white spheres oxygen-atoms. Figure taken from* ***[66]****.*

The properties of iron oxides mentioned above are summarized in Table 2.2. The additional information like saturation magnetization at 300 K, anisotropy constant and magneto-restriction constant are taken from [53].

Table 2.2: *Summary of iron oxide properties.*

	Hematite	Maghemite	Magnetite	Wustite
Color	Powder: Blood-red Compact: Blue-black	Bulk: Red-brown	Bulk: Black	Bulk: Black
Application	Pigment, jewelry, catalyst, gas sensor	Magnetic recording, medical application, magnetic sensor	Environmental application, pigment	Precursor for iron oxide preparation
Crystal structure	HCP	Inverse spinel	Inverse spinel	NaCl
Lattice constants [nm]	a = 0.5034 c = 1.375	0.834	0.839	0.428 to 0.431
Magnetic behavior	$T < T_M$ antiferromagnetic $T_M < T < T_N$ weak ferrom. $T_N < T$ paramagnetic T_M = 263 K T_N = 955 K	$T < T_C$ ferrimagnetic $T_C < T$ paramagnetic T_C = 820 K	$T < T_C$ ferrimagnetic $T_C < T$ paramagnetic T_C = 858 K	$T < T_N$ antiferrom. $T_N < T$ param. T_N = 198 K
Electric behavior	Insulator	Insulator	$T < T_V$ insulator $T_V < T$ semi-metallic T_V = 122 K	Semiconductor
Saturation magnetization at 300 K [Am^2/kg]	0.3	60 to 80	92 to 100	-
Anisotropy constant [J/m^3]	10^4 to $6 \cdot 10^4$	10^5	10^4 to 10^5	-
Magneto- restriction constant	$8 \cdot 10^{-6}$	$35 \cdot 10^{-6}$	$35 \cdot 10^{-6}$	-

2.2 Magnetism

2.2.1 Quantum numbers

In order to understand magnetism in the solid state one has to start with electrons. Their energetic state can be described using quantum numbers. The principal quantum number n describes the electron shell:

$$n = 1, 2, 3, \ldots \tag{2-1}$$

The second quantum number l is called orbital quantum number:

$$l = 0, 1, 2, \ldots, (n - 1) \tag{2-2}$$

$$l = s, p, d, f, \ldots$$

It gives the absolute value of the angular momentum L. The z-component is described by the magnetic quantum number m_l which is calculated by projecting the orbital angular momentum along the quantization axis (usually z):

$$L^2 = \hbar^2 l (l + 1) \tag{2-3}$$

$$L_z = m_l \hbar \tag{2-4}$$

$$m_l = -l, -(l - 1), \ldots, l \tag{2-5}$$

Where ħ is the reduced Planck's constant. In addition every electron carries an intrinsic angular momentum called spin S. Its projection along the quantization axis is described by the spin projection quantum number m_s.

$$S = \frac{1}{2} \tag{2-6}$$

$$m_s = \pm\frac{1}{2} \tag{2-7}$$

An atom can contain several electrons which must differ in at least one quantum number (Pauli Exclusion Principle). The consequence of this prohibition is that one orbital can carry a maximum of two electrons with opposite spins [67].

2.2.2 Magnetization

A charged particle moving in a circle represents a magnetic dipole. Its strength is described by the magnetic moment $\vec{\mu}$ which is dependent on the current I and the area $\vec{A}$ it flows around.

$$\vec{\mu} = \vec{A}\ I \tag{2-8}$$

Quantum mechanically follows:

$$\overrightarrow{\mu_l} = -\frac{g_l \mu_B \vec{L}}{\hbar} \tag{2-9}$$

$$\mu_B = \frac{e\,\hbar}{2\,m_e} \tag{2-10}$$

Where g is a dimensionless quantity called g-factor. For electrons g_e is 1, for spins it has a value of $g_s \approx 2$. The two relevant eigenvalues for $\vec{L}^2$ and L_z are $l(l+1)\hbar^2$ and $m_l\hbar$, respectively. Additionally every electron has a magnetic moment due to its spin which can be calculated analogically:

$$\overrightarrow{\mu_s} = -\frac{g_s \mu_B \vec{S}}{\hbar} \tag{2-11}$$

The eigenvalues that are relevant for $\vec{S}^2$ and S_z are s and m_s, respectively. The total angular moment of an atom $\vec{J}$ arises either from the so-called LS- or jj-coupling-scheme, depending on the atomic number. These are defined as follws:

$$\vec{J} = \vec{L} + \vec{S} \quad \text{where} \quad \vec{L} = \sum_i^N \overrightarrow{l_i} \quad \vec{S} = \sum_i^N \overrightarrow{s_i} \tag{2-12}$$

(LS-coupling)

$$\vec{J} = \sum_i^N \overrightarrow{J_i} \quad \text{where} \quad \vec{j} = \overrightarrow{l_i} + \overrightarrow{s_i} \tag{2-13}$$

(jj-coupling)

The energy of a magnetic moment in an applied field is:

$$E = -\vec{\mu} \cdot \vec{B} \tag{2-14}$$

The magnetization $\vec{M}$ of a bulk material which consists of a N atoms is calculated by the magnetic moment per unit volume V:

$$\vec{M} = \frac{\vec{\mu}}{V} \tag{2-15}$$

[19]

2.2.3 Types of magnetic behavior

Depending on the degree to which a material can be magnetized in external magnetic fields, different types of magnetic solids can be distinguished by the magnetic susceptibility χ.

$$\chi = \frac{M}{H} \tag{2-16}$$

2.2.3.1 Diamagnetism

Diamagnetism is a quantum mechanical effect observed in every material. It is often classically explained by identifying the orbital motion of electrons as circular current. An external magnetic field induces an additional current which counteracts its cause (Lenz' law). This induces a magnetic moment which is directed antiparallel to the applied field and therefore reduces it. Diamagnetism is a very weak effect that is approximately temperature independent. The diamagnetic susceptibility is negative and can be described according to Langevin:

$$\chi_{dia} = \frac{\mu_0 N Z e^2}{6 m_e} \langle r^2 \rangle \; < 0 \tag{2-17}$$

Where μ_0 is the vacuum permeability and $\langle r^2 \rangle$ the mean square distance to the nucleus. N represents the number of atoms per unit volume and Z the number of electrons [68] [69].

2.2.3.2 Paramagnetism

Materials with unpaired electrons, defects or partially filled inner shells generally possess a permanent dipole moment. If an external magnetic field is applied the magnetic moments align parallel to the field and the magnetization increases. This effect is opposed by thermal fluctuations that increase the disorder as the temperature rises. Therefore the paramagnetic susceptibility is dependent on the external field and the temperature. It is positive and defined by Curie's law:

$$\chi_{para} = \frac{Np^2\mu_B^2}{3k_BT} > 0 \quad (2\text{-}18)$$

$$p = g\sqrt{L(L+1)} \quad (2\text{-}19)$$

Where p is the effective number of Bohr magnetons and T is the temperature. k_B represents Boltzmann's constant [19] [69].

2.2.3.3 Ferromagnetism

A ferromagnetic material (FM) exhibits a long-range order where the magnetic moments are arranged parallel to each other due to a positive exchange constant. For $T > T_C$ the ferromagnetic susceptibility is described by Curie-Weiß' law:

$$\chi_{FM} = \frac{C}{T-T_C} >> 0 \quad (2\text{-}20)$$

$$C = \frac{Np^2\mu_B^2\mu_0}{3k_B} \quad (2\text{-}21)$$

Where C is the material specific Curie constant. Above the Curie temperature T_C the material becomes paramagnetic due to thermal fluctuations.

In most cases FMs can be divided into so called Weiß domains. Within every domain the magnetic moments are aligned in one direction. In between the magnetization rotates through the plane of the wall for bulk material (Bloch wall) or within the plane for layers that are thinner than the wall thickness (Néel wall), shown in Figure 2.5.

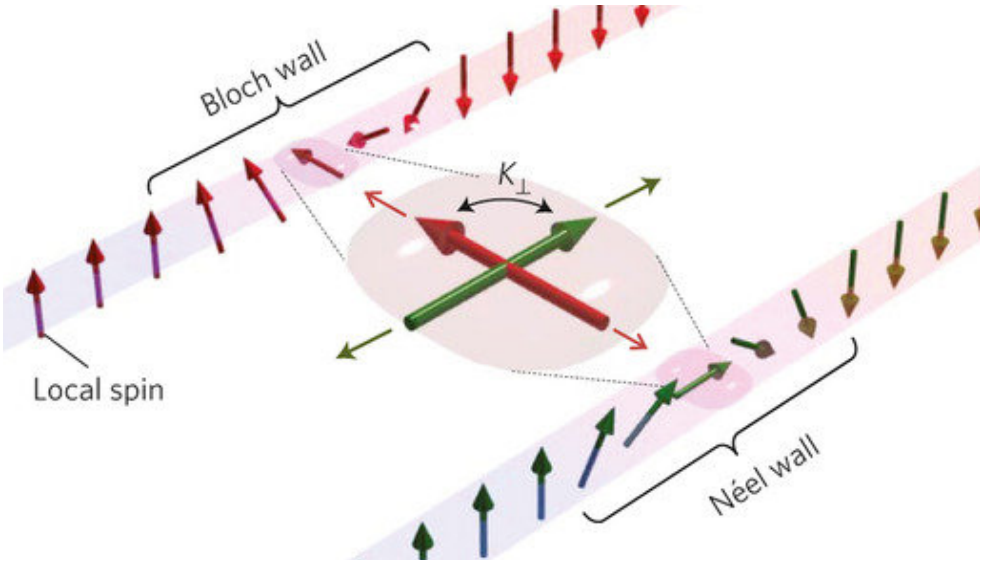

Figure 2.5: *Bloch wall and Néel wall: For the former local spins rotate through the plane of the wall, for the latter they rotate within the plane. Image taken from* ***[70]****.*

The reason for domain wall formation is the minimization of internal energy. As shown in Figure 2.6 magnetic stray fields can be reduced by domains. The energy needed to create a domain wall is called exchange energy and is proportional to the wall area:

$$\frac{\sigma_W}{A} = \pi\sqrt{SK} \quad (2\text{-}22)$$

Where A describes the unit area, S is the exchange stiffness and K is the uniaxial anisotropy. Hence a critical domain size is reached when energy loss and gain cancel each other out.

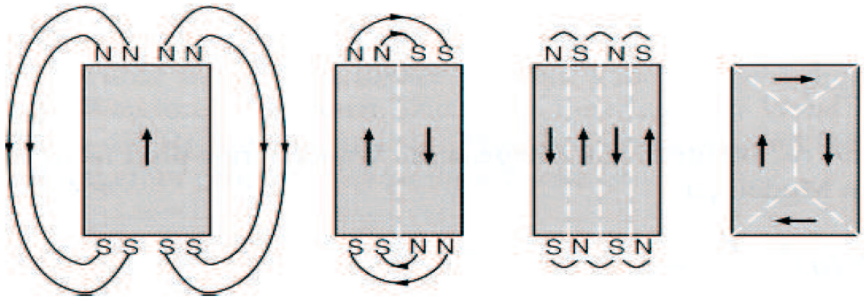

Figure 2.6: *Formation of ferromagnetic domains: The grey, magnetic material is separated into domains what is indicated by white, dotted lines. The direction of magnetization is shown by black arrows. The black lines refer to magnetic stray fields from the magnetic north pole 'N' to the magnetic south pole 'S'. Image taken from* ***[69]****.*

If an external magnetic field is applied ferromagnetic materials exhibit a hysteresis as shown in Figure 2.7a. For low field strengths energetically favored domains grow at the expense of others by reversible domain wall movement, but they are pinned at defects. By exceeding a critical value the movement suddenly continues (so called Barkhausen jumps, Figure 2.7b) and the change becomes irreversible. In addition every ferromagnetic material provides easy axes. To align the magnetic moments in a different direction energy is consumed (anisotropy energy) which can be provided by further raising the magnetic field. One should note that a hysteresis loop can also be observed *without* domain wall movement due to coherent or incoherent rotation [69] [71].

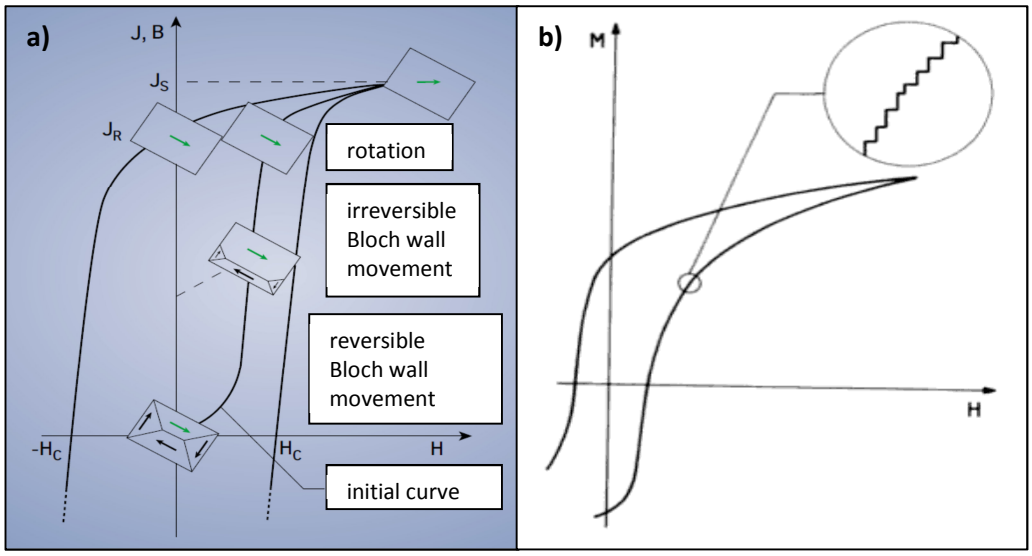

Figure 2.7: a) *Hysteresis of a ferromagnetic material: The boxes represent the sample and the arrows indicate the direction of magnetization in different domains. The green arrow points in the energetically favored direction. Figure taken from* ***[72]****.* ***b)*** *Barkhausen jumps: The hysteresis of a ferromagnetic material is shown and a small area in the region of irreversible Bloch wall movement is magnified. Image taken from* ***[73]****.*

2.2.3.4 Antiferromagnetism

Antiferromagnetic materials (AF) exhibit a negative exchange interaction resulting in an antiparallel ordering of adjacent moments. This can be described by two interpenetrating sublattices as shown in Figure 2.8. The absolute values of the magnetization are the same so there is no net moment.

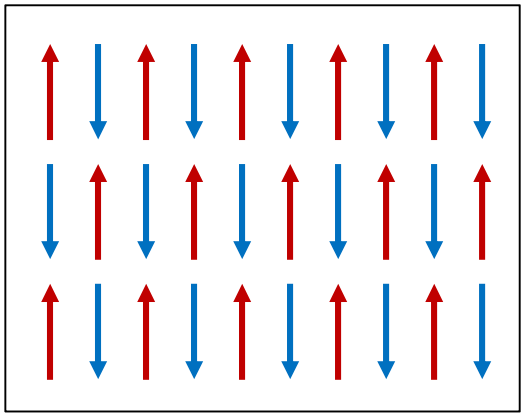

Figure 2.8: *Antiferromagnetic order: The red arrows represent spin up orientation and the blue ones spin down.*

Above the Néel temperature T_N the material becomes paramagnetic and the susceptibility can be described as follows:

$$\chi_{AF} = \frac{C}{T+T_N} \tag{2-23}$$

At 0 K the susceptibility is zero and increases continuously with rising temperatures. For very high fields the Zeeman energy can exceed the exchange interaction causing a spin-flop transition [19] [71] [74].

The temperature dependencies for different magnetic systems are summarized in Figure 2.9.

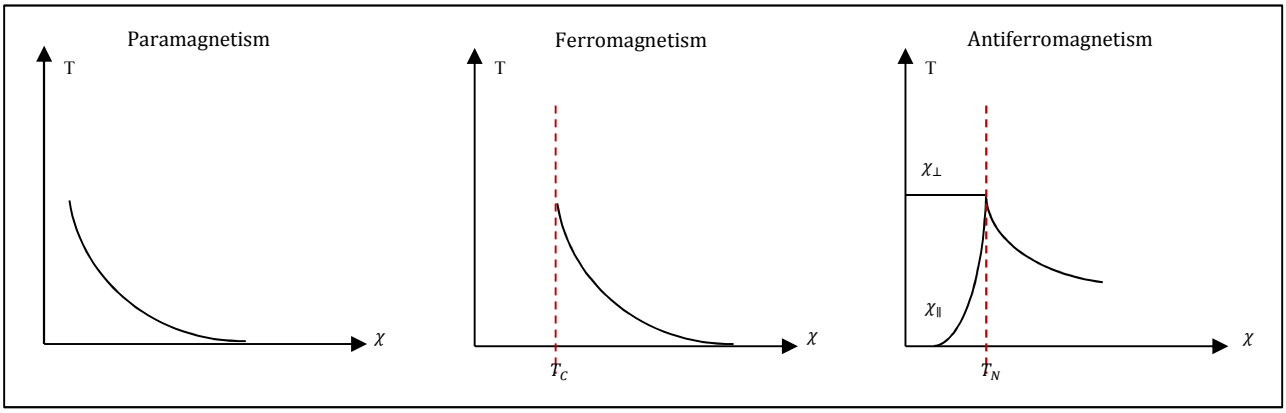

Figure 2.9: *Temperature dependency of the magnetic susceptibility for different magnetic systems. T_C is the Curie temperature and T_N the Néel temperature. $\chi_\perp$ is the susceptibility normal to the external field, $\chi_{||}$ lies parallel to it.*

2.2.3.5 Ferrimagnetism

Materials with two sublattices of antiparallel magnetic moments that do not cancel each other out are called ferrimagnetic (Figure 2.10a). A famous example is magnetite which has a spinel structure. It contains two oxidation states of iron occupying different lattice sites. While Fe^{3+} occupies octahedral and tetrahedral sites Fe^{2+} occupies octahedral sites only. For the reason that all exchange integrals (J_{oo}, J_{tt}, J_{ot}) are negative an antiparallel ordering is favorable. In addition $J_{ot} >> J_{oo}$, J_{tt} so the spins of octahedral sites are antiparallel to those of tetrahedral sites and spins of the same coordination are parallel. The result are Fe^{3+} spins that cancel each other out and Fe^{2+} spins leading to a net moment as shown in Figure 2.10b.

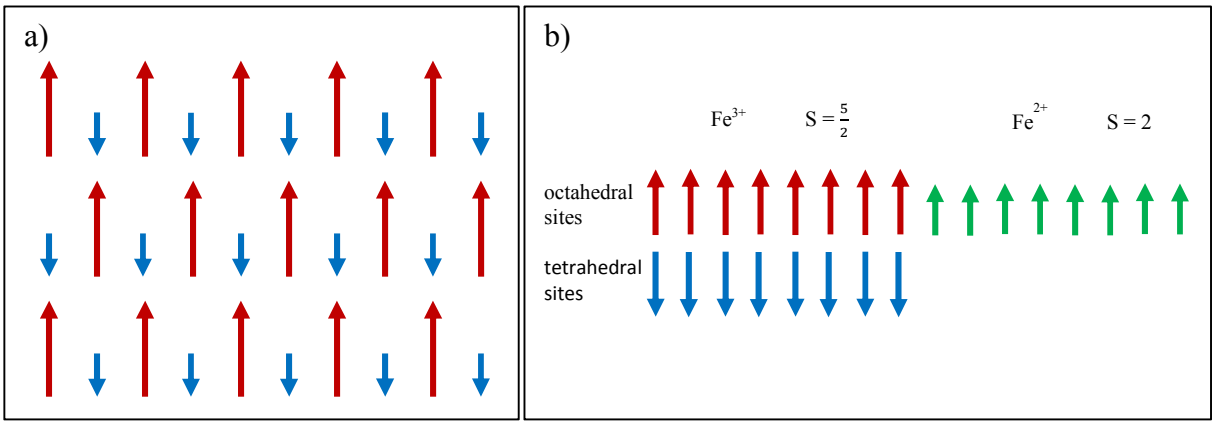

Figure 2.10: a) *Ferrimagnetic order.* ***b)*** *Ferrimagnetic order in Magnetite: The red arrows refer to the upward spins of Fe^{3+} on octahedral sites, blue ones represent downward spins of Fe^{3+} on tetrahedral sites. Green arrows are upward spins of Fe^{2+} on octahedral sites.*

Above the Curie temperature the material is paramagnetic and the susceptibility can be described using two different Curie constants for octahedral C_o and tetrahedral sites C_t:

$$\chi_{Fi} = \frac{(C_o + C_t)\,T - 2\mu C_o C_t}{T^2 - {T_C}^2} \qquad (2\text{-}24)$$

[69] [71]

2.2.3.6 Spin glasses

A spin glass can be produced by doping a nonmagnetic material with a small amount of magnetic atoms. If frustrated interactions and disorder exist, then such a system can exhibit spin glass ordering, i.e. below a critical temperature T_g a collective spin glass state is found [75].

2.3 Magnetic interactions

2.3.1 Dipole-dipole interaction

The magnetic field $\vec{B}_{Dipole}$ of a dipole $\vec{m}$ can be described as follows:

$$\vec{B}_{Dipole} = \frac{\mu_0 3(\vec{m}\ \vec{a}) - a^2\vec{m}}{a^5} \tag{2-25}$$

If a second moment is placed at a distance of interatomic spacing the interaction energy is

$$E = -\overrightarrow{\mu_B} \cdot \vec{B} \approx 3 \cdot 10^{-5}\ eV \tag{2-26}$$

which corresponds to an ordering temperature of 0.3 K. For the reason that ordering temperatures normally measure several 100 K the dipole-dipole interaction cannot be the driving force for magnetic long range order in atomic systems, though it is very important for the formation of magnetic domains and for interactions between nanoparticles [71].

2.3.2 Exchange interaction

Exchange interaction is a quantum mechanical effect that is based on the Coulomb interaction and Pauli Exclusion Principle. One distinguishes between direct and indirect exchange.

2.3.2.1 Direct exchange

Direct exchange is possible if electron orbitals overlap. Using a two electron system the exchange integral can be derived. The total spin of those electrons is represented by

$$\hat{S} = \hat{S}^a + \hat{S}^b \tag{2-27}$$

with the eigenvalues 0 for antiparallel spins and 1 for parallel spins. It leads to the degeneracy

$$n = 2S + 1 = \begin{cases} 1 & for\ S = 0 \\ 3 & for\ S = 1 \end{cases} \tag{2-28}$$

For the reason that electrons can be characterized by Fermi-Dirac-statistics and follow the Pauli Exclusion Principle they are counted among the fermions. Therefore the overall wave function Ψ consisting of a spatial part ψ and a spin part χ has to be antisymmetric. Hence, whatever the exchange symmetry of the spin wave function, the spatial part must have the opposite symmetry.

$$\Psi_S = \frac{[\psi_a(r_1)\psi_b(r_2) + \psi_a(r_2)\psi_b(r_1)]\chi_s}{\sqrt{2}} \tag{2-29}$$

$$\Psi_T = \frac{[\psi_a(r_1)\psi_b(r_2) + \psi_a(r_2)\psi_b(r_1)]\chi_T}{\sqrt{2}} \tag{2-30}$$

Where the index ‘S’ corresponds to the antisymmetric singlet state (S = 0, n = 1) and the index ‘T’ refers to the symmetric triplet state (S = 1, n = 3). ‘a’ relates to the first electron and ‘b’ to the second. r describes the position.

The exchange integral J is then calculated using the energy difference of the singlet and triplet state:

$$\mathrm{E}_S = \int \Psi_S^* \hat{\mathcal{H}}\ \Psi_S\ dr_1\ dr_2 \tag{2-31}$$

$$\mathrm{E}_T = \int \Psi_T^* \, \hat{\mathcal{H}} \, \Psi_T \, dr_1 \, dr_2 \tag{2-32}$$

$$\hat{\mathcal{H}} = \frac{1}{4} (\mathrm{E}_S + 3\mathrm{E}_T) - \underbrace{(\mathrm{E}_S - \mathrm{E}_T) S_1 S_2}_{\hat{\mathcal{H}}^{spin}} \tag{2-33}$$

$$\mathrm{E}_S - \mathrm{E}_T = 2 \int \psi_a{}^*(r_1) \psi_b{}^*(r_2) \; \hat{\mathcal{H}} \; \psi_a(r_2) \psi_b(r_1) \, dr_1 \, dr_2 \tag{2-34}$$

$$J^{DE} = \frac{\mathrm{E}_S - \mathrm{E}_T}{2} = \int \psi_a{}^*(r_1) \psi_b{}^*(r_2) \; \hat{\mathcal{H}} \; \psi_a(r_2) \psi_b(r_1) \, dr_1 \, dr_2 \tag{2-35}$$

This ansatz is adapted for a system consisting of many electrons by the so-called 'Heisenberg Hamiltonian':

$$\hat{\mathcal{H}} = -\sum_{ij} J_{ij} S_i \cdot S_J \tag{2-36}$$

Where J_{ij} is the exchange constant between spin 'I' and 'j'.

If the electrons belong to the same atom the exchange integral is positive and the triplet state is favored. This keeps the electrons apart from each other and minimizes the Coulomb energy. For electrons located on neighboring atoms bonds are formed. This allows an electron movement around both nuclei what saves kinetic energy. Molecular orbitals are formed which can be either spatially symmetric (bonding) or spatial antisymmetric (antibonding) [76] [77] [78].

2.3.2.2 Indirect exchange

For an indirect exchange process electrons travel with a certain probability from a lattice site to the next by hopping in order to lower the total energy [79].

2.3.2.2.1 Super exchange

For super exchange the electrons are assumed to occupy lattice sites that have a single energy level. This can be described by the Hubbard-Modell [79]:

$$\hat{H} = \hat{H}_t + \hat{H}_U \tag{2-37}$$

$$\hat{H}_t = -\mathrm{t} \sum_{\langle ij \rangle, \sigma} \left(c_{i\sigma}^+ \, c_{j\sigma}^- + c_{j\sigma}^+ \, c_{i\sigma}^- \right) \tag{2-38}$$

$$\hat{H}_U = -\mathrm{U} \sum_i (n_{i\uparrow} \, n_{i\downarrow}) \tag{2-39}$$

Where $\hat{H}_t$ characterizes the kinetic energy if an electron with spin σ on lattice site i moves to lattice site j by hopping. The hopping integral t > 0 is a measure for the kinetic energy gained by delocalization. $\hat{H}_U$ represents the Coulomb-Energy U needed for two electrons occupying the same lattice site.

The total energy gain is

$$J^{SE} \sim \frac{t^2}{U} \tag{2-40}$$

For U << t the system is metallic with delocalized electrons, for U >> t the Coulomb-part dominates leading to a so called Mott-Hubbard-Isolator with exactly one electron located on every lattice site.

In addition, this model can be used to explain the spin configuration. As already mentioned hopping lowers the total energy. For parallel spins hopping is not possible due to Pauli Exclusion Principle. Hence the spins arrange in an antiferromagnetic order as shown in Figure 2.11 [79].

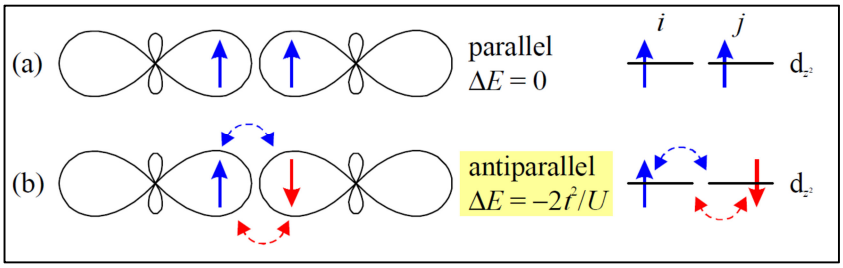

Figure 2.11: *Single level superexchange:* ***a)*** *Parallel spins cannot hop due to Pauli Exclusion Principle so there is no energy gain.* ***b)*** *For antiparallel spins hopping is possible so the energy can be reduced due to delocalization. Image taken from* ***[79].***

However, for lattice sites with two degenerated energy levels the behavior changes. The electrons can either occupy the same orbital (Figure 2.12 a,b) or different ones (Figure 2.12 c,d). The former matches the case for single level lattice sites leading to an antiferromagnetic structure. For the latter an antiparallel arrangement is disfavored by Hund's first rule so a parallel ordering is preferred (FM) [79].

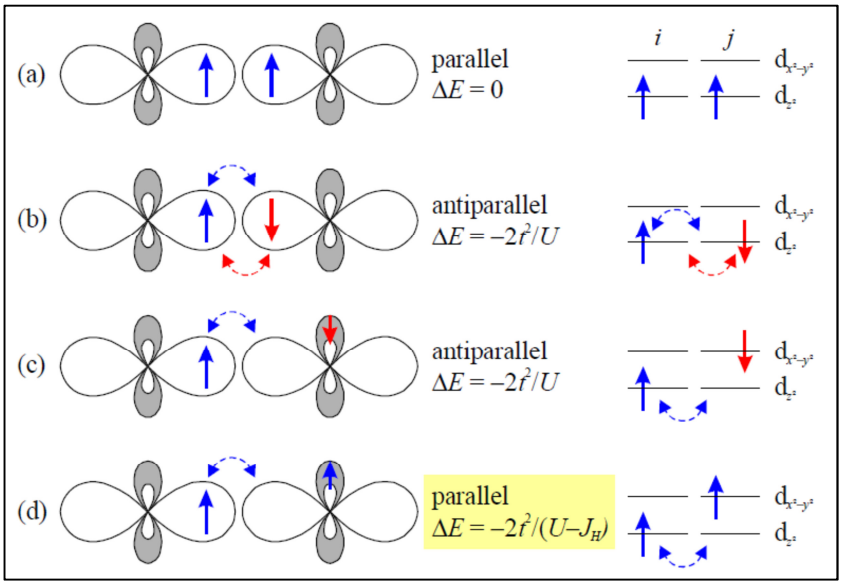

Figure 2.12: *Double level superexchange:* ***a)*** *and* ***b)*** *are identical to single level superexchange.* ***c)*** *Hopping is possible but disfavored by Hund's first rule.* ***d)*** *Hopping is possible and in agreement with Hund's first rule. The energy is reduced because of delocalization. Image taken from* ***[79]****.*

In the majority of cases this model is still too rough and the geometrical structure has to be considered. Therefore Goodenough, Kanamori and Anderson developed three simple rules for the prediction of magnetic behavior (GKA rules) [79]:

1. The 180° exchange between filled or empty orbitals is strongly AF (Figure 2.13.a,b).
2. The 180° exchange between a filled and an empty orbital is weakly FM (Figure 2.13 c).
3. The 90° exchange between filled orbitals is weakly FM (Figure 2.13 d).

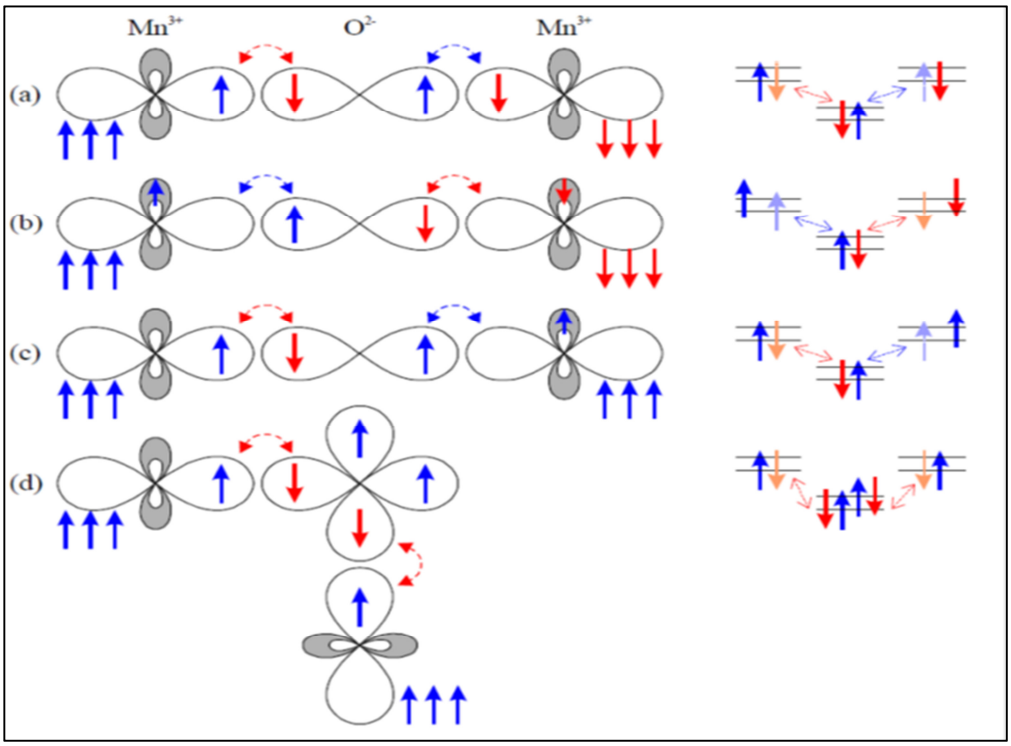

Figure 2.13: *Goodenough-Kanamori-Anderson rules: The 180° exchange between filled* ***(a)*** *or empty* ***(b)*** *orbitals is strongly AF.* ***c)*** *The 180° exchange between a filled and an empty orbital is weakly FM.* ***d)*** *The 90° exchange between filled orbitals is weakly FM. Image taken from* ***[79]****.*

2.3.2.2.2 Double exchange

For materials consisting of oxygen and metal ions in different valences double exchange can be observed. This is illustrated using $LaMnO_3$ as an example.

Mn^{3+} has three located t_{2g} core electrons and one itinerant e_g electron in a d_{z^2} orbital which is connected to a Mn^{4+} ion by an oxygen-p-orbital. For parallel core spins the e_g electron can travel across the diamagnetic oxygen ion to the M^{4+} ion without the need of excitation energy (Figure 2.14 a). For antiparallel spins the electron is not able to move because of Hund's coupling energy which has to be overcome (Figure 2.14 b). Therefore the magnetic structure is also responsible for the change in electrical conductivity at the Curie temperature (Colossal magnetoresistance) [79].

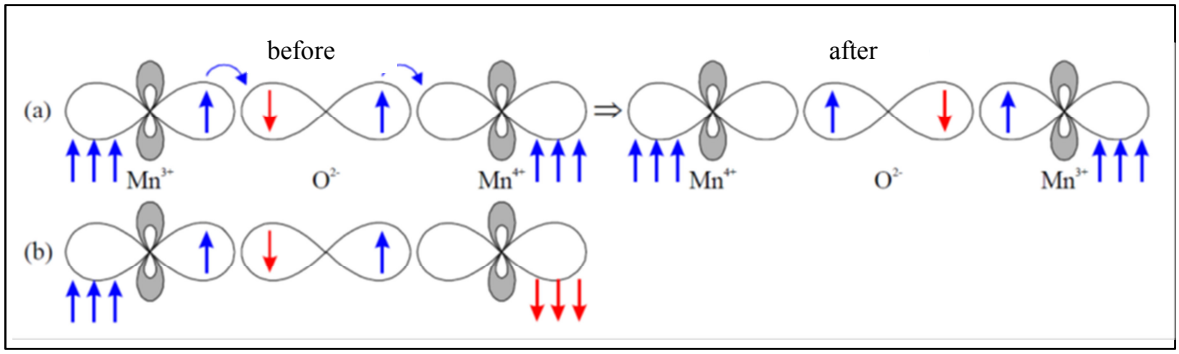

Figure 2.14: *Double exchange:* ***a)*** *For parallel core spins double exchange is possible.* ***b)*** *For antiparallel core spins not. Image taken from* ***[79]****.*

2.3.2.2.3 Dzyaloshinsky-Moriya-exchange (anisotropic exchange)

For the reason that the spin and orbital momentum of an electron interact weakly the energy level is splitted. If an electron is situated in the exited state an exchange interaction with the ground state is possible. The corresponding Hamiltonian is

$$\widehat{H}^{DM} = \mathrm{D} \cdot \overrightarrow{S_1} \times \overrightarrow{S_2} \tag{2-41}$$

For an inversion symmetric crystal field referred to the center between the vector of the magnetic ions D is zero. Otherwise D is parallel or perpendicular to the connection line of the ions. The interaction tries to arrange the spins right-angled to each other where the spins lie in a plane which is perpendicular to D. This effect is often observed in antiferromagnetics and leads to a canted arrangement. Hence a weak ferromagnetic moment which is perpendicular to the spin axis of the antiferromagnet (Figure 2.15) can be observed [19] [79] [80] [81] [82].

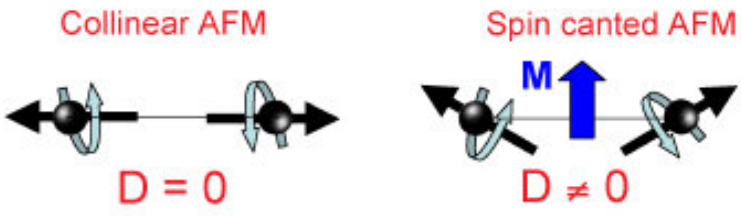

Figure 2.15: *Dzyaloshinsky-Moriya-exchange (DM): For a crystal field that is not inversion symmetric the DM interaction tries to arrange the spins perpendicular to each other leading to a canted arrangement. Image taken from* ***[83]****.*

2.3.2.2.4 Rudermann-Kittel-Kasuya-Yoshida exchange (RKKY)

The RKKY exchange interaction is observed in metallic materials where magnetic moments represent localized magnetic impurities. They couple with conduction electrons leading to a modified spatial polarization. This is noticed by the next impurity ion at a distance r resulting in the following interaction:

$$J^{RKKY} = \frac{\alpha \ cos(2k_F r)}{r^3} \tag{2-42}$$

Depending on the distance the sign changes and the interaction is either ferromagnetic or antiferromagnetic (Figure 2.16). This oscillating behavior is called Friedel-Oszillation with a wavelength given by the Fermi-wavelength:

$$\frac{\pi}{k_F} = \frac{\lambda_F}{2} \tag{2-43}$$

[79]

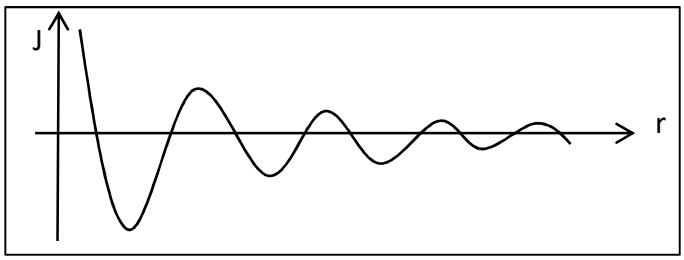

Figure 2.16: *Oscillating behavior of RKKY exchange: The exchange integral changes from positive to negative depending on the distance.*

2.4 Nanomagnetism

2.4.1 Origin

The magnetic behavior of nanomaterials (at least one dimension in the range from 1 nm to 100 nm) is very different compared to bulk material. This is primary caused by three aspects:

2.4.1.1 Characteristic lengths

Table 2.3 shows some characteristic lengths. Nanoparticles are often smaller than the critical magnetic domain size leading to a single-domain state as lowest energy configuration. Several parameters defining the magnetic properties such as the spin diffusion length, the domain wall width parameter and the exchange interaction length are also in the same order of magnitude as the particle size. This sometimes leads to extraordinary properties [22].

Table 2.3: *Typical magnitudes for some characteristic lengths in magnetism* ***[22]****.*

Length	Magnitude [nm]
Interatomistic distance (Fe)	$2.5 \cdot 10^{-1}$
Range of exchange interaction	10^{-1} … 1
Range of RKKY interaction	10^{-1} … 10
Domain size	10 … 10^{4}
Superparamagnetic critical diameter	1 … 10^{2}
Critical single-domain size	10 … 10^{3}
Domain wall width	1 … 10^{2}
Exchange length	1 … 10^{2}
Spin diffusion length	10 … 10^{2}
Electron mean free path	1 … 10^{2}
Superconducting coherence length	1 … 10^{3}
Fermi wavelength	10^{-1} … 10^{2}

2.4.1.2 Broken translation symmetry

The second aspect concerns the broken translation symmetry at interfaces. For structures with dimensions comparable to the Fermi wavelength λ_F there will be quantum confinement, so the wave character of electrons dominates and the energy E is quantized:

$$E_{quantum\ dot} = \frac{\hbar^2\pi^2}{2m_e}\left(\frac{n_x^2}{L_x^2}+\frac{n_y^2}{L_y^2}+\frac{n_z^2}{L_z^2}\right) \tag{2-44}$$

$$E_{quantum\ wire} = \frac{\hbar^2\pi^2}{2m_e}\left(\frac{n_x^2}{L_x^2}+\frac{n_y^2}{L_y^2}+\frac{n^2}{L^2}\right) \tag{2-45}$$

$$E_{quantum\ film} = \frac{\hbar^2\pi^2}{2m_e}\left(\frac{n_x^2}{L_x^2}+2\,\frac{n^2}{L^2}\right) \tag{2-46}$$

$$E_{macroscopic} = \frac{\hbar^2\pi^2}{2m_e}\left(3\,\frac{n^2}{L^2}\right) \tag{2-47}$$

Where L is the length of the sample in x, y and z direction. Without index, L describes a macroscopic value. For the reason that many physical properties are closely related to the density of states D(E) which is dependent on the energy - like the Pauli susceptibility χ_P - they change for nanomaterials.

$$\chi_P = \mu_0 \mu_B^2 D(E_F) \tag{2-48}$$

Additionally the magnetic moments of transition elements vary depending on the dimensionality of the sample.

Another effect is the reduction of the number of nearest neighbors which results in narrower electronic bands and an increasing anisotropy energy as well as a higher orbital contribution to the magnetic moment.

The last aspect concerning broken translation symmetry is the proportion of surface atoms which rises as the structure size decreases. For the reason that most catalytic procedures occur at the surface, nanomaterials become very reactive with decreasing size [22].

2.4.1.3 Dynamic behavior

The last main aspect is the dynamic behavior of the magnetization. For nanoparticles the anisotropy energy has the same order of magnitude as the thermal energy. Therefore thermal fluctuations play an important role [22].

2.4.2 Single-domain particles

For nanoparticles smaller than the critical domain size the magnetic moments are in a single domain state. Here the anisotropy energy is minimal for an arrangement parallel or antiparallel to the easy axis. These states are separated by the energy barrier E_B [22].

$$E_B = \mathrm{KV} \tag{2-49}$$

Where V is the volume of the particle. As shown in Figure 2.17a the energy barrier between the minima can be reduced by applying an external field. If the angle ψ between easy axis $\hat{n}$ and external field H measures 90° the energy levels are degenerate. For different angles one minimum becomes energetically favorable (Figure 2.17b) [22].

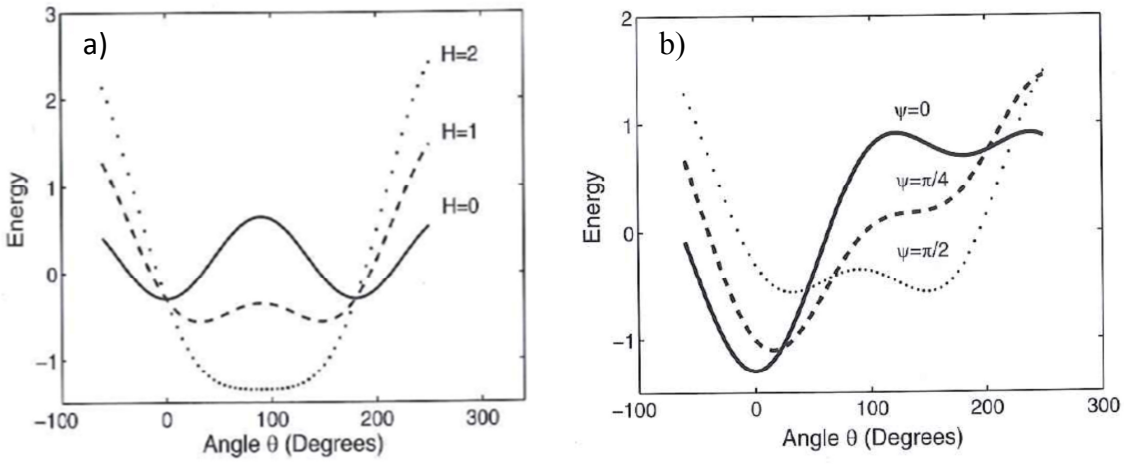

Figure 2.17: *Angular dependence of the energy* ***a)*** *for different field strength levels (ψ=90°)* ***b)*** *for different angles between easy axis and external field. Images taken from* ***[22]****.*

2.4.2.1 Stoner-Wohlfarth model

The Stoner-Wohlfarth model was developed in 1948 and describes single-domain particles as rotationally symmetric ellipsoids with the easy axis along the long axis (Figure 2.18). It is also called 'macrospin model' because it assumes a coherent reversal of atomic spins so the particles behave as if they had a single magnetic moment. The magnetization is considered to be homogenous, hence there is no exchange interaction contribution to the free energy E in presence of an external field H.

$$\frac{E}{V} = K_1 sin^2\theta + K_2 sin^4\theta - \frac{1}{2}\mu_0 N_\perp M_s^2 sin^2\theta - -\frac{1}{2}\mu_0 N_\parallel M_s^2 cos^2\theta - \mu_0 M_s H \times (cos\theta cos\psi + sin\theta sins\psi cos\varphi) \quad (2\text{-}50)$$

Where K_1 and K_2 are the first and second uniaxial anisotropy constants and θ is the angle between the easy axis and the magnetization. M_s describes the saturation magnetization and ψ is the angle between the easy axis and the external field. $N_\parallel$ and $N_\perp$ are the demagnetization factors [11] [77] [22].

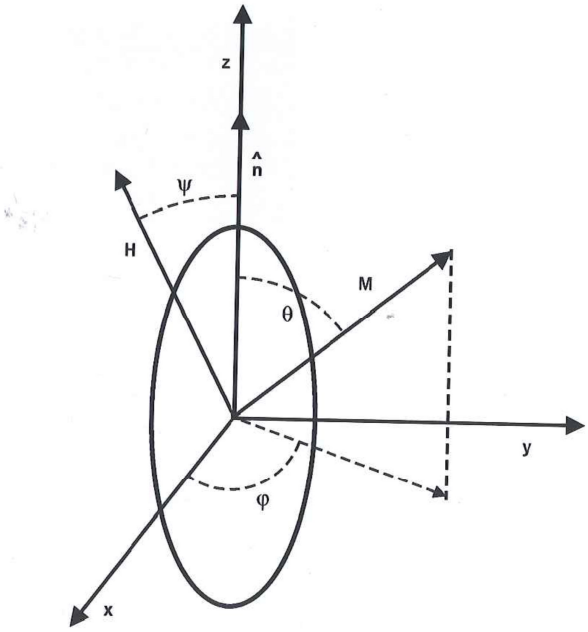

Figure 2.18: *Ellipsoidal particle in a magnetic field: The easy axis* $\hat{\boldsymbol{n}}$ *is in z-direction. ψ is the angle between the external magnetic field H and the easy axis. Θ is the angle between the magnetization M and the easy axis. φ is the angle between the projection of* $\vec{\boldsymbol{M}}$ *into the XY-plane and the x-axis. Image taken from* ***[22]****.*

2.4.2.2 Superparamagnetism

If the volume of a nanoparticle is below a critical value

$$V_{cr}^{SPM} \approx \frac{25\, k_B T}{K} \quad (2\text{-}51)$$

the thermal energy

$$E_{th} = k_B T \quad (2\text{-}52)$$

is sufficient to overcome the energy barrier. The total magnetic moment of the NP switches stochastically between two possible orientations and the net magnetic moment averages to zero. This behavior is called superparamagnetism and can be described by the Langevin function which is the classical limit of the Brillouin function. For larger particles the magnetization is stable and rotates only due to a magnetic field (Néel rotation) which is described by the Stoner-

Wohlfarth model [22]. The time scale of this stochastical reversal is given by the Neel Brown law [84]:

$$\tau_{NP} = \tau_0 exp\left(\frac{E_B}{k_B T}\right) \tag{2-53}$$

Where τ_{NP} is the relaxation time of a SPM nanoparticle and τ_0 is the attempt time. At the so-called blocking temperature T_B SPM systems exhibit a crossover from blocked behavior to isotropic superparamagnetism. It can be estimated by:

$$\tau_{NP} = \tau_{meas} \tag{2-54}$$

$$T_B = \frac{E_B}{k_B \ln\left(\frac{\tau_{meas}}{\tau_0}\right)} \tag{2-55}$$

The magnetization curve of an isotropic SPM system can be described by the Langevin function L(x). It is a limiting case of the Brillouin function B(x) for $J \to \infty$.

$$\mathrm{L(x)} = \coth x - \frac{1}{x} \tag{2-56}$$

Using this function the average assembly moment <μ> in an applied field can be derived assuming that noninteracting single-domain isotropic particles behave similar to a classical paramagnet:

$$\langle \mu \rangle = \mu \, \mathrm{L}\left(\frac{\mu H}{k_B T}\right) \tag{2-57}$$

Where μ represents the magnetic moment per particle [57] [22].

2.4.3 Exchange bias

At the interface of two different magnetic materials (FM/AF, FM/Fi, AF/Fi) an interaction is observed that leads to a shift in the hysteresis curve. This phenomenon is called exchange bias.

Depending on the structure of the antiferromagnetic material it can be compensated or uncompensated. For the former the spins of the first antiferromagnetic layer point in alternating directions, for the latter they all point in the same direction (Figure 2.19) [85].

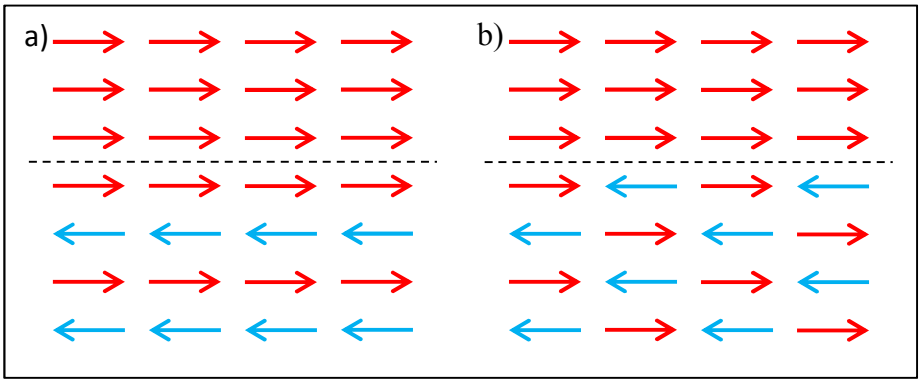

Figure 2.19: *FM/AF interface:* ***a)*** *Uncompensated: The spins at the interface point in the same direction* ***b)*** *Compensated: The spins point in alternating directions and no net interfacial moment is expected.*

For ferromagnets there are two orientations (parallel or antiparallel to the easy axis) that are energetically favorable. Due to the antiferromagnetic layer one direction is preferred. If an external magnetic field is applied the spins of the FM are forced to change their direction, but at the interface there is a local restoring force. Therefore the field needed to invert the spins is in one direction larger than in the other (Figure 2.20) [22] [86].

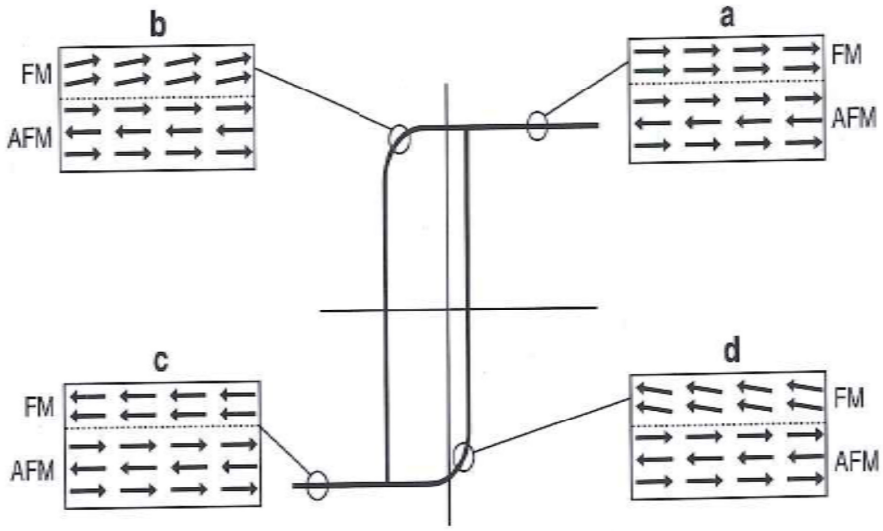

Figure 2.20: *Shifted hysteresis curve due to exchange bias:* ***a)*** *The spins of the FM layer point in the energetically favored direction.* ***b)*** *Onset of FM switching.* ***c)*** *In the saturation regime the spins of the FM layer are turned by 180°.* ***d)*** *Only a small positive field compared to b is necessary for reversal. Image taken from* ***[22]****.*

For a bilayer consisting of a ferromagnetic and an antiferromagnetic layer the energy E per unit area A is

$$\frac{E}{A} = -\mu_0 H M_{FM} d_{FM} cos(\Theta - \beta) + K_{AF} d_{AF} sin^2\Theta - J_{int} cos(\beta - \alpha) \tag{2-58}$$

Where d is the layer thickness and J_{int} is the effective interface coupling constant. α is the angle between the antiferromagnetic magnetization M_{AF} and the anisotropy axis. The angle between the ferromagnetic magnetization M_{FM} and the anisotropy axis is described by β. θ is the angle between the external field H and the ferromagnetic anisotropy axis. The shift in the hysteresis curve H_E can be obtained using the minimal energy.

$$\mathrm{H}_E = \frac{J_{int}}{M_{FM} d_{FM}} \tag{2-59}$$

Hence $M_{FM} d_{FM}$ has to be larger than J_{int} to observe the effect of exchange bias. Additionally there are several phenomena like an increase in coercivity. This is caused by short-range order fluctuations in the AF producing an additional uniaxial anisotropy. The larger the antiferromagnetic anisotropy the less effective is the ferromagnetic coupling and the ferromagnetic magnetization turns more easily.

Furthermore the shift in the hysteresis becomes less with every measurement due to changes in the antiferromagnetic domains with every rotation (training effect). Besides there is also a so called 'blocking temperature'. If the temperature is higher there is no exchange bias observable. Usually this exchange bias blocking temperature is approximately at the Néel temperature or below [22].

2.5 Self-assembly

The spontaneous arrangement of building blocks, known as self-assembly, is often found in nature (galaxies, clouds, micelles etc.). It is a very interesting approach for the fabrication of nanodevices due to its flexibility and low costs compared to other techniques [19]. It is caused by several interactions which will be discussed below.

2.5.1 Van der Waals interaction

The van der Waals interaction summarizes three different interactions between atoms, molecules or particles at a very short distance r (∝ nm).

The Keesom interaction U_{Keesom} is the polarization of a permanent dipole moment by another permanent dipole.

$$U_{Keesom} = -\frac{u_1^2 u_2^2}{3(4\pi\varepsilon_0\varepsilon_r)^2 k_B T r^6} \tag{2-60}$$

Where u is the orientational polarizability of dipole 1 and 2. ε_r describes the relative permittivity and ε_0 is the vacuum permittivity. Additionally a permanent dipole moment can induce a dipole moment in neighboring atoms leading to the Debye interaction U_{Debye}.

$$U_{Debye} = -\frac{u^2 \alpha_0}{3(4\pi\varepsilon_0\varepsilon_r)^2 k_B T r^6} \tag{2-61}$$

Where α_0 is the electronic polarizability of the non-polar atom. U_{London} refers to the London dispersion interaction. Due to thermal fluctuations every atom exhibits an instantaneous dipole moment which averages to zero over time. Nevertheless it induces a dipole moment in its neighboring atoms leading to a weak attractive interaction:

$$U_{London} = -\frac{3\alpha_0^2 h v}{4(4\pi\varepsilon_0)^2 r^6} \tag{2-62}$$

Where h is Planck's constant and v is the orbiting frequency of the electron [19] [20] [21].

2.5.2 Magnetic interaction

As shown in chapter 2.3.1 there is a dipole-dipole interaction between magnetic moments. For single domain particles the spins can be summed up to one 'superspin' $\mu = 10^3 - 10^5\ \mu_B$ (chapter 2.4.2). In the superparamagnetic regime thermal fluctuations become relevant (chapter 2.4.2.2) and have to be considered, hence the total interaction U_{dd} is:

$$U_{dd} = U_{dd}^{stat} + U_{dd}^{fluc} \tag{2-63}$$

$$U_{dd}^{fluc} = -\frac{1}{3k_B T}\left(\frac{\mu_1\mu_2}{4\pi\mu_0 r^3}\right)^2 \tag{2-64}$$

Where U_{dd}^{stat} is the static dipole-dipole interaction described in chapter 2.3.1 and U_{dd}^{fluc} is the dipole-dipole interaction due to thermal fluctuations. For the reason that this interaction is directional, nanoparticles tend to form chains or rings if it dominates [19].

2.5.3 Steric repulsion

As shown in chapter 2.5.1 and 2.5.2 there are attractive forces between nanoparticles which cause agglomeration to minimize the surface energy. This can be avoided by steric repulsion:

One end of a polymer or ligand chain is attached on the surface of the particles while the other is left free. The free energy E is then calculated as follows:

$$E(l) = \frac{\pi^2 k_B T\, \Gamma l_0^2}{6Nb^2}\left[\frac{1}{2}\left(\frac{l_0}{l}\right) + \frac{1}{2}\left(\frac{l}{l_0}\right)^2 - \frac{1}{10}\left(\frac{l}{l_0}\right)^5\right] \tag{2-65}$$

$$l_0 = N\left(\frac{12\,\Gamma b^5 \omega}{\pi^2}\right)^{\frac{1}{3}} \tag{2-66}$$

Where l is the length of the chains and l_0 the equilibrium length. Γ describes the chain density and N is the degree of polymerization. b is the characteristic length of the Kuhn monomers[1] and ω the excluded volume parameter.

Upon compression the free energy rises because of increasing osmotic pressure between the chains. Hence they tend to stretch and the nanoparticles get a brush-like surface (Figure 2.21) which avoids agglomeration [87].

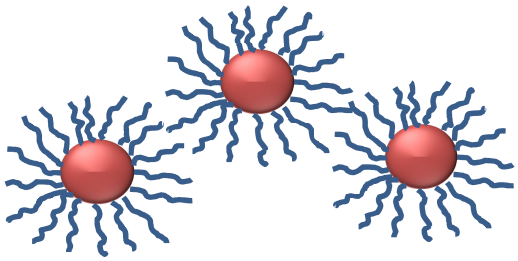

Figure 2.21: *Steric repulsion: Polymers or ligand chains (blue) are attached on the surface of the particles (red) leading to a brush-like structure which avoids agglomeration.*

2.5.4 Capillary forces

Two solids at a short distance which are connected by a fluid exhibit strong adhesion. The forces causing this effect were first examined for liquids which rise against gravity in a capillary. Therefore they are called capillary forces. For evaluation three fundamental equations are needed:

The pressure difference across a curved, liquid surface is described by the Young-Laplace equation (2-68). Inside a liquid every molecule is surrounded by a certain number of neighbors which is reduced at the surface. So the tangential and normal forces acting on such a molecule are not equal leading to a net tangential pressure which contracts the surface. This is called surface tension σ.

$$\sigma = \int_{-\infty}^{+\infty} [p_N - p_T(z)]dz \tag{2-67}$$

$$\Delta p = \sigma\left(\frac{1}{r_1} + \frac{1}{r_2}\right) \tag{2-68}$$

[1] Segments of an ideal chain described by the random walk model

Where p describes the normal (index 'N') and tangential (index 'T') pressure. r_1 and r_2 refer to the principal radii of curvature and Δp is the Laplace pressure. z is the distance z to the surface.

The dependency of the vapor pressure p on the curvature is described by the Kelvin equation (2-69). The more curved a surface the higher the vapor pressure. So the molecules of a drop can evaporate easier than those in a film.

$$RT\ ln\left(\frac{p_0^k}{p_0}\right) = V_m\sigma\left(\frac{1}{r_1}+\frac{1}{r_2}\right) \tag{2-69}$$

Where R is the gas constant and V_m the molar volume of the liquid. p_0^k and p_0 refer to the vapor pressure of the curved and flat surface in thermodynamic equilibrium.

The third fundamental relation is Young's equation (2-70) which describes the wetting phenomenon. As shown in Figure 2.22 a liquid drop on a solid forms a wetting line, where three phases (liquid, solid, vapor) are in contact.

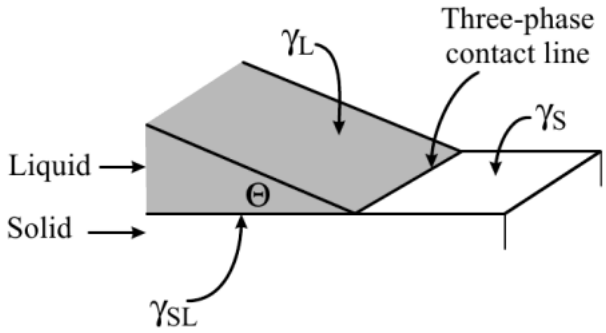

Figure 2.22: *Three-phase contact line (wetting line) of a liquid drop (grey) on a solid surface (white) surrounded by vapor.* $\boldsymbol{\gamma_L}$ *is the surface tension of the liquid-vapor interface.* $\boldsymbol{\gamma_S}$ *refers to the solid-vapor interface and* $\boldsymbol{\gamma_{SL}}$ *to the solid-liquid interface. Image taken from* ***[88]****.*

The contact angle Θ only depends on the interfacial tensions γ:

$$\gamma_L\ cos\Theta = \gamma_S - \gamma_{SL} \tag{2-70}$$

Where the index 'L' refers to the liquid-vapor interface, 'S' to the solid-vapor interface and 'SL' to the solid-liquid interface [89] [88] [90].

Around the contact area of a solid sphere with a plane or another sphere a narrow slit is created. If a small amount of a liquid is added, a meniscus is formed as shown in Figure 2.23 which causes an attractive force due to surface tension and Laplace pressure.

The total capillary force is

$$F = 2\pi l\gamma_L - \pi l^2\Delta p \tag{2-71}$$

Where l is the azimuthal radius [88].

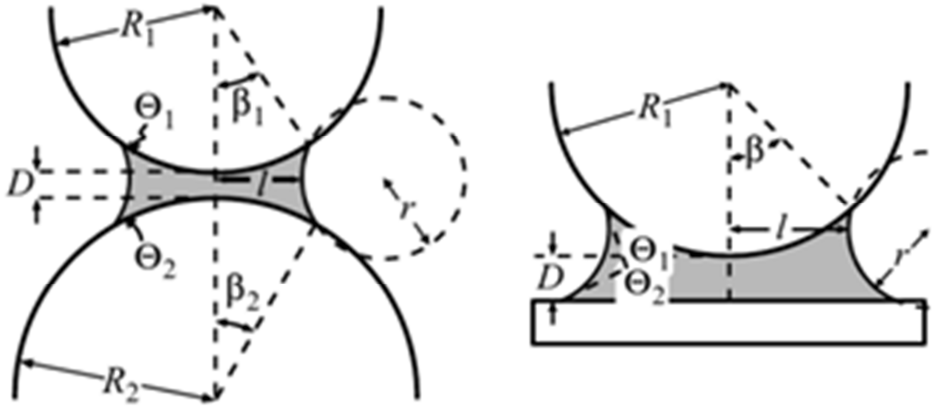

Figure 2.23: *Meniscus formation between two bodies: R_1 refers to the radius of the upper sphere, R_2 to the lower. l is the azimuthal radius. D is the distance between the upper and lower solid. β_1 and β refer to the angle between the edge of the meniscus and the connection line of the center of the upper sphere and the center of the meniscus. β_2 refers to the lower sphere. Θ_1 is the contact angle between the upper solid and the liquid, Θ_2 refers to the lower solid. r is the radius of a circle drawn at the edge of the meniscus. Image taken from* ***[88]****.*

2.5.5 Entropy

Even though entropy is usually regarded as the driving force for disorder it can be responsible for nanoparticle assembly. In a colloid with a high number concentration of particles they may arrange to a cavity. Like that the available volume is reduced what is entropically unfavorable. Therefore the arrangement is transformed to an ordered phase that provides a larger 'free' volume to maximize the entropy [87] [91].

2.5.6 Other forces

There are several forces that can also affect the assembly of nanoparticles like molecular surface forces or electrostatic interaction. For the reason that they are only slightly relevant for this thesis they are not discussed in detail.

The electrostatic interaction is a directional force which can be attractive or repulsive depending on the sign of the charge. It is interesting for the assembly of nanostructures due to its controllability through the solvent, its concentration and chemical properties [87].

The term molecular surface force comprises several short-range attractive forces like dipolar interaction, hydrogen bonding, covalent bonds or donor-acceptor interaction. They are often applied for the functionalization or stabilization of nanoparticles [87].

3 Instruments

3.1 Atomic force microscope

The atomic force microscopy (AFM) is a surface sensitive technique to determine the structure and morphology of a sample, developed in 1986 by Binning, Quate and Gerber. It excels by its possibility of measuring inter- and intramolecular forces with molecular resolution or manipulating single molecules.

The AFM belongs to the family of scanning probe microscopy (SPM) techniques. Its probe is a fine tip mounted on a cantilever which scans the surface of the sample. The measuring arrangement is shown in Figure 3.1. A laser is focused on the end of the cantilever. The light is deflected in different angles depending on the cantilever bending which is in turn depending on the height profile. Using a mirror the beam is then transmitted to a photodiode.

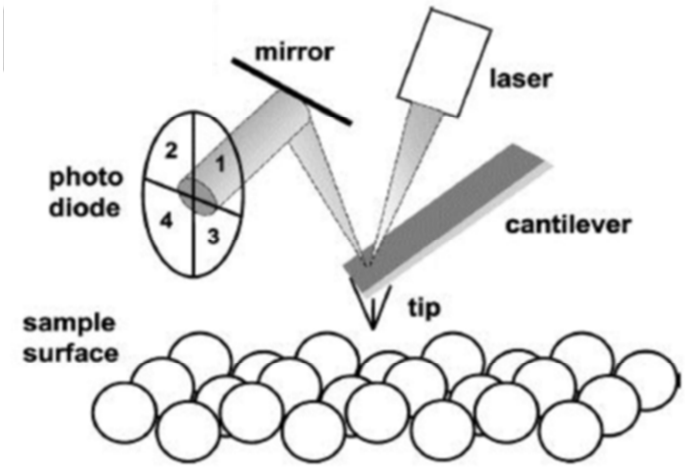

Figure 3.1: *AFM imaging: A fine tip is mounted at the edge of a cantilever and scans the sample surface. A laser is focused on the back of the cantilever and reflected towards a mirror which directs the beam towards a photo diode. Image taken from* ***[92]****.*

According to the strength of deflection a brightness value is assigned to every point in the XY-plane of the sample leading to a false color image of the surface. To avoid damage the cantilever movement normal to the sample (z-direction) is detected and manipulated by a feedback loop. The 3D movement is provided by piezoelectric actuators. The force acting on the cantilever ΔF can be obtained using Hook's law:

$$\Delta z = \frac{\Delta F}{k_c} \tag{3-1}$$

Where Δz is the displacement in z-direction and k_c the spring constant. Depending on the properties which shall be observed three different scanning modes are possible:

In contact mode the force between the tip and the surface which is proportional to the cantilever bending is held constant, so the tip is in physical contact with the surface. This is only possible for hard, solid samples which are not damaged by the tip. Due to friction cantilever torsion can occur which is measured by the photo detector. This is called frictional force microscopy (FFM).

Additionally the tip can be modified by functional groups. For the reason that similar groups show greater intermolecular interaction than chemically different ones higher friction can be observed. This delivers information about the chemical composition why it is called chemical force microscopy (CFM).

To avoid the destruction of soft samples another principle called tapping mode is used. The cantilever is moved into oscillation with a frequency of 50 kHz to 500 kHz (in air). Upon contact with the surface the oscillation amplitude is drastically reduced which is used to measure the surface topology and control the distance to the surface. Simultaneously a phase image can be generated. Differences in material properties like hardness, flexibility or surface adhesion lead to a phase shift between cantilever oscillation and vibratory excitation. Like that the mapping of several surface properties is possible. Additionally it can be used for contrast enhancement.

The third technique is the non-contact mode in which the tip scans the surface at a certain distance where attractive forces like van der Waals interaction dominate. The force is measured by the resonance frequency shift, the amplitude or the phase shift of the cantilever. This method is advantageous because of its high sensitivity and low power transmission [92].

3.2 Scanning electron microscope

The scanning electron microscope (SEM) is a device which produces images of a sample with a resolution in the nanometer range using a focused electron beam. It consists of an electron gun which provides the electrons, an electro-optical system to focus them and a detector with an image processing system. The samples have to be conductive due to the impinging electrons. Furthermore the chamber should be evacuated to avoid scattering [93].

The electron gun can be designed for field emission, thermal emission or Schottky emission. For the reason that the latter is the most common method and is also applied in the FEI Magellan 400 SEM that is used for this thesis, it is the only one explained in detail. It consists of a single crystalline tungsten wire ({100} planes perpendicular to the wire axis) that is etched down to a tip at one end and spot-welded to a polycrystalline tungsten wire at the other. The latter is fixed to two poles that are embedded in a cylindrical ceramic base. To reduce the work function a ZrO_x reservoir is attached. To enable the electrons to overcome work function the emitter is heated up to a temperature of approximately 1800 K [94].

The electro-optical column is shown in Figure 3.2. It consists of several pairs of electro-optical lenses (electrostatic or electromagnetic) which allow two-dimensional electron deflection. The beam is centered inside the pillar by the first pair of inductors. Afterwards its diameter is reduced by condenser lenses which also set the magnification. Marginal rays are suppressed by a mechanical lens opening (50 µm – 100 µm). To perform a raster scan several deflectors are used. An underlying probe forming lens reduces the beam-diameter again. Finally a set of focus- and stigmator inductors level distortions [93].

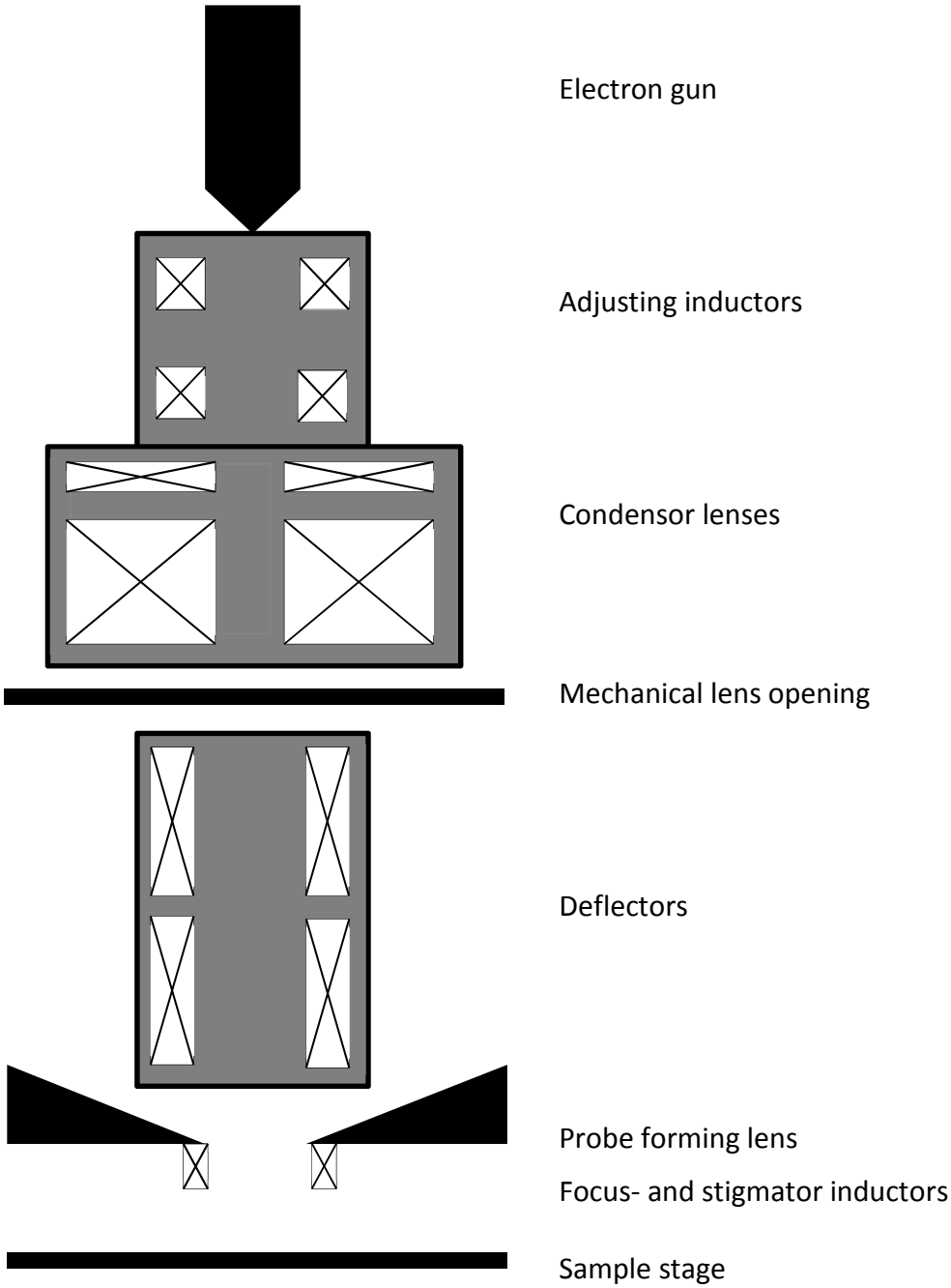

Figure 3.2: *Principal set-up of an electron optical column: Between the electron gun and the sample holder several electro-optical lenses are mounted to focus the electron beam and set the magnification.*

When primary electrons (PE) which were emitted by the electron gun hit the sample secondary electrons (SE) are created by inelastic collision. They are able to overcome the material dependent work function because of high energy impact. They leave the solid and hit a positive charged collector grid which is mounted above the sample stage. The signal is intensified by a video amplifier and an image tube creates a synchronous display of the sample [93].

3.3 Magnetic property measurement system

The magnetic property measurement system (MPMS) is a magnetometer which is used for the measurement of very small magnetic moments. The general setup is shown in Figure 3.3 and can be divided into the superconducting components (blue), the sample space and temperature control.

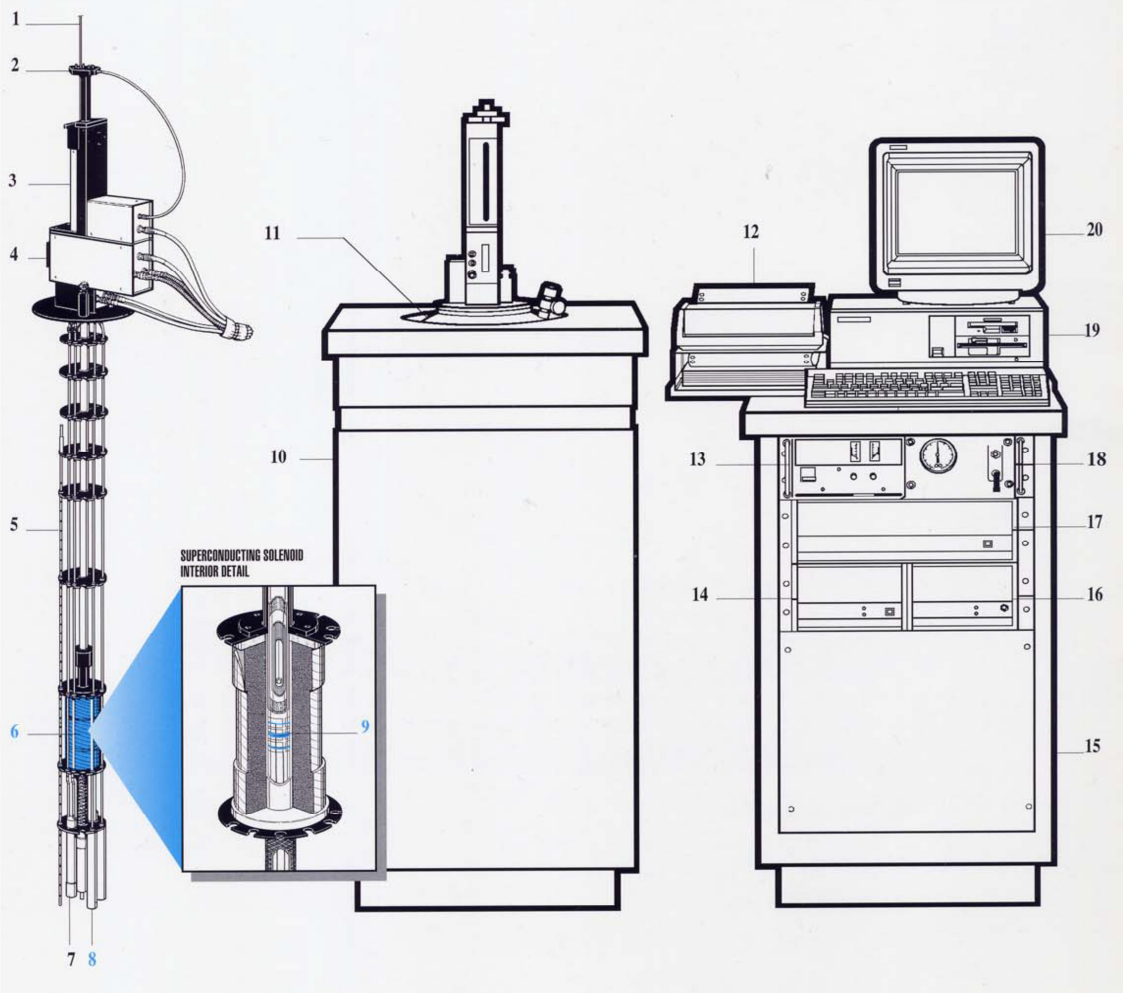

Figure 3.3: *General MPMS setup:* ***1)*** *Sample rod* ***2)*** *Sample rotator* ***3)*** *Sample transport* ***4)*** *Probe assembly* ***5)*** *Helium level sensor* ***6)*** *Superconducting solenoid* ***7)*** *Flow impedance* ***8)*** *SQUID capsule with magnetic shield* ***9)*** *Superconducting pick-up coil* ***10)*** *Dewar isolation cabinet* ***11)*** *Dewar* ***12)*** *Printer* ***13)*** *Magnet power supply* ***14)*** *Temperature controller* ***15)*** *Console cabinet* ***16)*** *Power distribution unit* ***17)*** *MPMS controller* ***18)*** *Gas/magnet control unit* ***19)*** *Computer* ***20)*** *Monitor. Image taken from* ***[95]****.*

The sample space is a tube with an inside diameter of 9 mm. It is maintained with static helium gas at low pressure and lined with copper to provide high thermal uniformity. The sample is mounted on a rod-like sample holder which is moved into the sample space through a lip seal by a stepper-motor-controlled platform. It is then pulled through the detection coil.

There are several superconducting parts that show (even for large amounts of electrical current) no energy dissipation in the form of heat. One of them is a superconducting magnet that forms a completely closed loop in a solenoidal configuration[2]. Like that it can be operated in persistent

[2] Coil wound into a tightly packed helix

mode[3]. To open the loop for charging or discharging a current switch is applied by a small heater wrapped around a short segment of the superconducting wire. If the temperature is raised the area is no longer superconducting and the loop is open. To change the current a power supply at each side of the switch is used.

In the center of the magnet a superconducting detection coil is placed. It is designed as a second-order gradiometer: As shown in Figure 3.4 it consists of a superconducting wire which is wound once anticlockwise, two times clockwise and again one time anticlockwise. Like that, noise in the detection circuit due to fluctuations in the magnetic field of the superconducting magnet or background drifts in the SQUID due to relaxation in the magnetic field can be reduced.

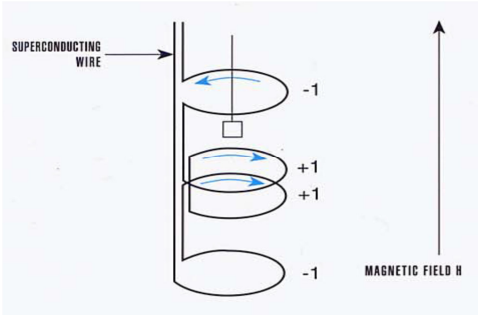

Figure 3.4: *Second-order gradiometer: A superconducting wire is wound once anticlockwise, two times clockwise and again one time anticlockwise to form a superconducting detection coil. Image taken from* ***[95]****.*

The core module of the MPMS is a superconducting quantum interference device (SQUID). As the sample is pulled through the detection coil a current is inductively generated. It flows through superconducting wires to the SQUID sensor. There the current induces a flux which flows into the superconducting ring. Due to the Josephson effect it can only be coupled in in a quantized form, hence not the whole flux is used.

For the measurement procedure the so-called 'RF-SQUID-technology' is applied. Therefore the SQUID ring is used as nonlinear element of an oscillator circuit. Thus the signal of the pick-up coil is enhanced. This signal is then plotted as induction voltage against the position what is called response curve (Figure 3.5). Afterwards the curve is fitted on the theoretical curve of a single dipole. The magnetic moment m(T,H) is one of the fit-parameters [95].

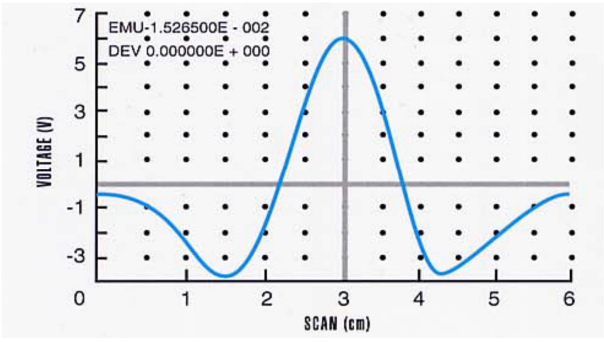

Figure 3.5: *SQUID response as a magnetic dipole is moved through the superconducting detection coil: The voltage measured by the SQUID changes for every scan position. Figure taken from* ***[95]****.*

[3] Operation at a constant current without external power supply or current source

3.4 Metal deposition

Due to instrumental conditions different deposition techniques had to be applied:

To deposit gold and platinum a magnetron sputtering process was applied at the PGI-6 in Jülich. Glow discharge plasma generates energetic ions that bombard a target in front of it. This leads to the removal of target atoms that condense on the sample as a thin film. Thereby secondary electrons are generated that maintain the plasma. Their motion is constrained to the vicinity of the target by a magnetic field parallel to the target surface. It is produced by magnets positioned in a specific way: A ring of magnets along the target edge forms one pole, a magnet placed at the central axis of the target forms the other. Like that, the probability of an ionizing collision between an electron and an atom is increased, hence the plasma becomes denser in the target region and the ion bombardment is raised [96].

Palladium was deposited by molecular beam evaporation in a UHV chamber at the JCNS-2 in Jülich: A tungsten cathode is heated until the thermal energy is sufficient to allow electrons to overcome work function and leave the solid. They are accelerated by a high voltage source and directed towards the target by an electromagnet. The Target heats up and evaporates. The material is deposited on a sample situated above the target while the layer thickness is measured using a quartz oscillator. Ultra-high vacuum (UHV) is provided by a rotary vane pump and a turbo pump [97].

Thanks to cooperation with the Max-Planck-Institute in Stuttgart Ion beam sputtering (IBS) could be used to deposit niobium: An ion source consisting of a cathode and an anode that are positioned parallel to each other generates a focused ion beam. Therefore a high voltage field is applied to the anode what creates an electrostatic field inside the ion source. Hence the electrons are confined around a saddle point in the middle of the source. As argon gas is injected, it is ionized by the high electric field and plasma arises. The ions are accelerated towards the target by the cathode. Due to momentum transfer the target material is then sputtered onto the sample [98].

4 Results and discussion

4.1 Samples

By now there are several routes available to produce magnetic nanoparticles with a narrow size distribution such as sonochemical reactions, microemulsions, sol-gel synthesis, thermolysis or hydrolysis of precursors, electrospray synthesis, hydrothermal reactions or flow injection synthesis [99].

For this thesis commercially available iron oxide nanoparticles with a diameter of 20 ± 2.5 nm and a spherical shape from Ocean NanoTech LLC were used (Appendix A). They were synthesized by thermolysis of an iron precursor in presence of oleic acid and dispersed in toluene.

The oleic acid ($CH_3(CH_2)_7CH=CH(CH_2)_7CO_2H$) is a long-chained molecule with a C18 tail. It has a cis-double-bond in the center leading to a kink (Figure 4.1). On the surface of an iron oxide nanoparticle it forms a dense monolayer which avoids aggregation (steric stabilization, Figure 2.21). The average diameter of functionalized nanoparticles is thereby increased by 0-5 nm. The saturation magnetization remains unchanged [100] [101].

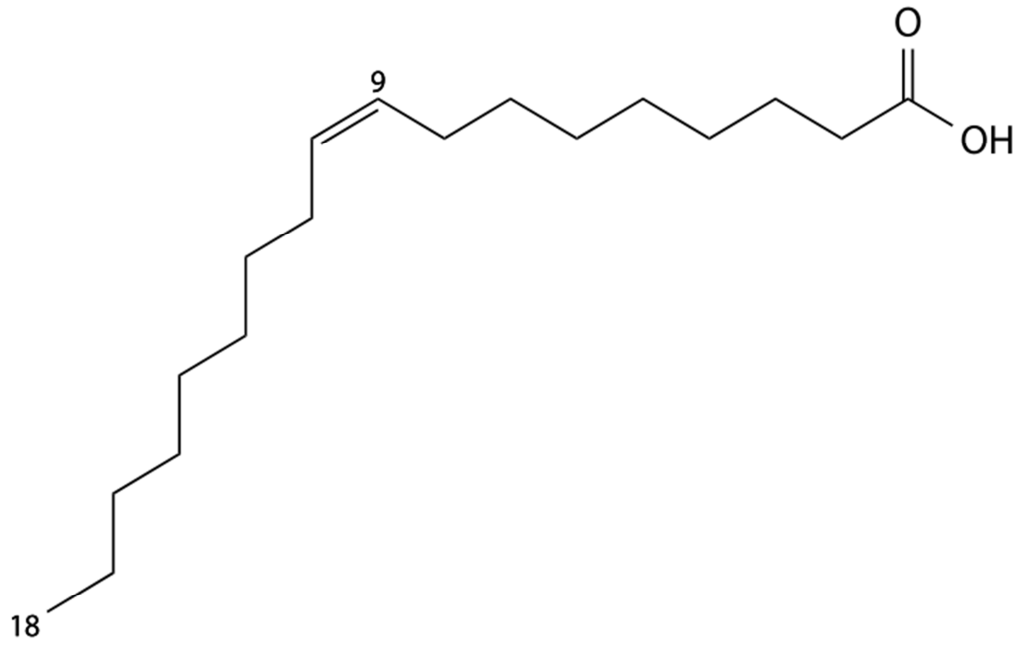

Figure 4.1: *Chemical structure of oleic acid.*

The colloid was transferred on silicon wafers by different deposition routes. Afterwards a sub-monolayer of nanoparticles was produced and the oleic acid was removed by two distinct approaches. Finally, metals were deposited using several methods and the magnetic properties of the system were investigated.

4.2 Deposition routes

The first aim of this thesis was to assemble the nanoparticles on a solid substrate. Therefore silicon wafers with a natural oxide layer were used. They were cut into 1x1 cm^2 pieces and cleaned in a two-stage process:

They were first placed inside a beaker filled with ethyl acetate which is an organic solvent. After 45 minutes in an ultrasonic bath most of the lipids and dirt on the surface were removed. Then they were put into a beaker filled with ethanol and left in an ultrasonic bath for further 45 minutes to clean them from ethyl acetate remains. To keep the wafers clean they were stored in ethanol and dried with dry nitrogen gas prior to deposition.

To transfer the nanoparticles on a clean wafer three different deposition routes were utilized which are sketched in Figure 4.2: Sedimentation, drop-casting and spin-coating. Depending on the particle size and shape as well as interactions like van der Waals, steric, dipolar or capillary forces the particles tended to assemble in different ways [19].

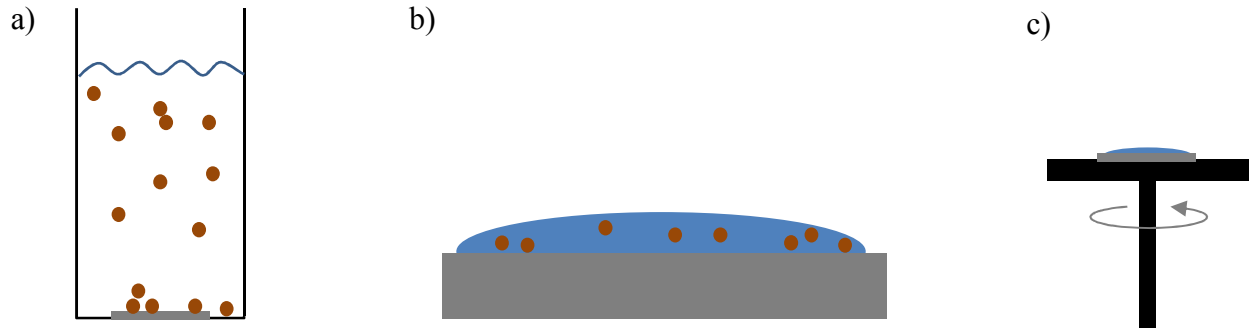

Figure 4.2: *Scheme of deposition routes (not to scale):* ***a)*** *Sedimentation: The colloid is diluted with toluene and left to stand in a beaker with a silicon wafer lying on the bottom. While the solvent evaporates the particles settle on the sample.* ***b)*** *Drop-casting: A drop is deposited on the sample and left to stand to allow the solvent to evaporate.* ***c)*** *Spincoating: A small amount of the colloid is deposited on the center of a wafer and set into rotation. The colloid is forced to the edge and forms a thin film while the solvent evaporates.*

4.2.1 Sedimentation

For sedimentation (Figure 4.2a) a silicon wafer piece measuring 1x1 cm^2 was placed onto the bottom of a beaker. It was filled with 40 ml of toluene, and 18 µl of the commercially available iron oxide colloid were added. The solution was left to stand for 24 h to allow the solvent to evaporate and let the nanoparticles settle on the wafer.

The result is shown in Figure 4.3. The particles order in an irregular, layer-like arrangement (Figure 4.3a-c). Only in areas with a low number density of nanoparticles local hexagonal order is recognizable (Figure 4.3d).

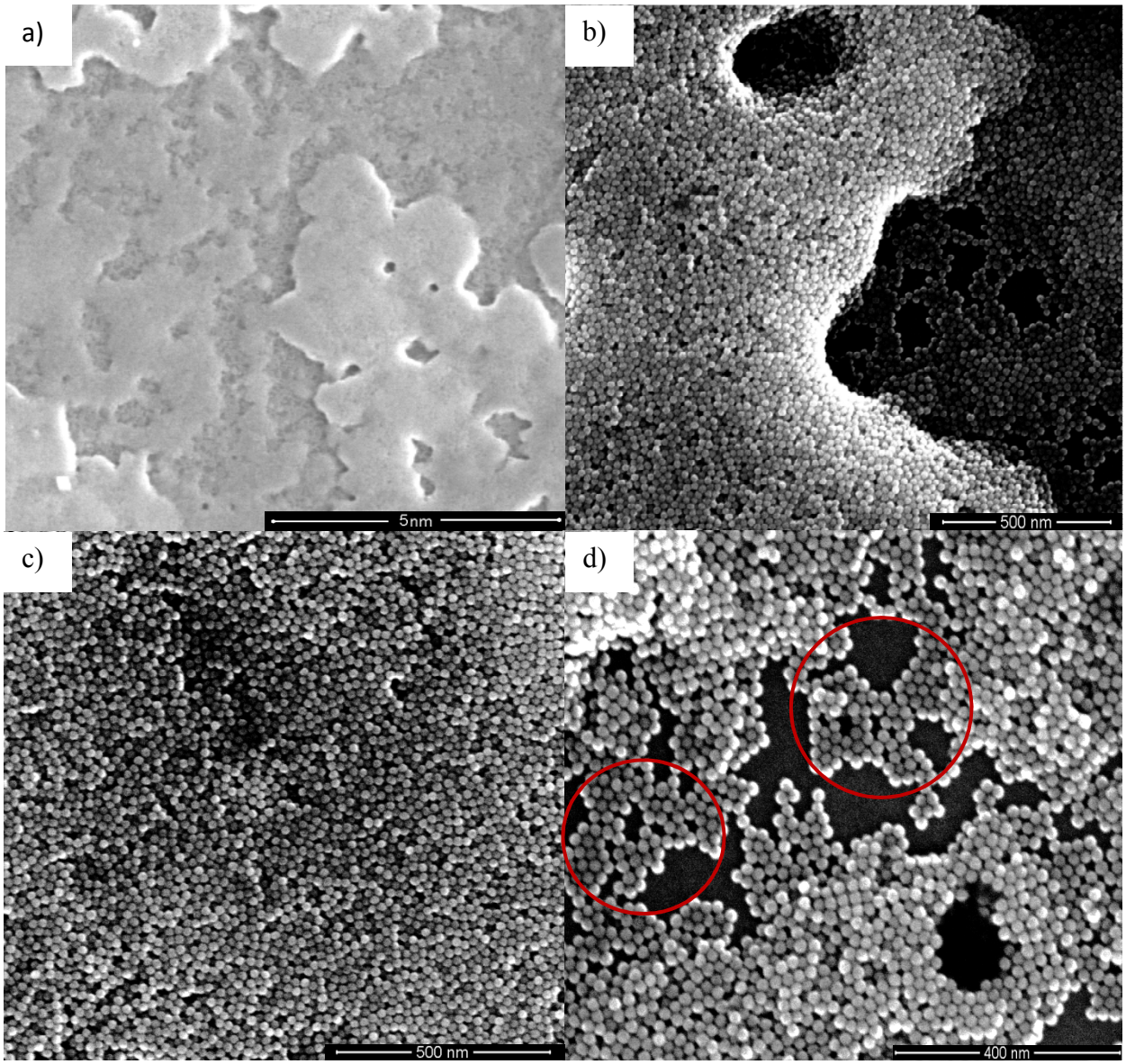

Figure 4.3: *SEM images of iron oxide nanoparticles deposited on a silicon wafer by sedimentation. The pictures were taken in the middle of the sample.* ***a)*** *Disordered multilayer surface.* ***b)*** *Close-up of the transition between monolayer and multilayer.* ***c)*** *Close-up of the disordered multilayer.* ***d)*** *Close-up of the monolayer which exhibits hexagonal order (red circles).*

The process can be modeled using a Langevin formalism of particle transport. The motion is dependent on particle-fluid interaction forces like Stokes drag, body force, virtual mass impacting force, Basset history force and the force due to the acceleration of the undisturbed fluid surrounding the particle. Additionally the particles are influenced by rapidly fluctuating forces (Brownian force) and hydrodynamic interactions. Due to the oleic acid shell agglomeration and deagglomeration processes can be neglected. A model which includes these aspects was described by Ganguly and Chakraborty [102].

4.2.2 Drop-casting

To deposit the nanoparticles by drop-casting, 18 µl of the colloid were applied on a 1x1 cm^2 silicon wafer using a micropipette. The samples were left to stand for 24 h so that the toluene could evaporate.

As shown in Figure 4.4a most of the surface is smooth. On top there are small areas with a second layer which is similar to the surface shown for sedimentation. Concerning the nanoparticle arrangement only small zones exhibit local hexagonal or cubic order (Figure 4.4b). In areas with a low number concentration of particles just a hexagonal order is observable (Figure 4.4c-d). Additionally the amount of nanoparticles on the edge of the sample is higher than in the center.

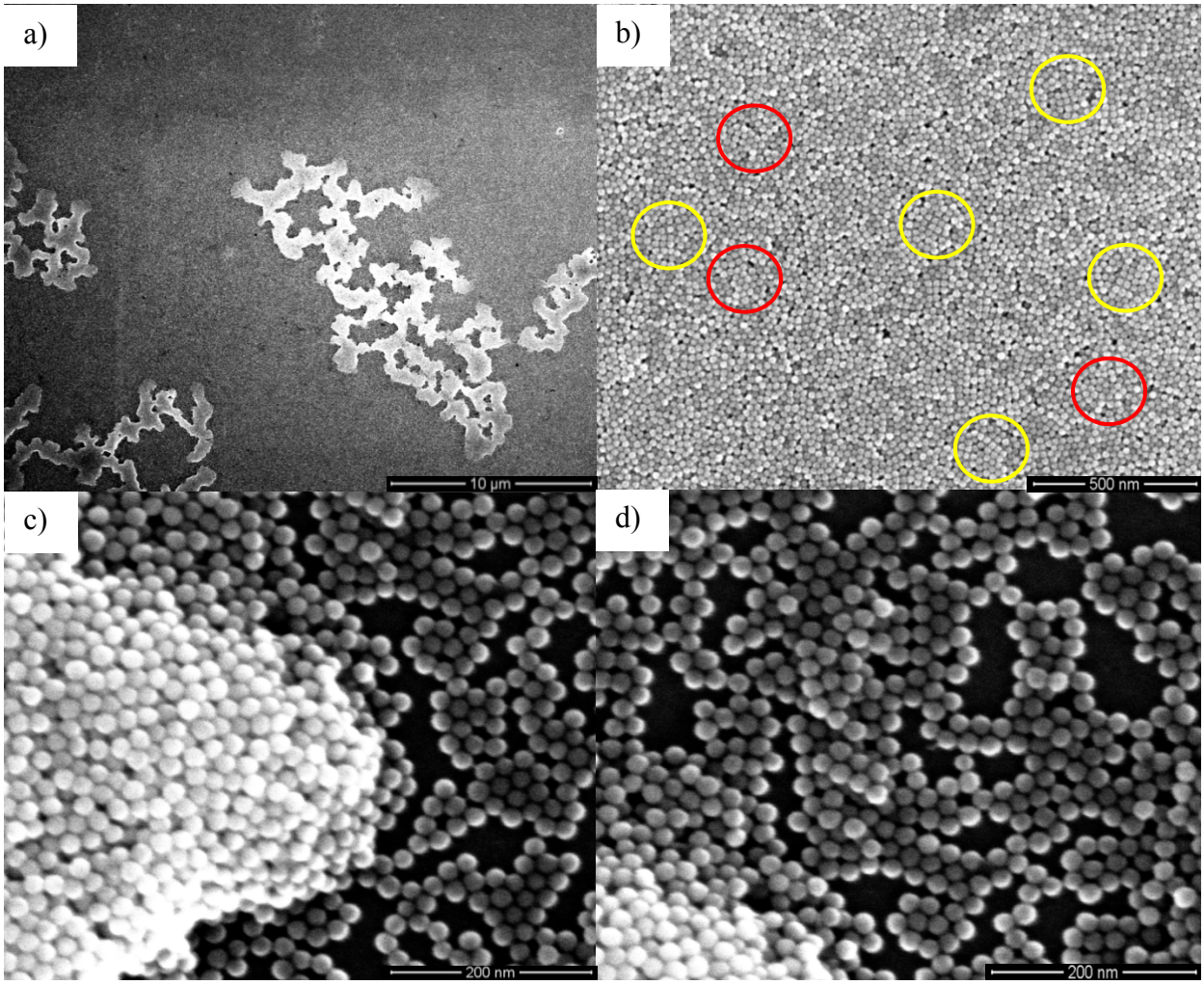

Figure 4.4: *SEM images of iron oxide nanoparticles deposited on a silicon wafer by drop-casting taken in the middle of the sample.* ***a)*** *Smooth surface with a disordered layer on top.* ***b)*** *Close-up: Smooth surface (red circles: hexagonal order, yellow circles: cubic order).* ***c)*** *Close-up: Transition between sub-monolayer and multilayer.* ***d)*** *Close up: Sub-monolayer with hexagonal order.*

To describe the process several models have to be combined: There is a strong interaction between the nanoparticles and the substrate leading to a Fank-van-der-Merwe like growth resulting in a smooth surface [103]. Additionally a two-dimensional solution of nanoparticles is dynamically produced at the liquid-air interface by rapid evaporation. This leads to the nucleation of islands which stick to the interface. During late stage drying these islands are lied

down on the surface [17] [104] [105]. Furthermore a coffee-ring-effect can be observed: During the evaporation process the contact line of the drop is pinned so the liquid which evaporates from the rim must be replenished by liquid from the interior. This leads to an outward flow carrying the particles to the interface what results in a thicker nanoparticle layer compared to the center [106] [107].

4.2.3 Spincoating

For the last deposition route a 1x1 cm^2 silicon wafer was mounted on a spincoater. 9 µl of the colloid were applied using a micropipette. The sample was accelerated up to its final rotation speed of 50 rps at which it spinned for 60 s.

The result is depicted in Figure 4.5. The surface is very homogeneous and even (Figure 4.5a). It exhibits many areas of up to 50000 nm^2 that are highly ordered in a hexagonal arrangement (Figure 4.5b). Additionally there are several regions with drying cracks (Figure 4.5c-d).

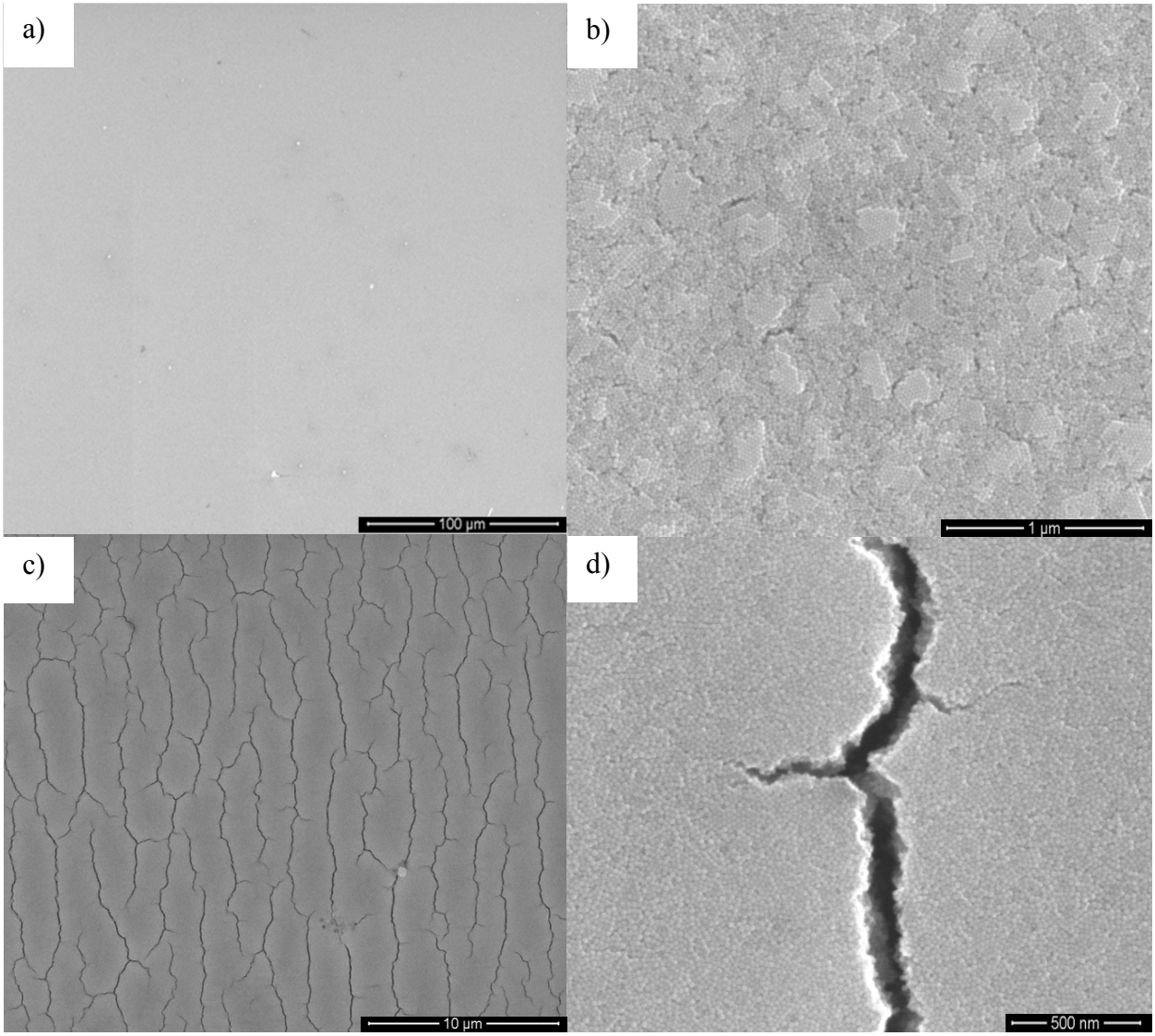

Figure 4.5: *SEM images of iron oxide nanoparticles deposited on a silicon wafer by spincoating. The pictures were taken in the middle of the sample.* ***a)*** *Smooth surface.* ***b)*** *Close-up of the smooth surface: Several well-ordered areas with hexagonal arrangement are visible.* ***c)*** *Drying cracks.* ***d)*** *Close-up of a drying crack.*

Whereas the sample spins the colloid is pushed towards the edge by centrifugal force. Depending on the viscosity, acceleration rate, final rotation speed and duration of spinning it reaches a final thickness [108]. The homogeneity is dependent on the wettability of the solvent on the substrate [19]. With this method a very smooth surface can be reached. For the reason that the layer becomes very thin and because of the high vapor pressure of the solvent (toluene), the evaporation process is very fast. The particles are meanwhile drawn together due to capillary forces. This leads to tensile stress which finally causes cracks. Additionally the cracks arise in a preferred direction due to centrifugal forces [109].

For the reason that samples with desired properties like a smooth, homogeneous surface with a high amount of self-assembly could be reached by this deposition route it was chosen to prepare all samples for magnetic measurements by spincoating. Additionally it allows adjusting the layer thickness by dilution and rotational speed.

4.3 Dilution

The magnetic properties of three-dimensional nanoparticle arrays can become very complex, so a (sub-)monolayer had to be produced by spincoating. Therefore the colloid was diluted with toluene in different proportions and deposited as described in chapter 4.2.3.

For a dilution of 1:10 a dense, well-ordered particle layer emerged (Figure 4.6). But there were still many particles on top so the colloid was further diluted. At a ratio of 1:20 (Figure 4.7a-b) a sub-monolayer was formed without any islands in the center of the sample. At the edge there were still thicker layers that are comparable to Figure 4.6a, hence a dilution of 1:30 was chosen. It was similar to the former sample but more homogeneously without any islands even at the edge of the sample (Figure 4.7c-d).

Additionally the arrangement already allows conclusions to possible nanoparticle interactions. As shown in Figure 4.7d the particles tend to form chains where the number concentration is low enough. This indicates that there is a strong dipolar interaction between the nanoparticles [105] [110].

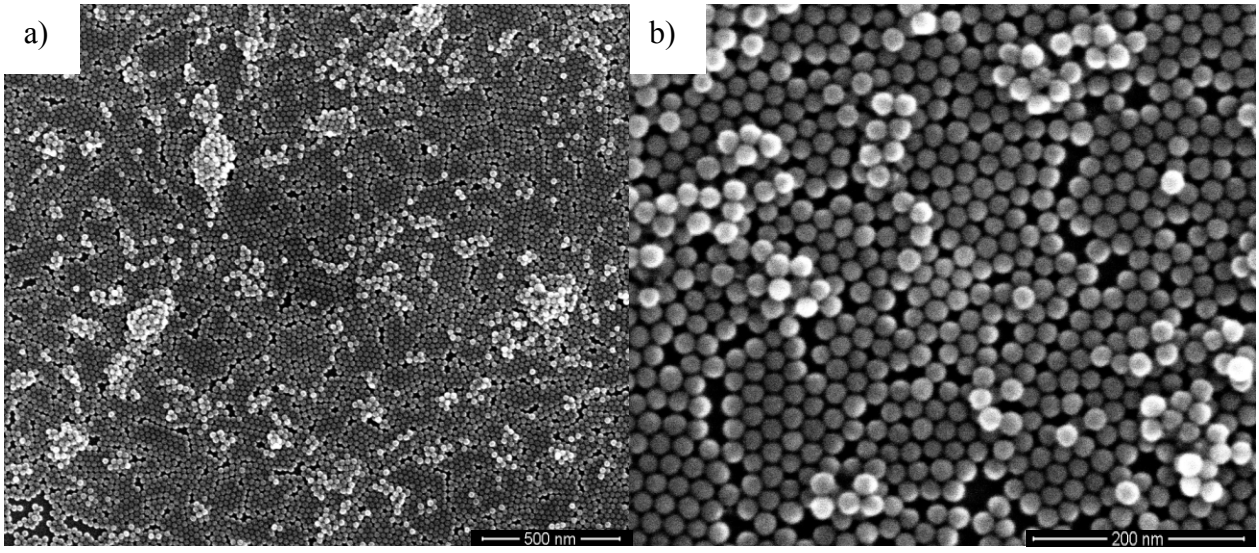

Figure 4.6: *SEM images of iron oxide nanoparticles deposited on a silicon wafer by spincoating diluted with toluene at a ratio of 1:10. The pictures were taken in the middle of the sample.* ***a)*** *Well-ordered monolayer with nanoparticle agglomerates on top.* ***b)*** *Close-up showing the hexagonal arrangement of the monolayer.*

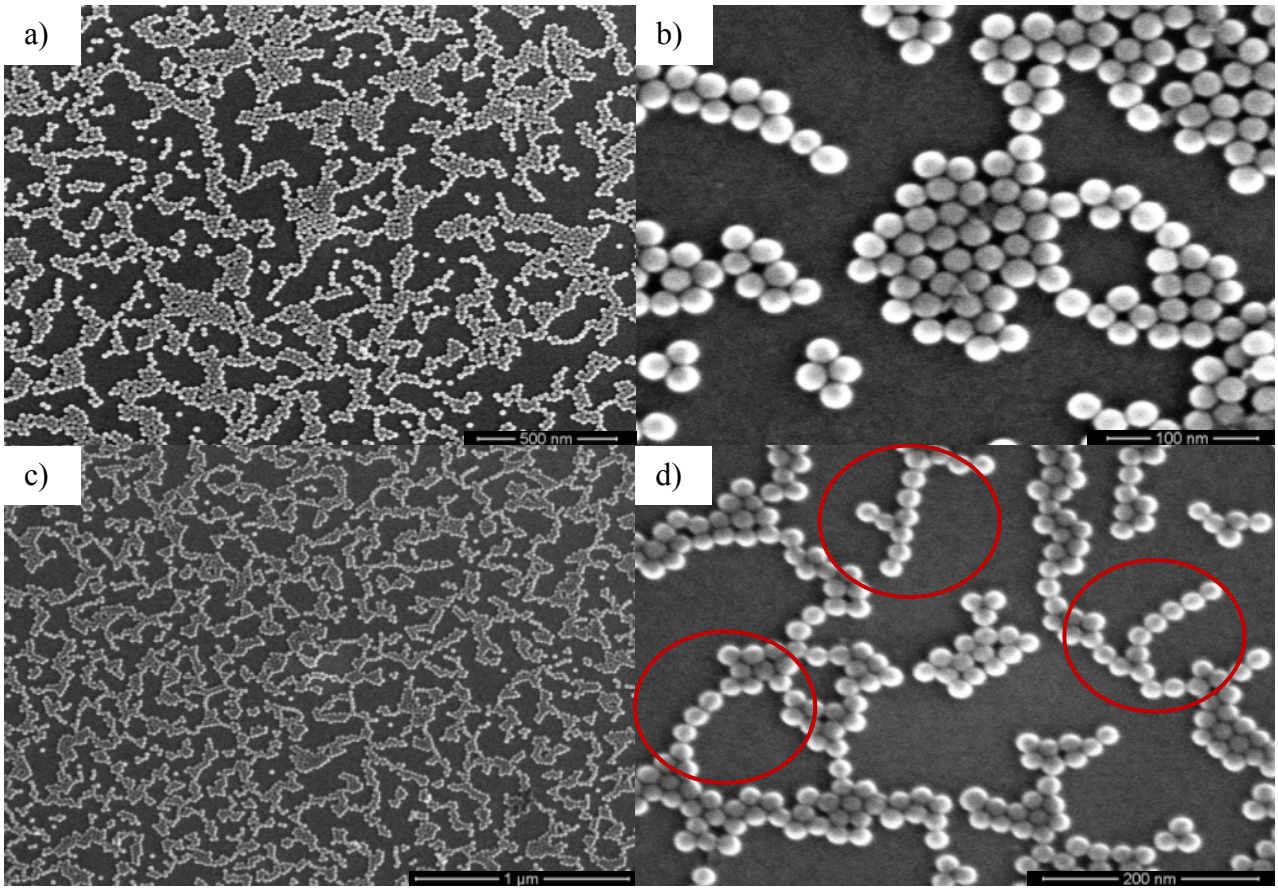

Figure 4.7: *SEM images of iron oxide nanoparticles deposited on a silicon wafer by spincoating. The pictures were taken in the middle of the sample.* ***a-b)*** *Dilution with toluene at a ratio of 1:20 and* ***c-d)*** *1:30. The particles tend to form chains (red circles) what indicates a strong dipolar interaction.*

4.4 Oleic acid removal

To mediate magnetic interaction by a metallic matrix material the oleic acid shell had to be removed from the particles [105]. Therefore two different approaches were applied: The dilution with acetone on the one hand and a plasma process on the other.

4.4.1 Acetone

Acetone is a well-known solvent that is often used to remove lipids. To avoid agglomeration due to van der Waals interactions after the removal of the oleic acid shell, an ultrasonic bath was used. The colloid was transferred into a beaker using a micropipette. Acetone was added in a proportion of 1:10, 1:20 and 1:30. After stirring for 5 s the nanoparticles were deposited on a wafer as described in chapter 4.2.3.

As shown in Figure 4.8 a hole formation can be observed. Along the perimeter the nanoparticles order in a hexagonal monolayer arrangement with a disordered, thicker layer on the edge. For a dilution of 1:10 there is no order recognizable between the holes (Figure 4.8a-b). For a ratio of 1:30 the particle concentration is low enough for a monolayer formation between the holes (Figure 4.8e-f). The arrangement in this area is similar to the one observed for particles diluted with toluene at a proportion of 1:30. Additionally the number and size of holes increases as the amount of acetone is raised. If the hole density is high enough, they touch leading to an even thicker layer at the edge.

This behavior can be explained by an instability model proposed by Ohara and Gelbart: During the spincoating-process a uniform, thin, liquid film is formed on the surface. While the volatility of the solvent (acetone) forces it to evaporate, the disjoining pressure tries to prevent the film from becoming too thin. As the critical thickness is reached holes open up to keep the layer at a certain thickness. The holes grow in size and most of the particles are dragged along the rim until enough particles accumulate so that they cannot be pushed along any further due to lateral friction - the edge of the hole is pinned [111] [112].

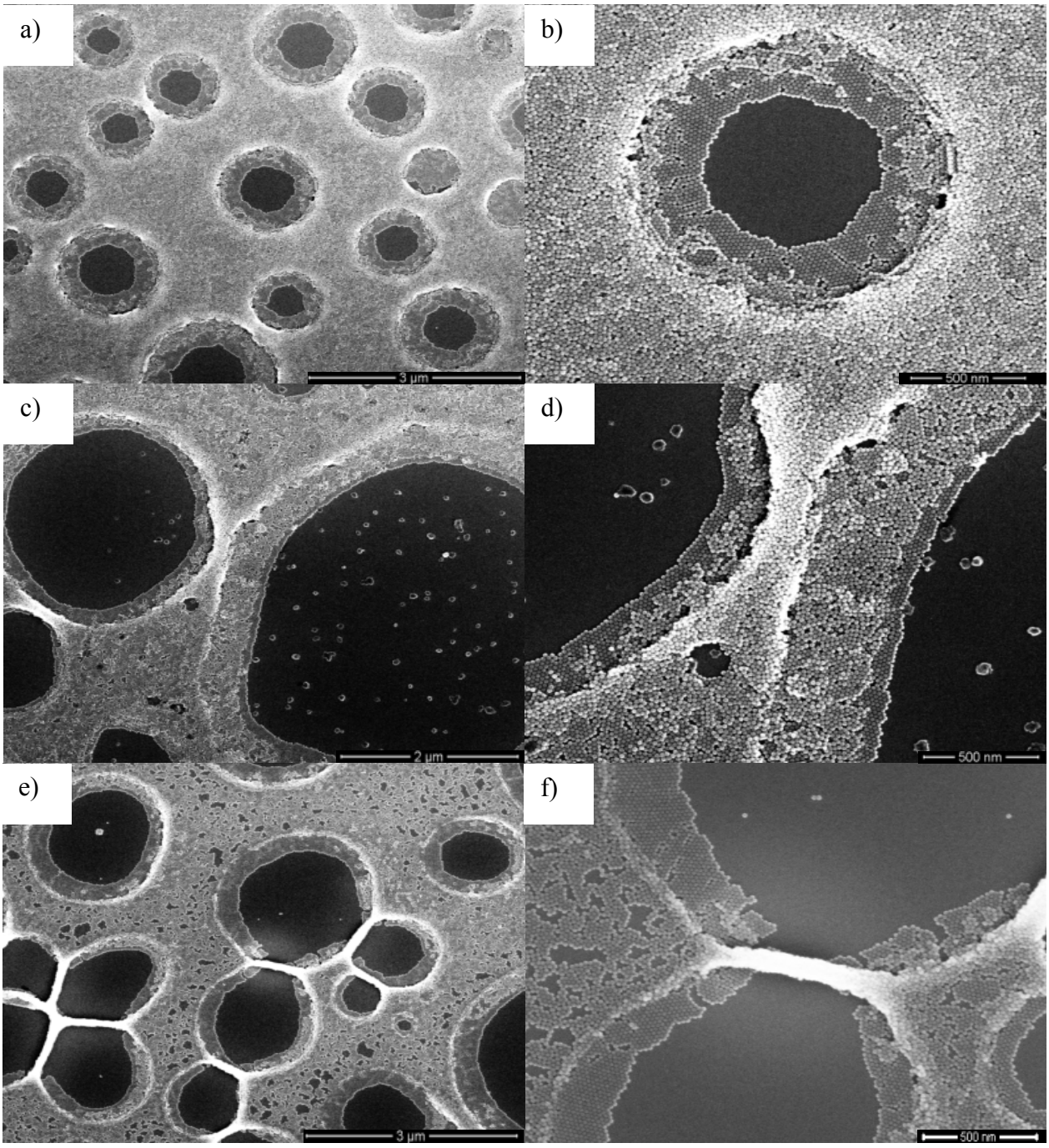

Figure 4.8: *SEM images of iron oxide nanoparticles deposited on a silicon wafer by spincoating. The pictures were taken in the middle of the sample. The nanoparticles form holes with a well-ordered monolayer on the rim.* ***a-b)*** *Dilution with acetone at a ratio of 1:10,* ***c-d)*** *1:20 and* ***e-f)*** *1:30. Here the number concentration of nanoparticles is low enough to form a sub-monolayer between the holes. It exhibits hexagonal order.*

To proof that the hole formation is not caused by the ultrasonic bath, the preparation was repeated skipping this step. As shown in Figure 4.9 the holes are still observable but they are more unevenly distributed and there is a broadened size distribution for the samples prepared without the ultrasonic bath. In this case the colloid is less well mixed leading to a less homogeneous arrangement.

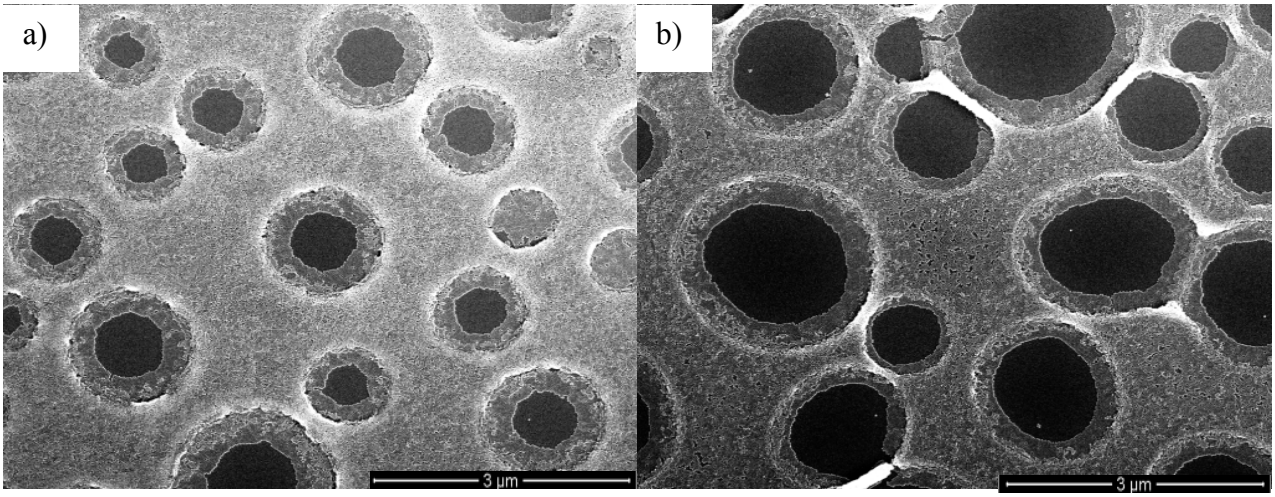

Figure 4.9: *SEM images of iron oxide nanoparticles diluted with acetone in a proportion of 1:10 and deposited on a silicon wafer by spincoating. The pictures were taken in the middle of the sample. The nanoparticles form holes with a well-ordered monolayer on the rim.* ***a)*** *During the dilution process an ultrasonic bath was used.* ***b)*** *No ultrasonic bath during dilution.*

For the samples diluted with toluene this effect does not occur because of its significantly lower vapor pressure (184 mmHg for acetone [113] compared to 22 mmHg [114] for toluene at 300K). Therefore the evaporation process is much slower and the particles have already settled on the surface as the critical solvent thickness is reached.

Since the particles are desired to form a homogenous, ordered layer on the surface, this approach of oleic acid removal is not suitable and a different method has to be applied.

4.4.2 Plasma processing

Another approach to remove the oleic acid shell is plasma etching [115]. Therefore a TePla 300 Plasma Processor was used with an oxygen gas flow of 200 ml/min and a power of 300 W. The colloid was diluted with toluene in a proportion of 1:30 and deposited as described in chapter 4.2.3. Afterwards the samples were treated with the oxygen plasma for 2, 10 and 30 min at a pressure of approximately 0.7 mbar.

The samples have not changed visually after 2 min and 10 min (Figure 4.10b-c) compared to the untreated one (Figure 4.10a). After 30 min the nanoparticles have a different shape and look rather cubic than spherical (Figure 4.10d). This indicates a kind of recrystallization or phase transition that will be further discussed in chapter 4.6.1.

All the treated samples have in common that they rather build aggregates than chains. Therefore the van der Waals interaction dominates which indicates that the oleic acid shell is removed so that the influence of the dipolar interaction observed for the untreated sample is negligible for self-assembly.

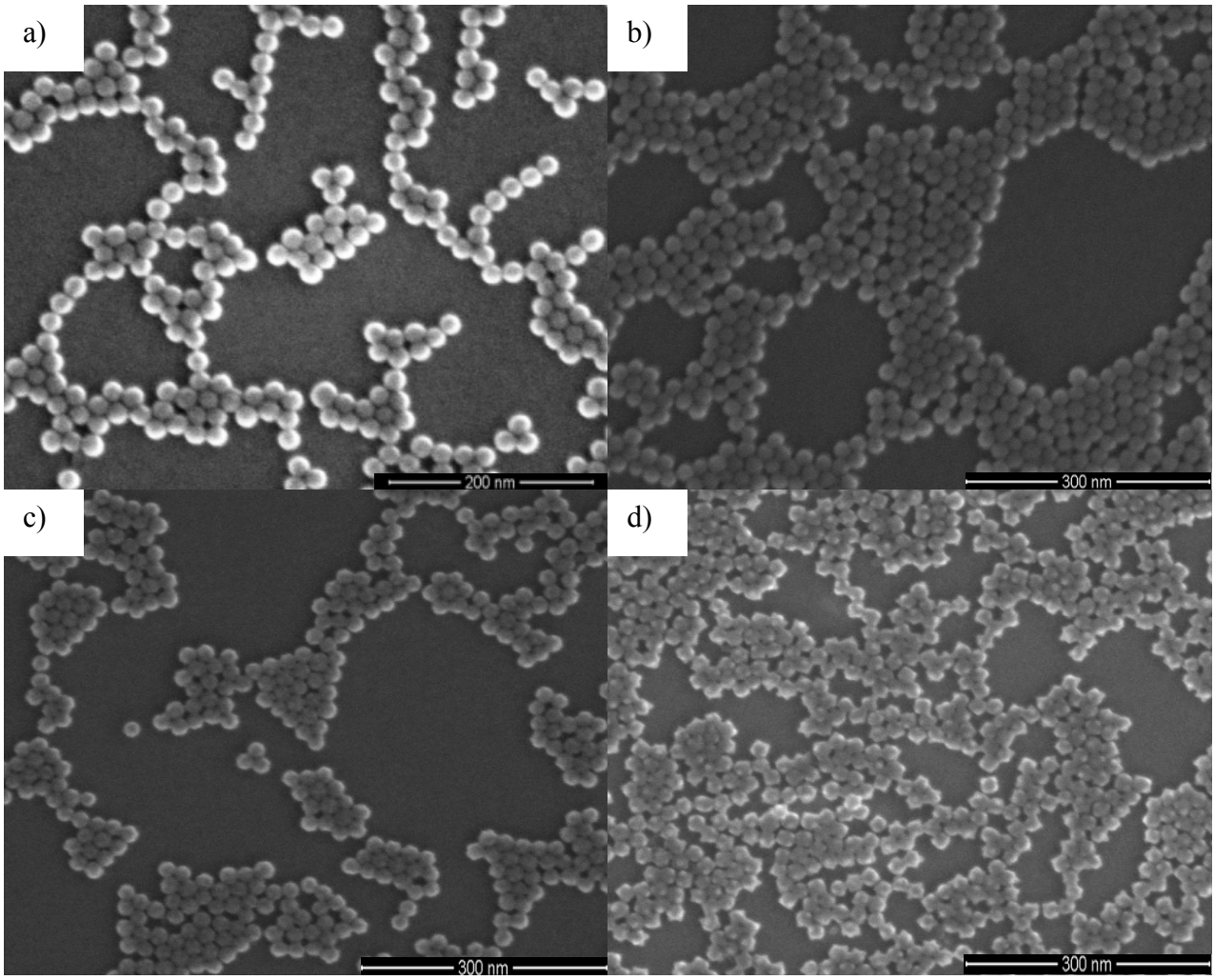

Figure 4.10: *SEM images of iron oxide nanoparticles diluted with toluene in a proportion of 1:30 and deposited on a silicon wafer by spincoating. The pictures were taken in the middle of the sample.* ***a)*** *Without plasma treatment.* ***b)*** *2 min oxygen plasma.* ***c)*** *10 min oxygen plasma.* ***d)*** *30 min oxygen plasma.*

4.5 Metal deposition

After the assembly of the iron oxide nanoparticles on a silicon wafer and the removal of the oleic acid shell, the matrix material could be deposited (Figure 4.11). Due to instrumental conditions different techniques had to be used.

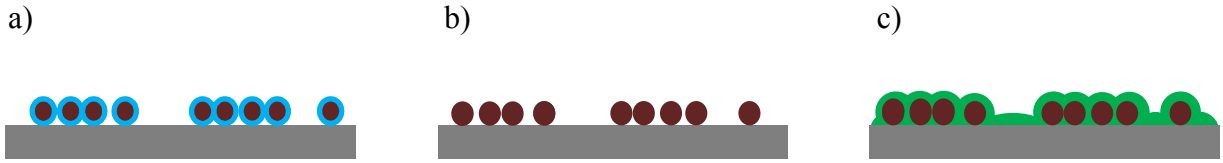

Figure 4.11: *Schematic of nanoparticle processing (not to scale):* ***a)*** *Nanoparticles (brown) with oleic acid shell (blue) on the silicon wafer (grey.)* ***b)*** *Oleic acid is removed.* ***c)*** *Metal (green) deposition.*

Platinum and gold were deposited by a magnetron sputter process. Figure 4.12 shows samples that were prepared as described in chapter 4.4.2 with 20 nm of metal on top. Due to its high mobility, gold seems to be deposited more isotropic (Figure 4.10a-b) than platinum (Figure 4.12c-d). There is no visual difference observable between the samples prepared with or without plasma treatment.

Palladium and niobium were deposited by molecular beam evaporation and IBS, respectively. Unfortunately it was not possible to include SEM images due to limited measurement time.

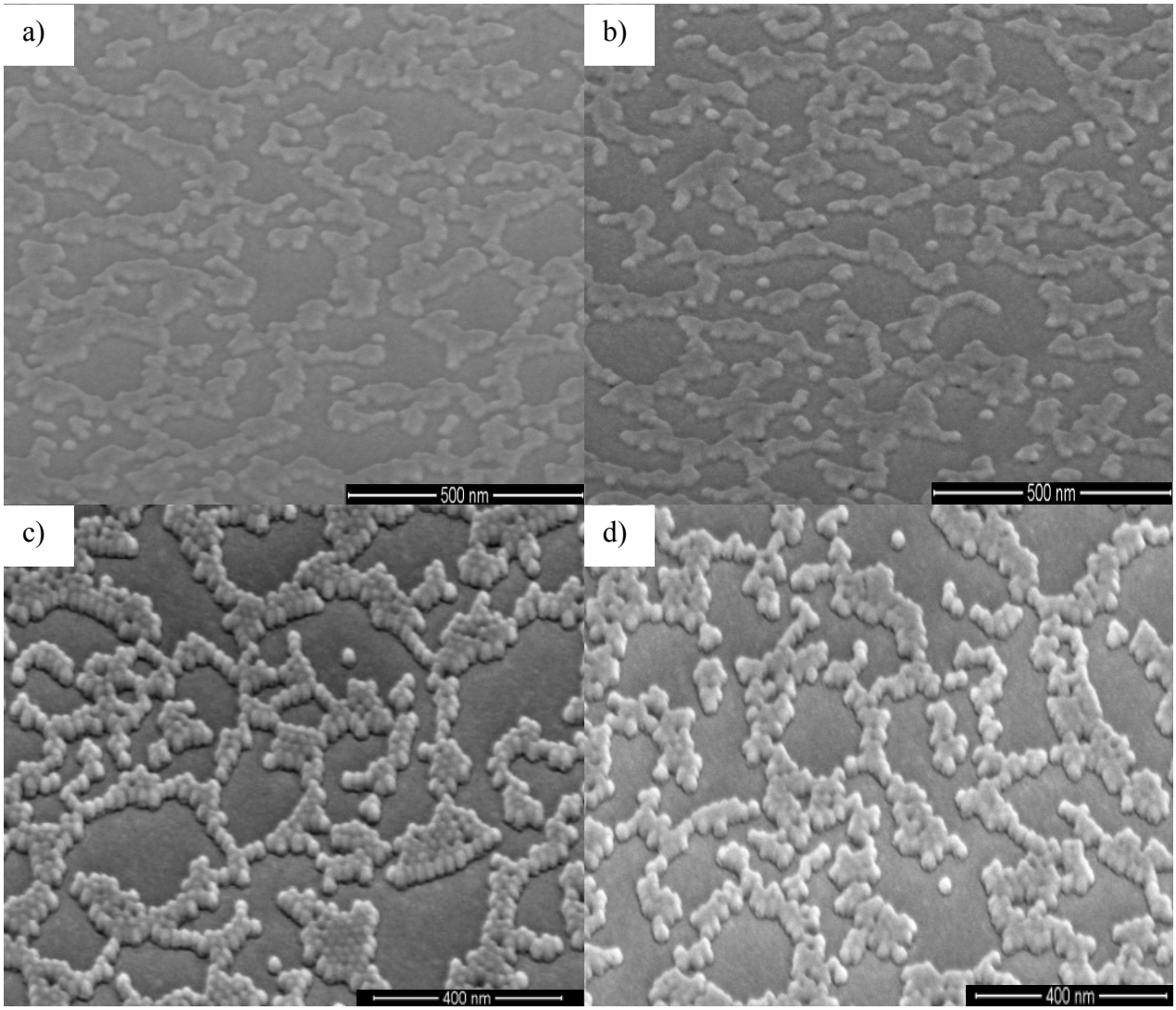

Figure 4.12: *SEM images of iron oxide nanoparticles diluted with toluene in a proportion of 1:30 and deposited on a silicon wafer by spincoating. Different metals were applied by magnetron sputtering. The pictures were taken in the middle of the sample.* ***a)*** *No plasma treatment prior to the deposition of 20 nm gold.* ***b)*** *30 min oxygen plasma, 20 nm gold.* ***c)*** *No plasma treatment prior to the deposition of 20 nm platinum.* ***d)*** *30 min oxygen plasma, 20 nm platinum.*

4.6 MPMS measurements

For the MPMS measurements all samples were prepared by the deposition of the commercially available iron oxide nanoparticle colloid (20 nm spheres) on a silicon wafer via spincoating at 50 rps for 60 s. Some of the samples were treated with oxygen plasma. Additionally a matrix material in the form of different metals was deposited on a subset of them. Due to experimental conditions the wafers were cut to a size of approximately 5x7 mm^2.

4.6.1 Magnetic properties

To analyze the magnetic properties, the so-called 'zero-field-cooled' curve (ZFC) and the 'field-cooled' curve (FC) were measured as well as hysteresis loops at three different temperatures (5 K, 100 K and 300 K).

For the ZFC curve the samples were transferred into the MPMS and heated up to a temperature of 350 K. Afterwards they were cooled down to 5 K in zero magnetic field. Then a magnetic field of 50 Oe was applied and the temperature was raised to 350 K while measuring the magnetic moment. Subsequently the FC curve was obtained by cooling down the sample to a temperature of 5 K and simultaneously measuring the magnetic moment [116].

Due to the diamagnetic silicon substrate, the hysteresis loops were superimposed by a diamagnetic signal that had to be removed as shown in Figure 4.13. Therefore a tangent was applied to the curve in the saturation region. Then a linear function in the form f(x) = ax where a is the slope of the tangent was subtracted from the hysteresis [117]. The slope values used for the presented curves are shown in Appendix B.

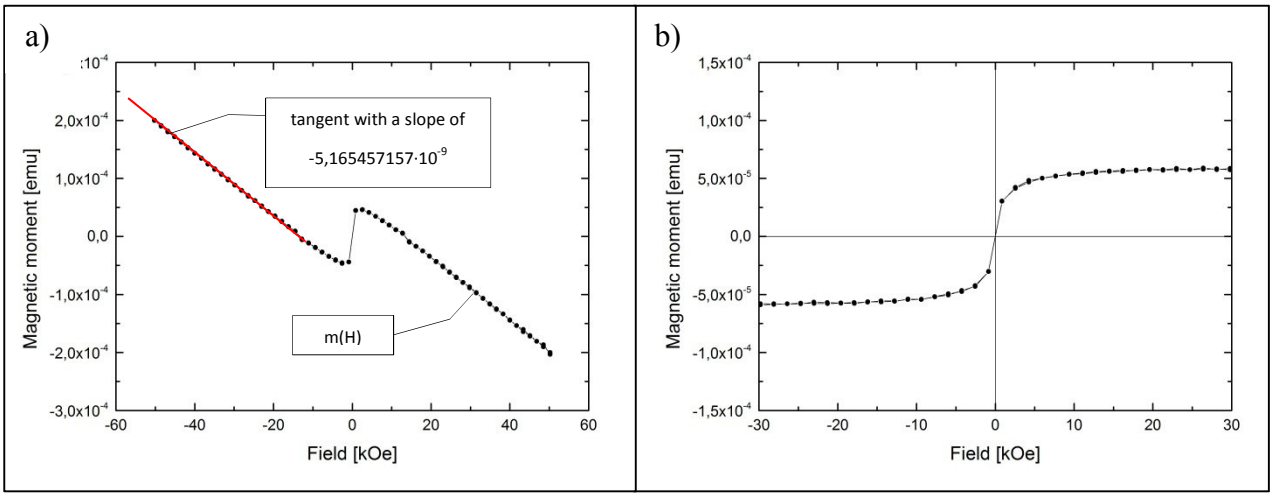

Figure 4.13: a) *Example curve of the magnetic moment m in dependency of the field H of a nanoparticle sample (black) with a tangent in the saturation region (red).* ***b)*** *m(H) – [-5.165457157·10^{-9}·H].*

4.6.1.1 Layer thickness

To analyze the influence of the layer thickness the curves of a sample with a toluene dilution of 1:30 are compared to the results for an undiluted colloid.

Figure 4.14 shows the hysteresis loops obtained for the latter. At 300 K (Figure 4.14a) the curve is S-shaped and closed. It opens up and broadens as the temperature is lowered (Figure 4.14b-c). This is the typical behavior of a superparamagnetic material: At room temperature (300 K) the timescale to measure the hysteresis is larger than the relaxation time hence the loop is

comparable to a curve obtained for a paramagnetic system. Due to the temperature dependency of the relaxation time the hysteresis opens up at a certain temperature. There the measurement duration is shorter than the time the superspin needs to switch between its two possible orientations and the curve becomes similar to the hysteresis of a ferromagnetic material (chapter 2.4.2.2) [116].

Additionally the loop is shifted to the left which is likely to be caused by exchange bias (chapter 2.4.3). This indicates that the nanoparticles consist of at least two different types of iron oxide. The coercive field strengths at 5 K are shown in Appendix C.

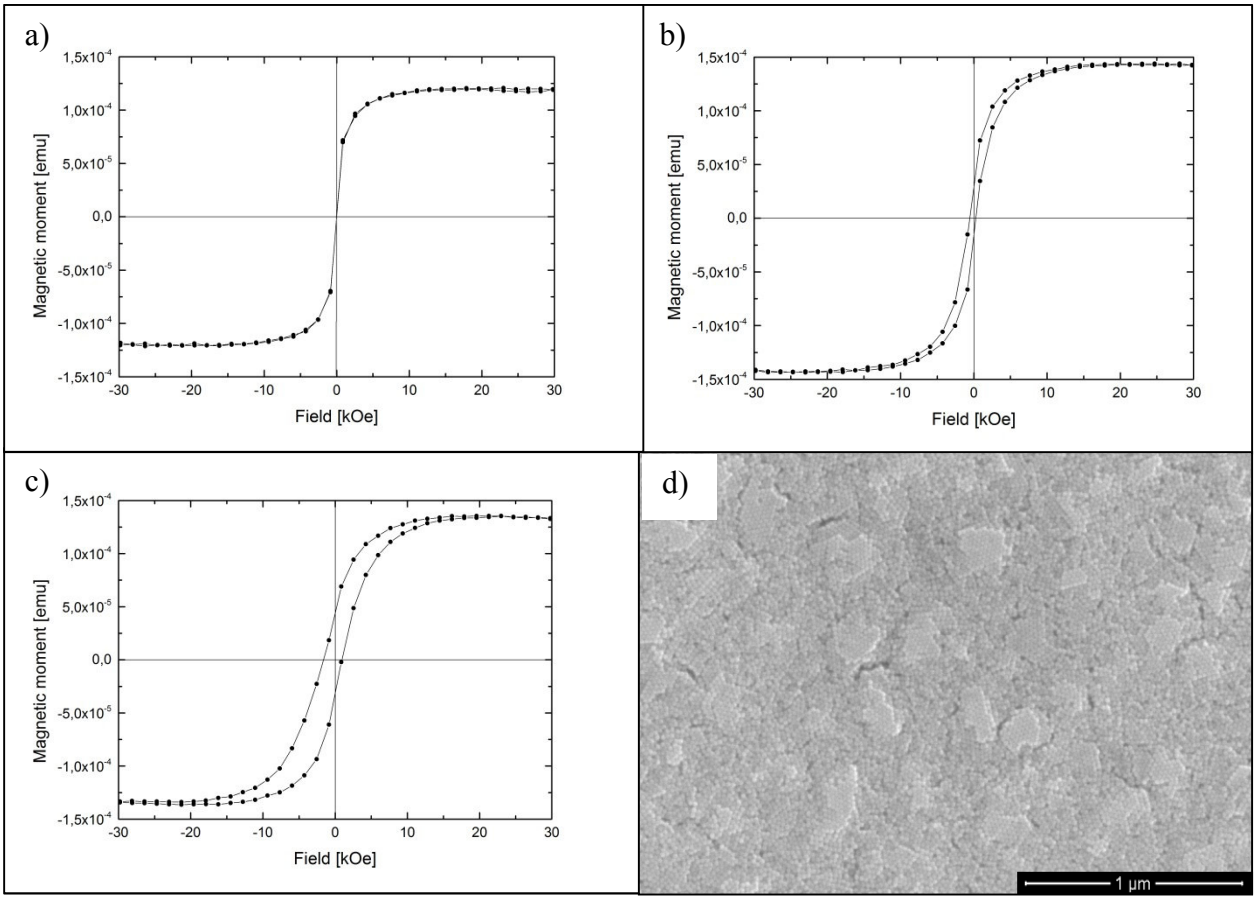

Figure 4.14: *Hysteresis curves for an undiluted sample measured at* ***a)*** *300 K,* ***b)*** *100 K and* ***c)*** *5 K that show superparamagnetic behavior. Additionally the curves obtained below the blocking temperature are shifted to the left due to exchange bias (Appendix C).* ***d)*** *SEM image of the sample.*

The ZFC and FC curves of the undiluted sample are depicted in Figure 4.15. For the reason that the magnetic field is switched off at the beginning of the measurement, the spins of the particles are oriented along their easy axes. As the sample is cooled down to 5 K, the spins become blocked at T_B, i.e. the thermal energy is too low to overcome the energy barrier between the two possible orientations and the spins stay in a fixed direction (chapter 2.4.2.2). The particles 'freeze' in randomly distributed orientations according to their easy axes; hence the total magnetic moment is approximately zero. As the temperature is raised in an applied magnetic field (ZFC curve) the total magnetic moment increases gradually due to deblocking which is in turn due to thermal fluctuations.

At the blocking temperature $T_B \approx 245$ K the spins are able to switch freely and arrange along the field direction. Therefore a maximum magnetic moment of approximately $2 \cdot 10^5$ emu can be observed. As the temperature is further increased the magnetic moment decreases due to thermal fluctuations (Curie behavior). Subsequently the temperature is lowered in the same external field (FC curve) and the magnetic moment increases again because of reduced thermal fluctuations.

Depending on the spin arrangement inside the nanoparticles different behaviors are observed below the blocking temperature: For an antiferromagnetic material the curve reaches its maximum at T_N and subsequently decreases. This is caused by spin interaction which tends to an antiparallel arrangement (Figure 2.8). The magnetic moments cancel each other out and the magnetization is lowered. Therefore the ZFC and FC curve of an ideal AF are identical [118]. For a ferro- or ferrimagnetic material the FC curve keeps increasing with decreasing temperature because the spins arrange parallel to each other and along the field direction [119] [120] [121].

Figure 4.15 shows an overlap of both cases where the FC curve is lowered below T_B but is not identical to the ZFC curve. Hence the iron oxide nanoparticles consist of a ferro- / frerrimagnetic and an antiferromagnetic material what complies with the exchange bias assumption. This is further confirmed by the offset between the peaks in ZFC and FC curve: The ZFC curve is distorted by the ferro- / ferrimagnet while the antiferromagnet dominates for the FC curve.

Benitez et al. analyzed identical particles by XRD and high resolution transmission electron microscopy (HRTEM) and showed that they consist of wustite and an iron oxide exhibiting spinel structure [122]. This also complies with the results presented since wustite is an antiferromagnet and the ferrimagnetic iron oxides maghemite and magnetite are both spinels (chapter 2.1). For the reason that no Verwey transition can be observed, the ferrimagnetic subsystem seems to be maghemite [122] [123]. Additionally the ZFC curve shows an atypical steep increase at approximately 198 K which reflects the Néel temperature of wustite [122].

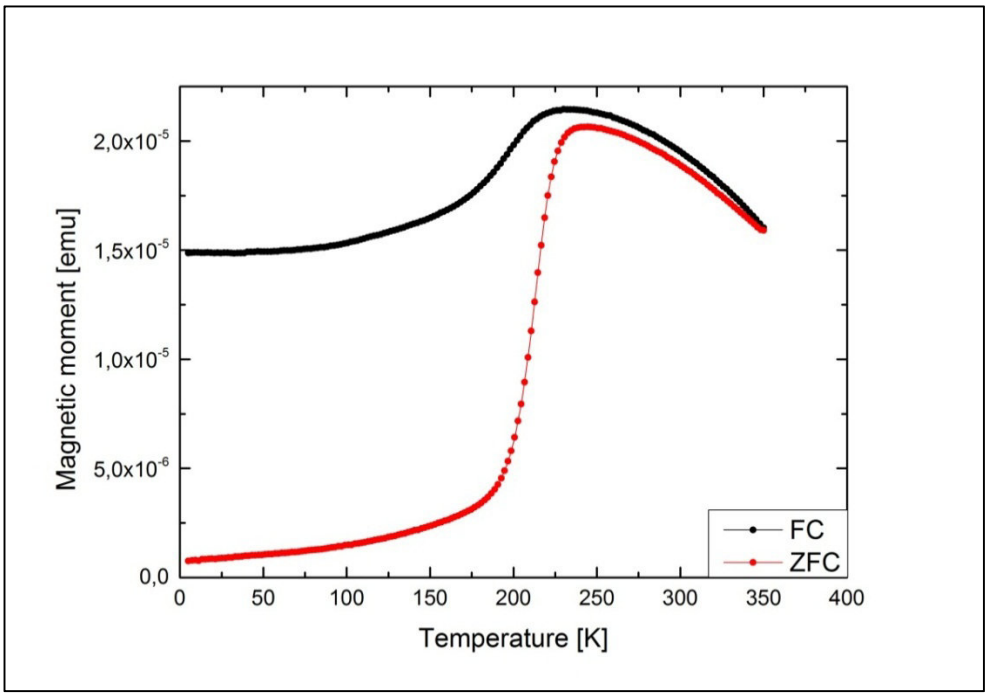

Figure 4.15: *ZFC (red) and FC (black) curve of an undiluted sample measured in a field of 50 Oe. The behavior is caused by the combination of antiferromagnetic wustite and ferrimagnetic maghemite.*

In Figure 4.16a-c the hysteresis curves for a sample diluted with toluene at a proportion of 1:30 are depicted. They show the same superparamagnetic behavior as the undiluted sample and they are also shifted due to exchange bias. Only the saturation magnetization is reduced due to a lower number of particles. The ZFC and FC curves are shown in Figure 4.16e. They have the same shape as the curves of the undiluted sample.

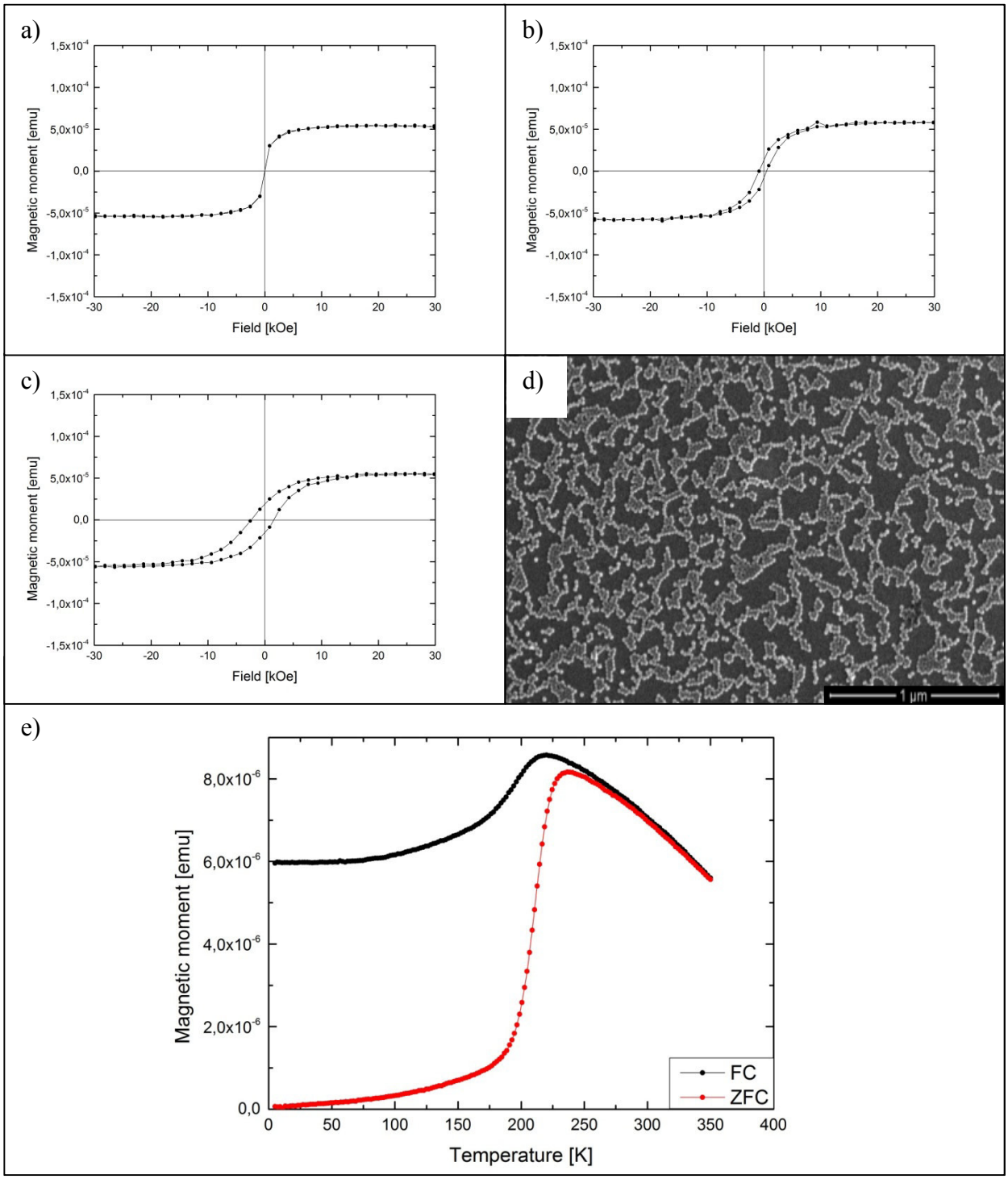

Figure 4.16: *Hysteresis curves of a sample diluted with toluene at a proportion of 1:30 measured at* ***a)*** *300 K,* ***b)*** *100 K and* ***c)*** *5 K that show superparamagnetic behavior. The curves obtained below the blocking temperature are shifted to the left due to exchange bias (Appendix C).* ***d)*** *SEM image of the sample.* ***e)*** *ZFC (red) and FC (black) curve measured in a field of 50 Oe. The behavior is similar to the undiluted sample.*

4.6.1.2 Samples treated with acetone

As shown in chapter 4.4.1 the dilution with acetone has a large impact on the nanoparticle self-assembly. Nevertheless the different arrangement does not influence the magnetic properties. Figure 4.17 and Figure 4.18 show the hysteresis and ZFC-FC curves of a sample diluted with acetone at a ratio of 1:30. The results are similar to those obtained for a sample diluted with toluene at same proportion (Figure 4.16) except for the saturation magnetization which is similar to the one obtained for the undiluted sample (Figure 4.14). This could be caused by the comparably dense nanoparticle arrangement between the holes. Unfortunately the oleic acid could be detected neither chemically nor optically due to its relatively small amount. Hence it is not possible to establish whether the oleic acid shell is not removed at all, if it is only slightly damaged and the effect is therefore not verifiable, or if it is insignificant for the magnetic properties.

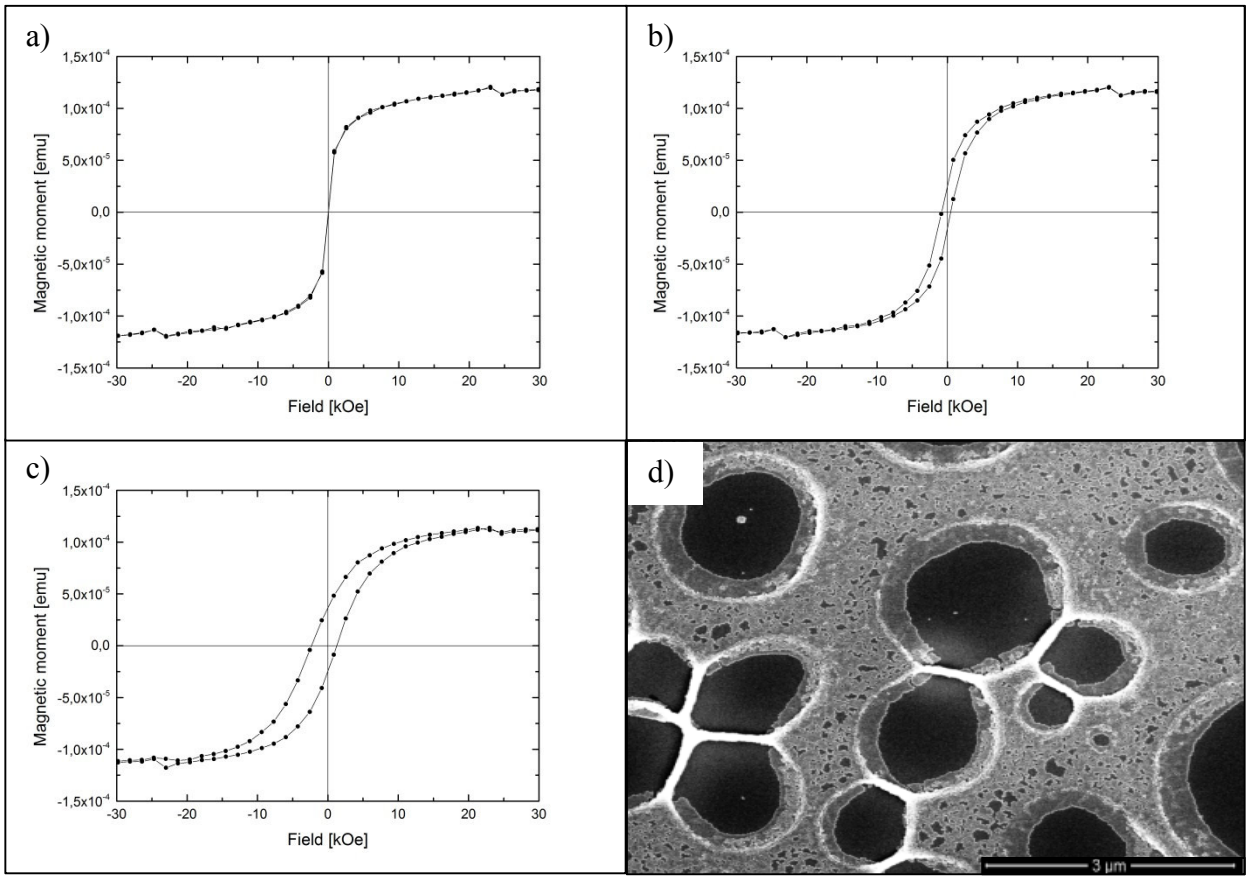

Figure 4.17: *Hysteresis curves of a sample diluted with acetone at a ratio of 1:30 measured at* ***a)*** *300 K,* ***b)*** *100 K and* ***c)*** *5 K that show superparamagnetic behavior. Additionally the curves obtained below the blocking temperature are shifted to the left due to exchange bias (Appendix C).* ***D)*** *SEM image of the sample.*

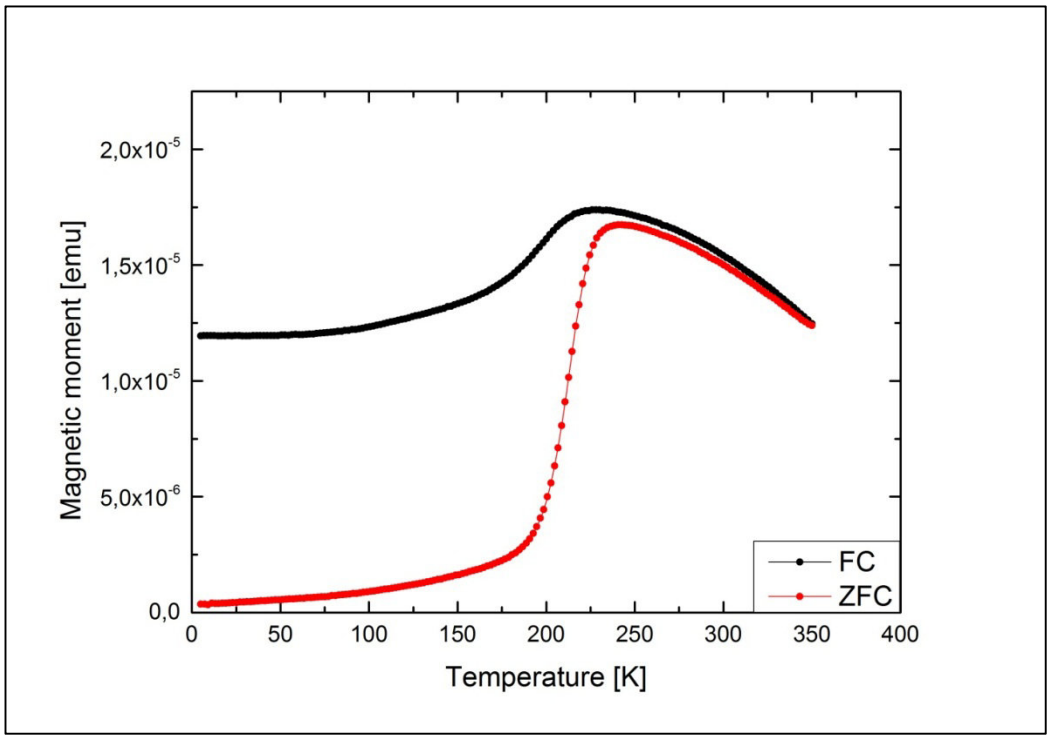

Figure 4.18: *ZFC (red) and FC (black) curve of a sample diluted with acetone at a ratio of 1:30 measured in a field of 50 Oe. The behavior is similar to the sample diluted with toluene at the same proportion.*

4.6.1.3 Plasma

The colloid was diluted with toluene at a proportion of 1:30 and deposited as shown in chapter 4.2.3. Subsequently a plasma treatment was performed with various etching times to remove the oleic acid shell:

4.6.1.3.1 2 minutes

The hysteresis curves of a sample treated with oxygen plasma for 2 min are depicted in Figure 4.19a-c. They are very similar to those obtained for samples without plasma treatment at the same dilution (Figure 4.16): The superparamagnetic behavior and the exchange bias are still observable. Even the saturation magnetization is close to the value obtained for the untreated sample. The particles still contain wustite since the ZFC curve shows a steep increase at 198 K and the FC curve decreases below the Néel temperature of wustite (Figure 4.19e), but not as much as for the untreated sample (Figure 4.16). Hence the amount of wustite seems to be reduced. This could be due to partial transformation into maghemite which is indicated by the second peak observable at 125 K. It is not caused by the Verwey transition of magnetite because it would also appear in the FC curve which is not the case [122] [123]. Additionally the ZFC and FC curves are not identical at high temperatures. Hence the system is in a metastable state and the phase transition continues during the measurement.

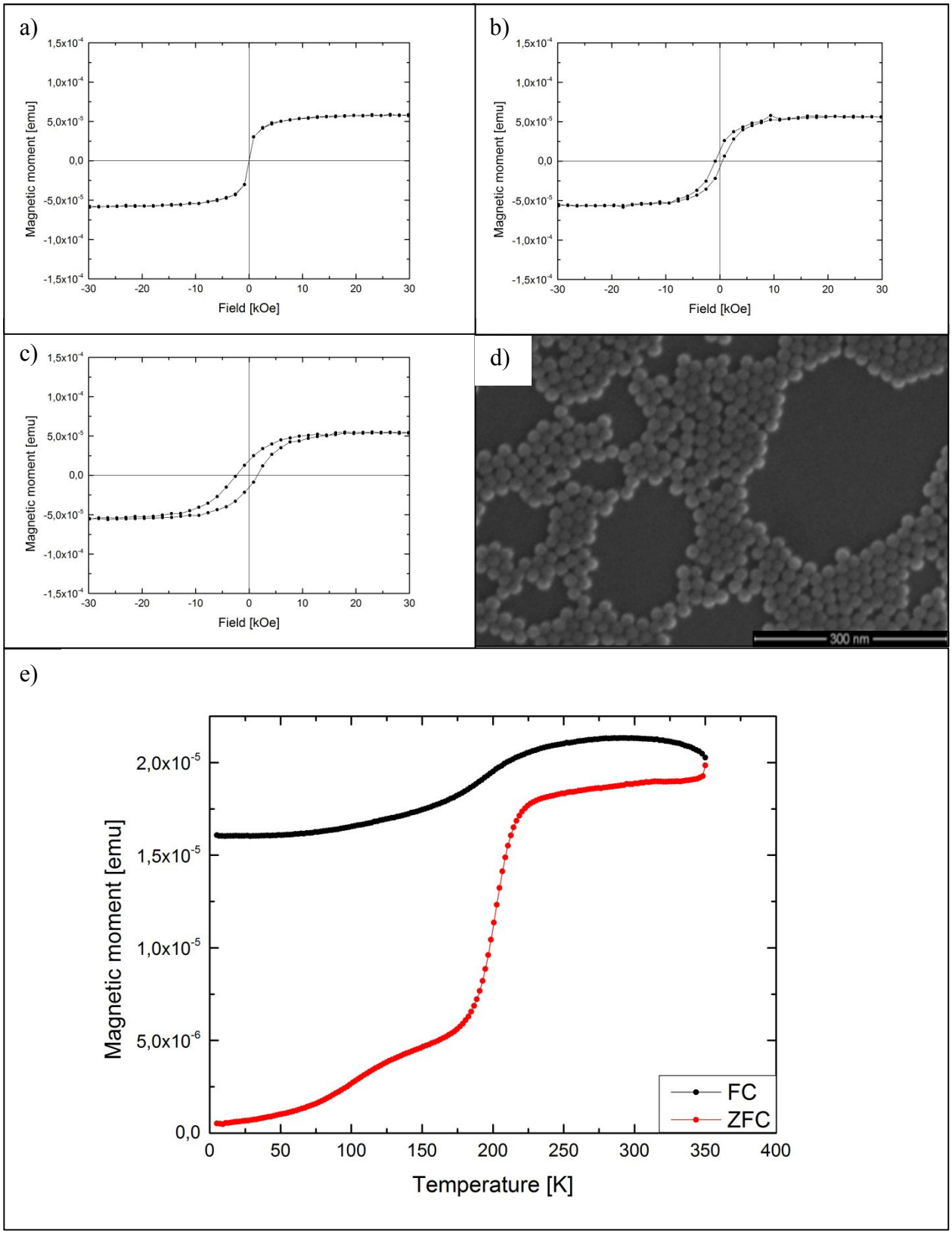

Figure 4.19: *Results for a sample diluted with toluene at a ratio of 1:30 and treated with oxygen plasma for 2 min. The hysteresis curves were measured at* ***a)*** *300 K,* ***b)*** *100 K and* ***c)*** *5 K and show superparamagnetic behavior. Additionally the curves obtained below the blocking temperature are shifted to the left due to exchange bias (Appendix C).* ***d)*** *SEM image of the sample.* ***e)*** *ZFC (red) and FC (black) curve measured in a field of 50 Oe. The amount of maghemite is increased at the expense of wustite.*

4.6.1.3.2 10 minutes

For a sample treated with oxygen plasma for 10 min the conversion of wustite to maghemite seems to be continued since the effect described in the previous chapter is enhanced: Figure 4.21 shows that the peak in the ZFC curve at 125 K has become dominant and is superimposed by the second peak at 198 K which has become comparably weak. Additionally the decrease in the FC curve below the blocking temperature is even smaller than in the curve obtained after 2 min of plasma treatment (Figure 4.19). The hysteresis curves that are shown in Figure 4.20 still exhibit superparamagnetic behavior and the exchange bias is also observable, but the coercive field strengths measured at 100 K and 5 K are significantly lower than in the previous chapters, hence the blocking temperature is reduced (Appendix C). This complies with the assumption of a raising amount of maghemite since its T_B is lower than the one observed for wustite.

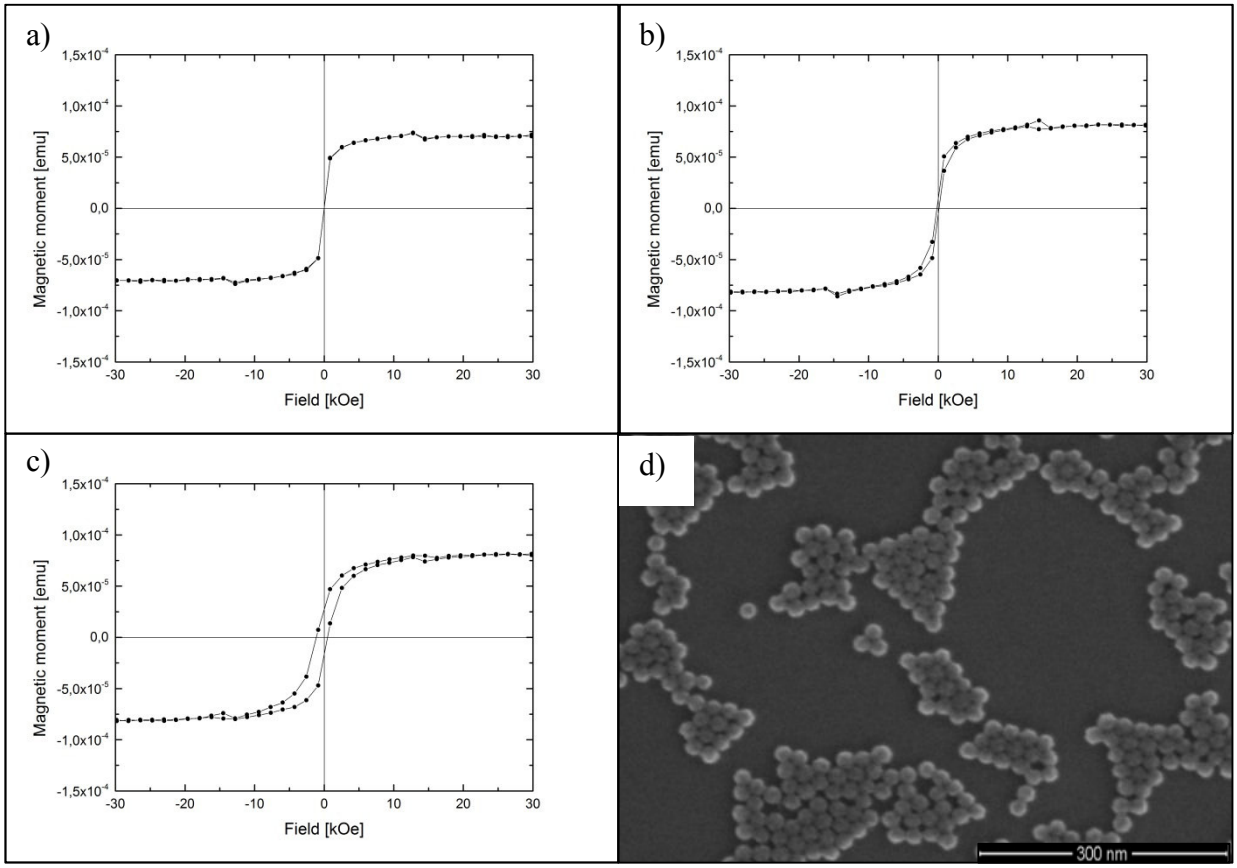

Figure 4.20: *Hysteresis curves of a sample diluted with toluene at a ratio of 1:30 and treated with oxygen plasma for 10 min measured at* ***a)*** *300 K,* ***b)*** *100 K and* ***c)*** *5 K that show superparamagnetic behavior. The blocking temperature is lowered compared to the samples treated with oxygen plasma for 2 min. Additionally the curves obtained below the blocking temperature are shifted to the left due to exchange bias (Appendix C).* ***D)*** *SEM image of the sample.*

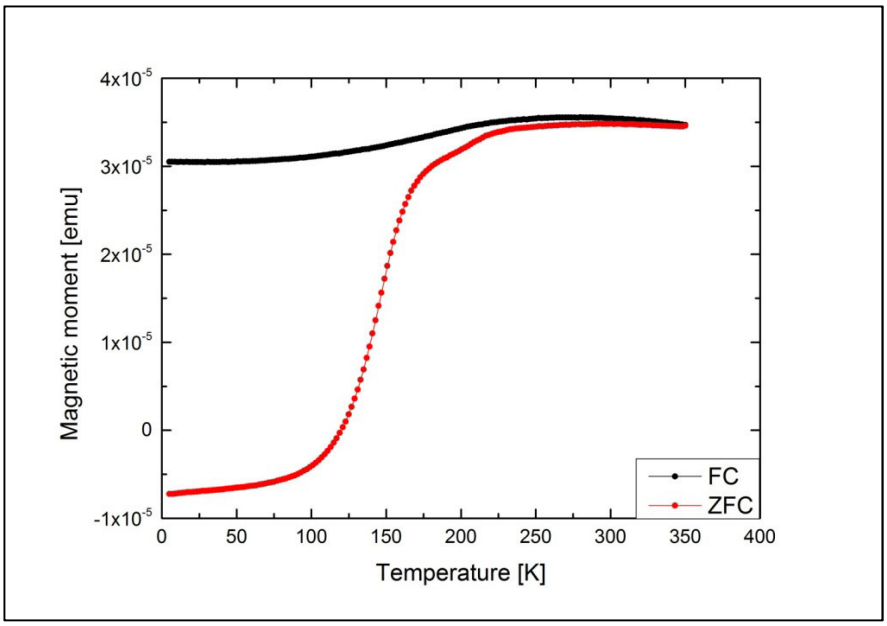

Figure 4.21: *ZFC (red) and FC (black) curve of a sample diluted with toluene at a ratio of 1:30 that was treated with oxygen plasma for 10 min measured in a field of 50 Oe. The amount of maghemite is further increased at the expense of wustite.*

4.6.1.3.3 30 minutes

After 30 min of oxygen plasma treatment the hysteresis measured at 100 K is still closed inducing that the blocking temperature is further decreased (Figure 4.23). Additionally the shape has become less rounded compared to the curves obtained before. Therefore the proportion of wustite seems to be further reduced. But the open hysteresis at 5 K is still shifted to the left; hence a small amount of wustite must be left causing exchange bias. Anyway there is no second peak observable in the ZFC curve at 198 K anymore (Figure 4.22), hence the proportion is too small to affect the overall magnetic behavior.

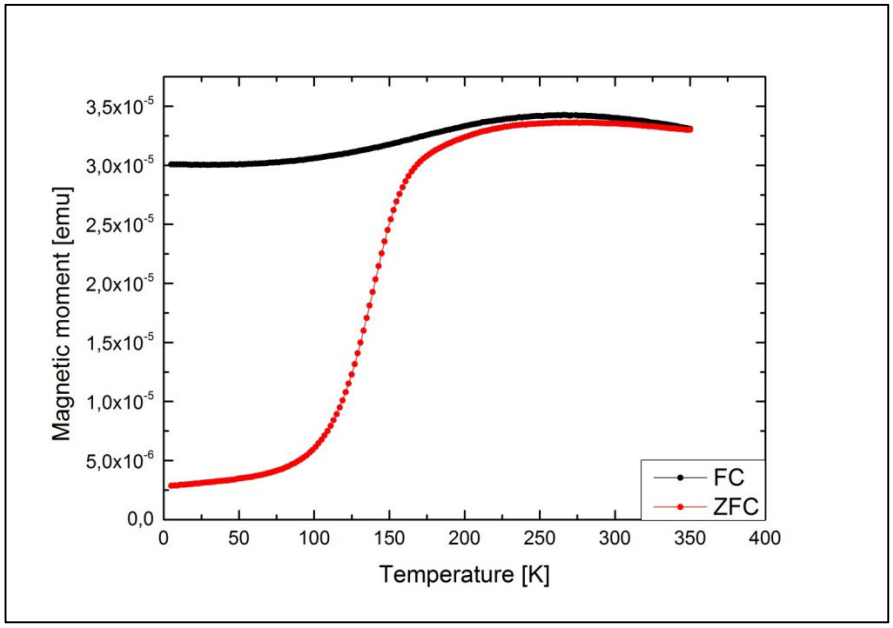

Figure 4.22: *ZFC (red) and FC (black) curve of a sample diluted with toluene at a ratio of 1:30 that was treated with oxygen plasma for 30 min measured in a field of 50 Oe. The amount of wustite is reduced to such an extent, that no influence can be observed anymore.*

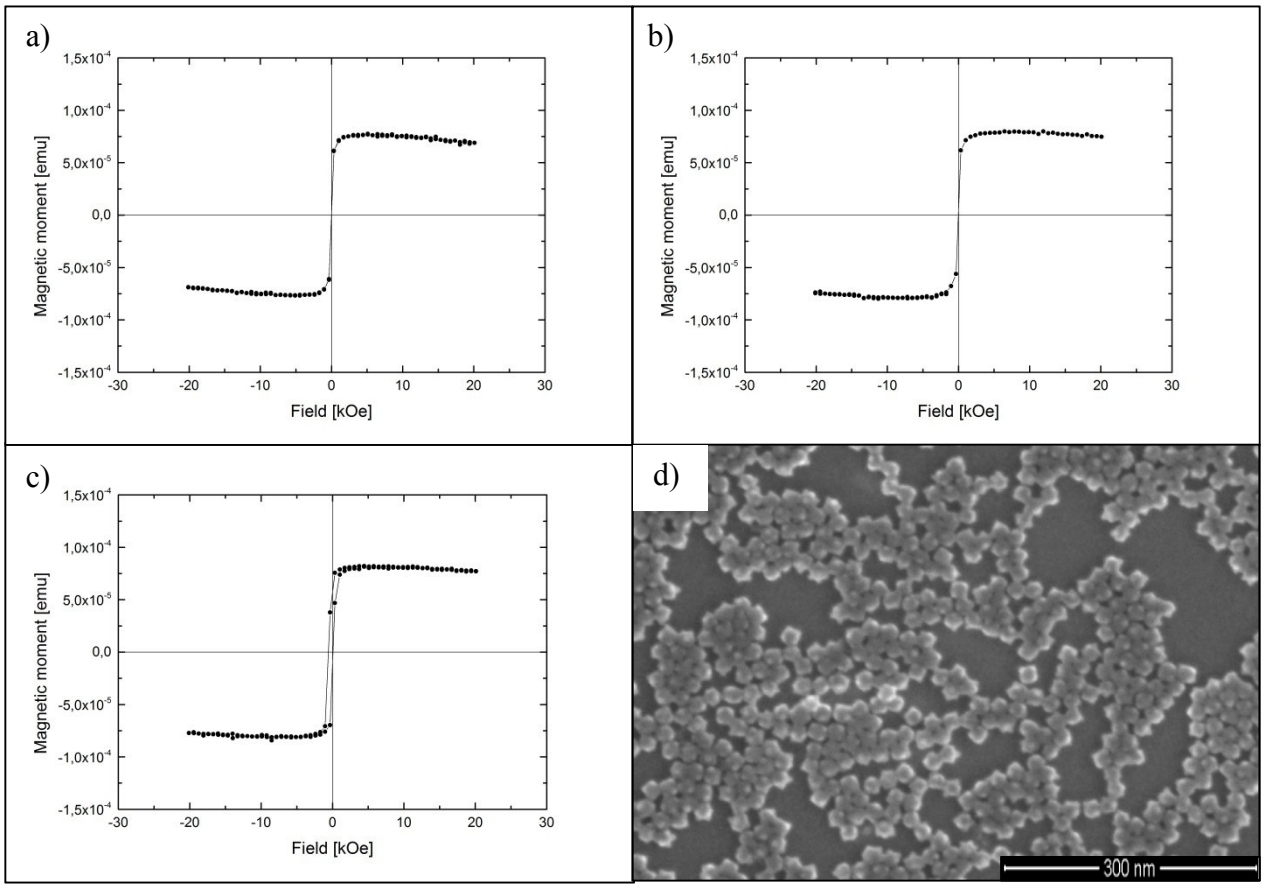

Figure 4.23: *Hysteresis curves for a sample diluted with toluene at a ratio of 1:30 and treated with oxygen plasma for 30 min measured at* ***a)*** *300 K,* ***b)*** *100 K and* ***c)*** *5 K that show superparamagnetic behavior and exchange bias (Appendix C). The blocking temperature is reduced and the shape has become less rounded because the amount of wustite has become very small.* ***d)*** *SEM image of the sample.*

4.6.1.4 Metal

The deposition of metal upon the samples is applied to tune the inter-particle interactions. To ensure that all the particles are covered, the colloid was diluted with toluene at a proportion of 1:30 (chapter 4.3) and deposited by spincoating as shown in chapter 4.2.3. Subsequently the oleic acid shell was removed by a plasma process with various etching times. One sample was left untreated in order to serve as reference. Finally, the particles were covered by 20 nm of niobium, gold, palladium or platinum using different deposition routes (chapter 4.5). Unfortunately, it was only possible to measure the samples covered with platinum or gold, respectively, due to restricted measurement time.

4.6.1.4.1 Platinum

Figure 4.24 shows the hysteresis and ZFC-FC curves of a sample without plasma treatment prior to metal deposition. It exhibits the same behavior as the sample shown in Figure 4.16 which was identically prepared but without platinum coating. Hence the metal could either have no impact on the magnetic properties or the oleic acid shell, which was not removed by a preceding plasma process, avoids interaction between the nanoparticles and the platinum matrix.

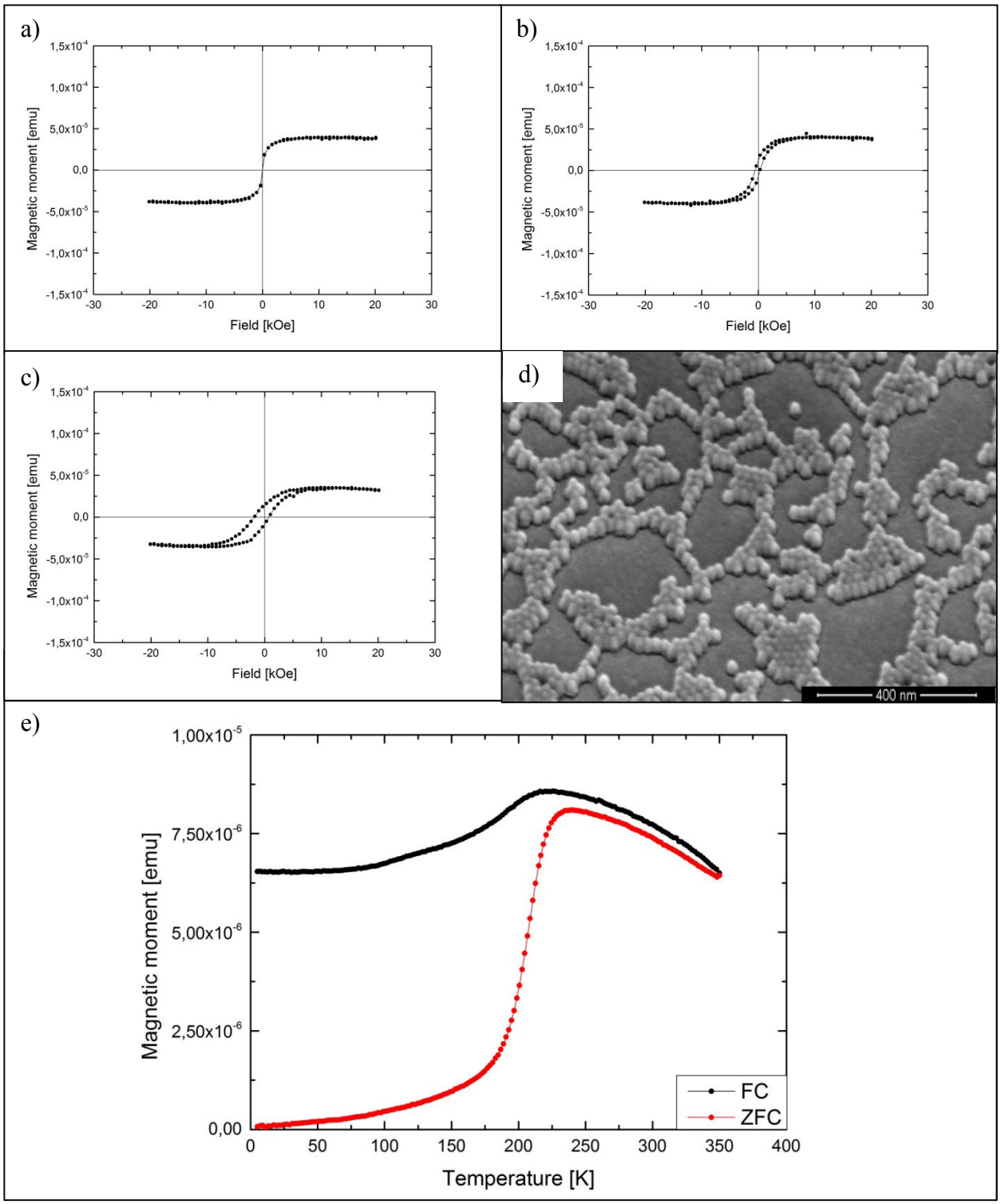

Figure 4.24: *Results for a sample diluted with toluene at a ratio of 1:30 without plasma treatment prior to the deposition of 20 nm of platinum by magnetron sputtering. The hysteresis curves were measured at* ***a)*** *300 K,* ***b)*** *100 K and* ***c)*** *5 K and show superparamagnetic behavior. Additionally the curves obtained below the blocking temperature are shifted to the left due to exchange bias (Appendix C).* ***d)*** *SEM image of the sample.* ***e)*** *ZFC (red) and FC (black) curve measured in a field of 50 Oe. The curves are similar to those obtained for the sample which was prepared identically but without platinum coating.*

The measurement results for the sample treated with oxygen plasma for 2 min prior to the deposition of platinum are showed in Figure 4.25. The curves are similar to those obtained for the sample which was treated with plasma for 30 min only (Figure 4.22 and Figure 4.23). As

proposed in chapter 4.6.1.3.1, 2 min of plasma treatment could lead to the formation of a metastable state in which wustite is transformed to maghemite. Hence the initiated conversion is either continued during storage prior to the measurement, or it proceeded due to the energy impact among metal deposition.

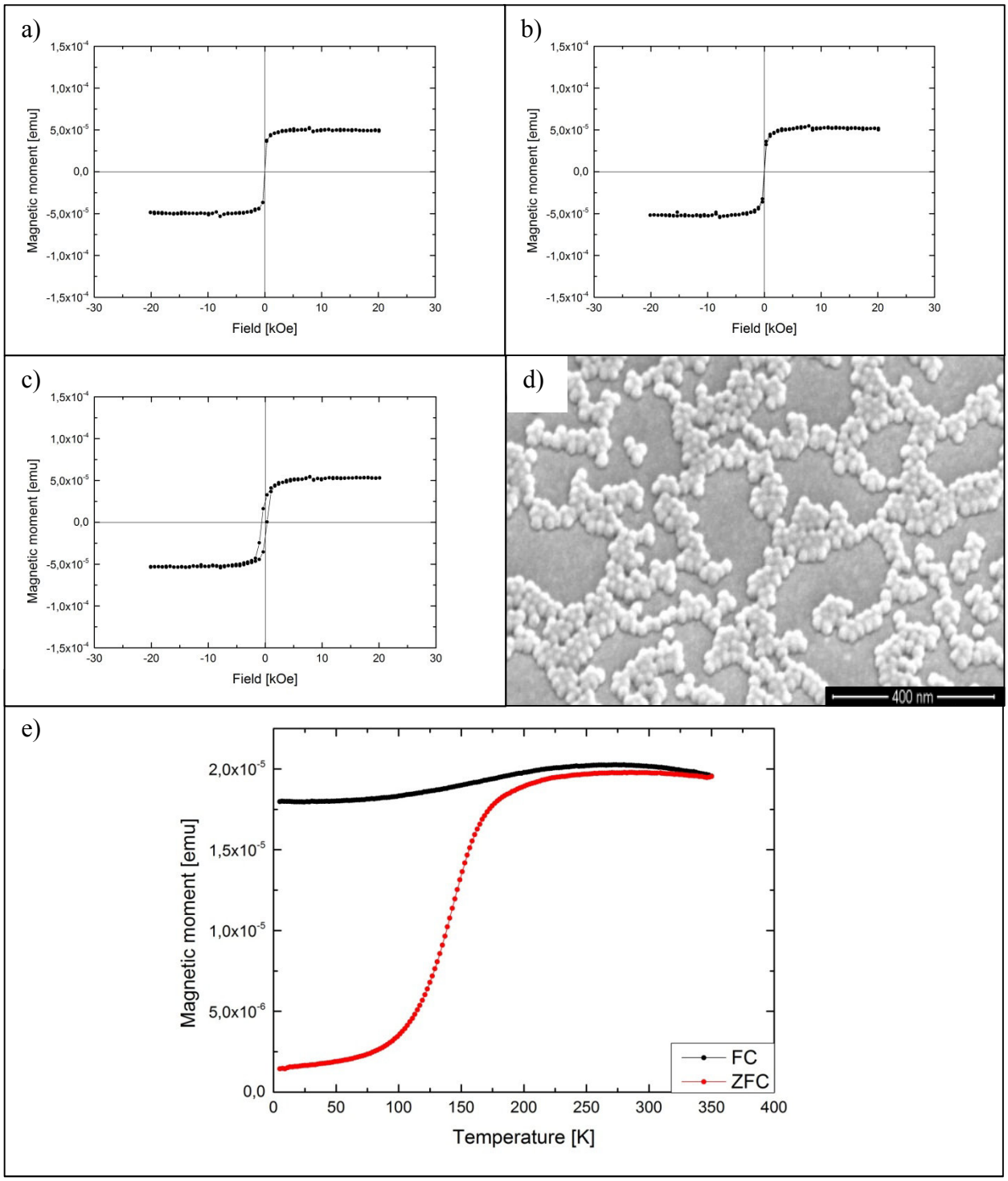

Figure 4.25: *Results for a sample diluted with toluene at a ratio of 1:30 and treated with oxygen plasma for 2 min prior to the deposition of 20 nm platinum by magnetron sputtering. The hysteresis curves were measured at* ***a)*** *300 K,* ***b)*** *100 K and* ***c)*** *5 K and show superparamagnetic behavior. Additionally the curves obtained below the blocking temperature are shifted to the left due to exchange bias (Appendix C).* ***d)*** *SEM image of the sample.* ***e)*** *ZFC (red) and FC (black) curve performed in a field of 50 Oe. The results are similar to those obtained for the sample treated with oxygen plasma for 30 min without platinum coating.*

The next sample was treated with oxygen plasma for 10 min prior to metal deposition. The ZFC-FC curves are depicted in Figure 4.26a. If it is examined in more detail (Figure 4.26b) an additional peak can be observed in the FC curve. This can be caused by the Verwey transition of magnetite. Hence the energy impact of the magnetron sputtering process in combination with 10 minutes of plasma treatment seems to be sufficient to transform maghemite to magnetite.

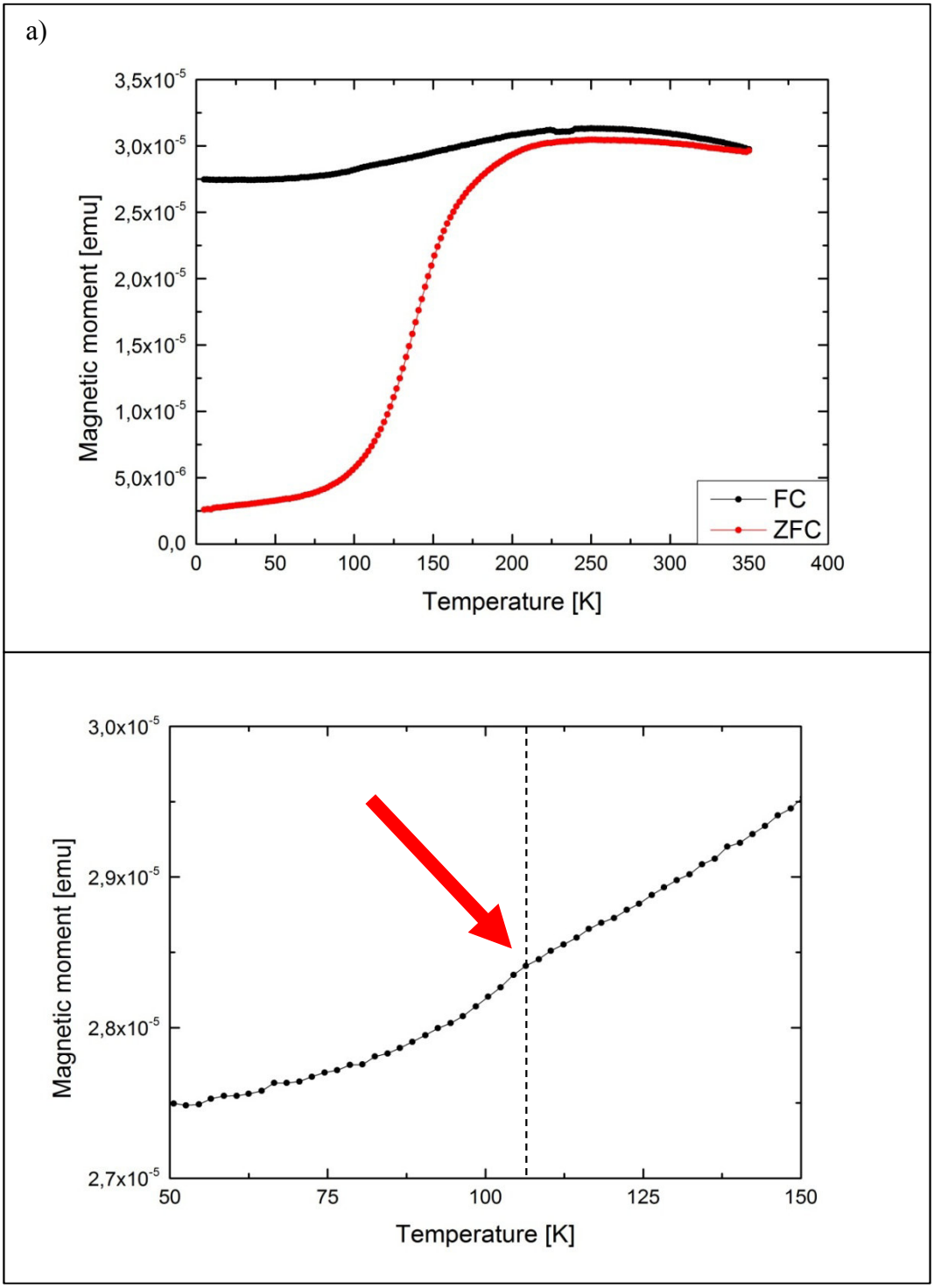

Figure 4.26: a) *ZFC (red) and FC (black) curve of a sample diluted with toluene at a ratio of 1:30 that was treated with oxygen plasma for 10 min prior to the deposition of 20 nm of platinum by magnetron sputtering. The measurements were performed in a field of 50 Oe. The curves are similar to those obtained for the sample treated with oxygen plasma for 2 min, but they exhibit an additional peak (Verwey transition).* ***b)*** *Magnification of the FC curve to show the Verwey transition.*

As shown in Figure 4.27 the nanoparticles still exhibit superparamagnetic behavior and exchange bias. Hence wustite is not transformed to maghemite completely though the energy impact seems to be high. The offset at approximately ± 10000 Oe is caused by measuring inaccuracies (it was the position of zero-crossing prior to the diamagnetic correction).

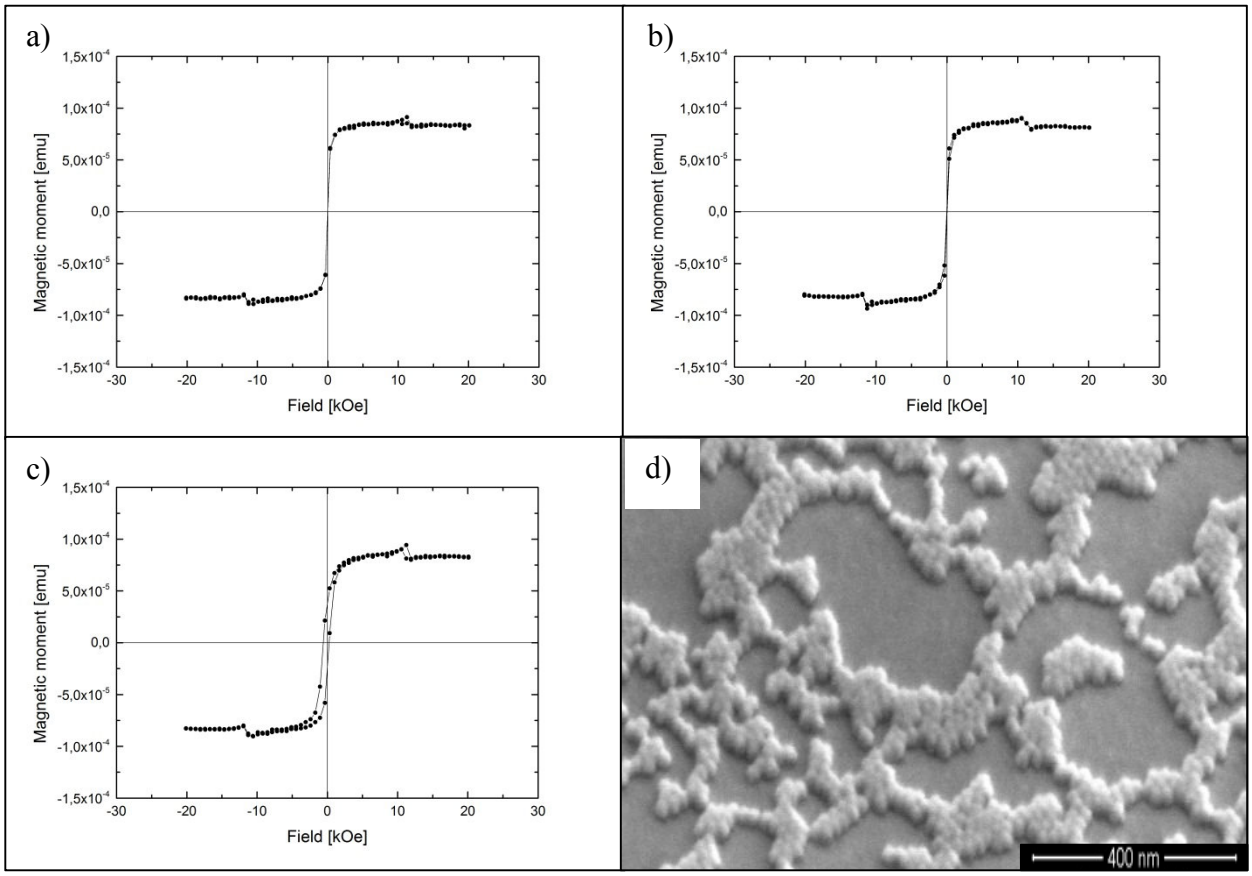

Figure 4.27: *Hysteresis curves of a sample diluted with toluene at a ratio of 1:30 and treated with oxygen plasma for 10 min prior to the deposition of 20 nm platinum by magnetron sputtering. The measurements were performed at* ***a)*** *300 K,* ***b)*** *100 K and* ***c)*** *5 K and show superparamagnetic behavior. Additionally the curves obtained below the blocking temperature are shifted to the left due to exchange bias (Appendix C). They are similar to those obtained for the sample treated with oxygen plasma for 2 min.* ***d)*** *SEM image of the sample.*

If the samples are treated with oxygen plasma for 30 min the effect can be enhanced as shown in Figure 4.28. The hystereses curves (Figure 4.29) are similar to those obtained for the samples treated for 10 min (Figure 4.27) hence the increased amount of magnetite seems to have no significant impact on blocking temperature and exchange bias.

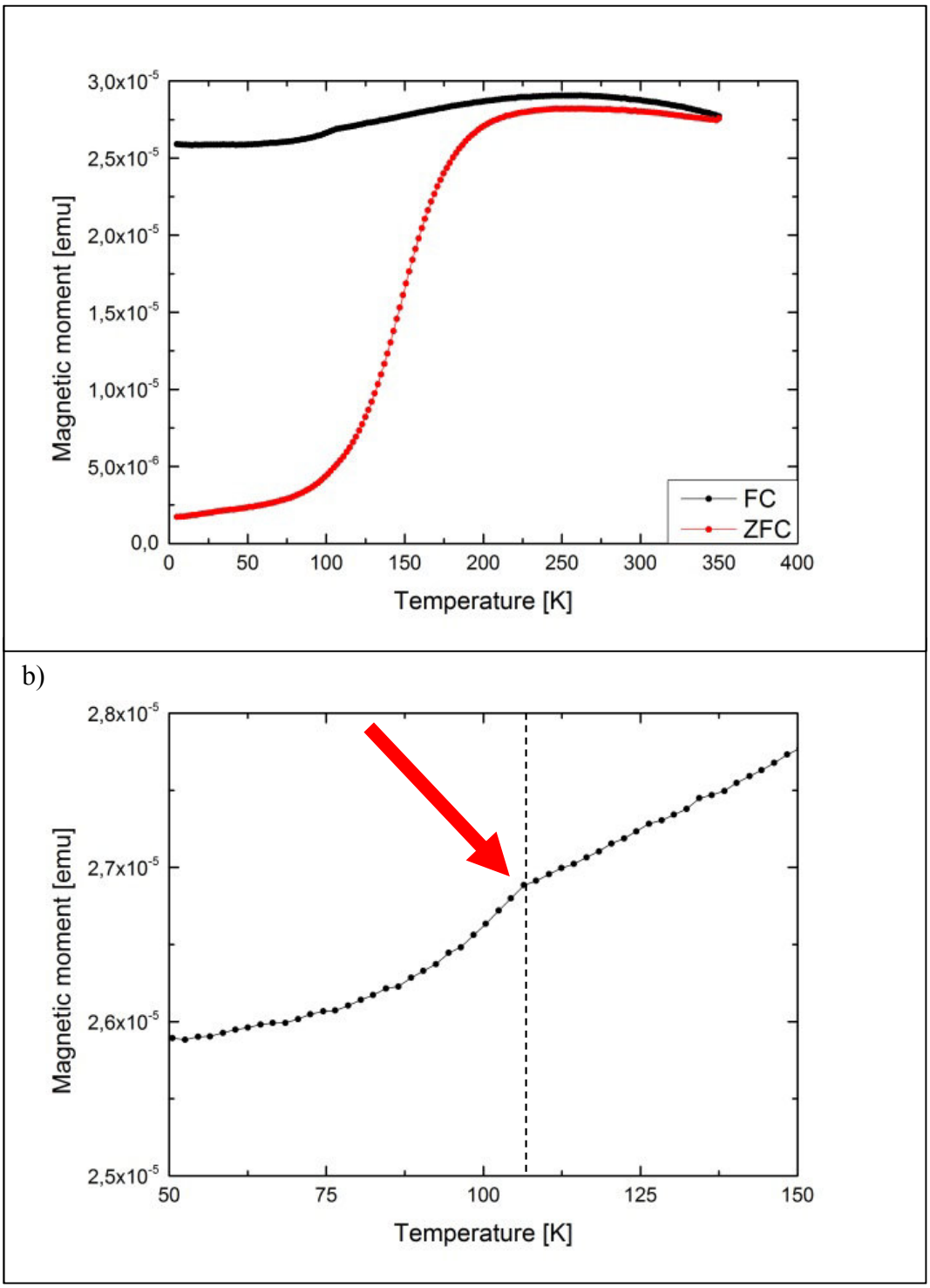

Figure 4.28: a) *ZFC (red) and FC (black) curve of a sample diluted with toluene at a ratio of 1:30 that was treated with oxygen plasma for 30 min prior to the deposition of 20 nm of platinum by magnetron sputtering. The measurements were performed in a field of 50 Oe. The transformation of maghemite is enhanced compared to a plasma treatment for 10 min.* ***b)*** *Magnification of the FC curve to show the Verwey transition.*

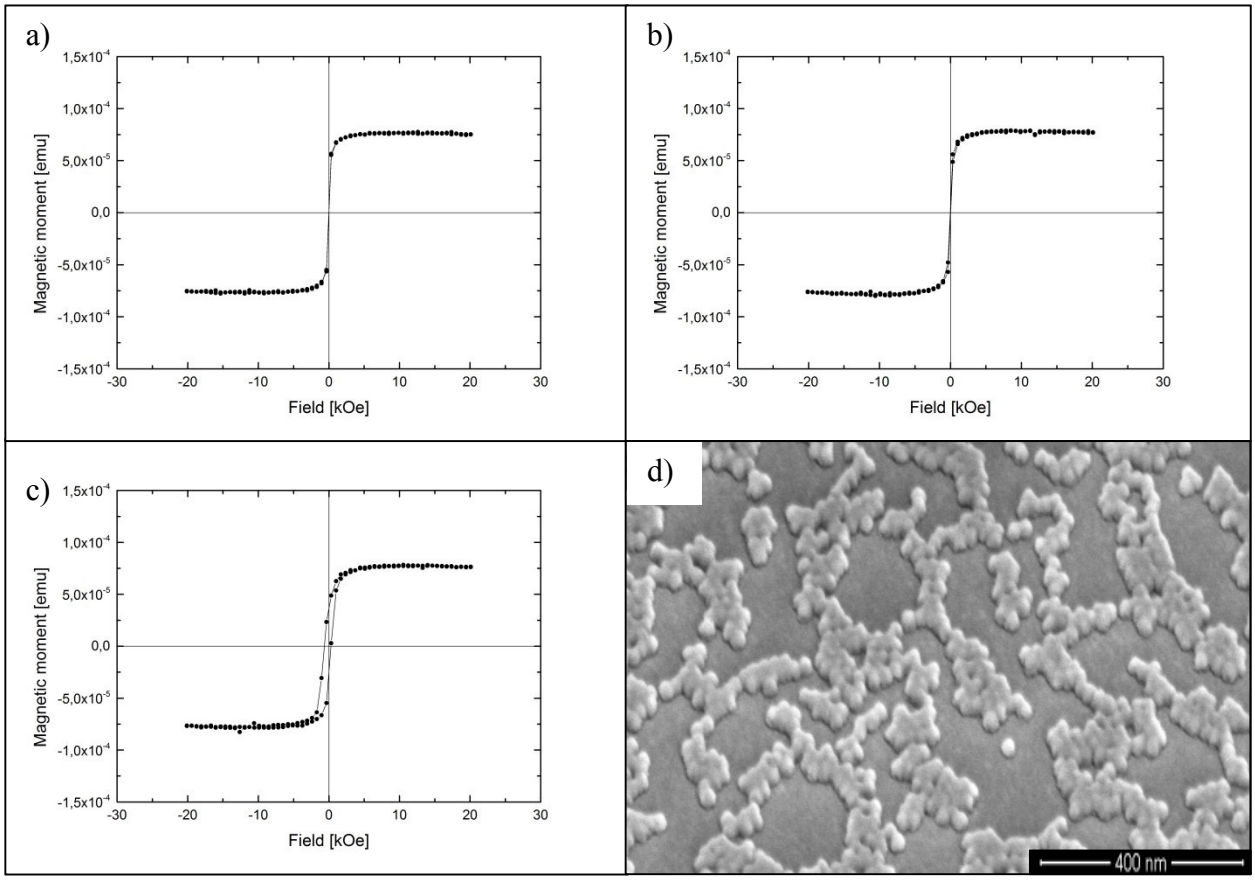

Figure 4.29: *Hysteresis curves for a sample diluted with toluene at a ratio of 1:30 and treated with oxygen plasma for 30 min prior to the deposition of 20 nm of platinum by magnetron sputtering. The measurements were performed at* ***a)*** *300 K,* ***b)*** *100 K and* ***c)*** *5 K and show superparamagnetic behavior. Additionally the curves obtained below the blocking temperature are shifted to the left due to exchange bias (Appendix C).* ***d)*** *SEM image of the sample.*

4.6.1.4.2 Gold

Analogously to the platinum samples 20 nm gold were deposited on some samples by magnetron sputtering. Unfortunately it was not possible to measure the hysteresis and ZFC-FC curves of the sample without plasma treatment prior to metal deposition due to restricted measurement time. Therefore the discussion starts with the sample that was treated for 2 min. Figure 4.30 shows the hysteresis curves. They are similar to those obtained for the platinum samples: They exhibit superparamagnetic behavior and exchange bias. The blocking temperature is comparable to the value obtained for samples without metal that were treated with plasma for 30 min.

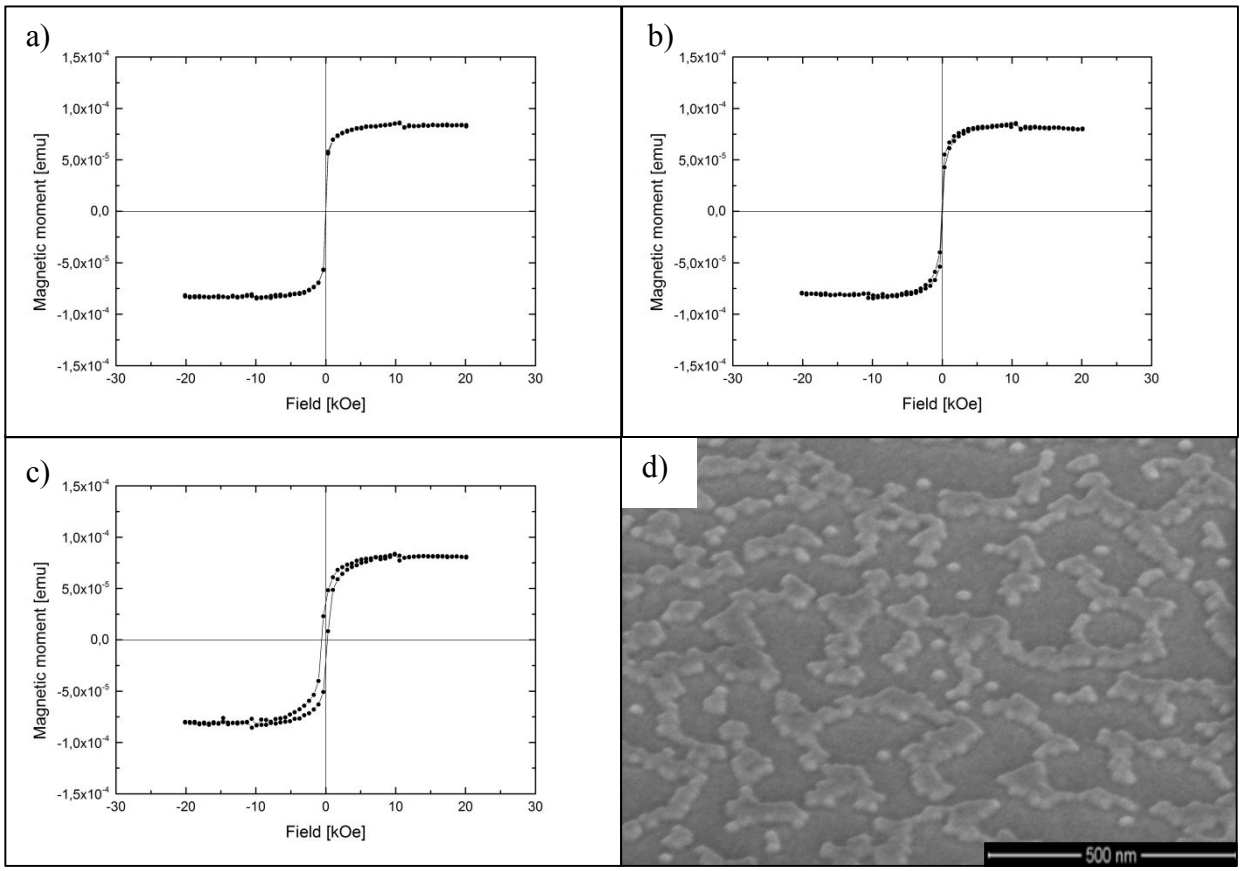

Figure 4.30: *Hysteresis curves of a sample diluted with toluene at a ratio of 1:30 and treated with oxygen plasma for 2 min prior to the deposition of 20 nm gold by magnetron sputtering. The measurements were performed at* ***a)*** *300 K,* ***b)*** *100 K and* ***c)*** *5 K and show superparamagnetic behavior. Additionally the curves obtained below the blocking temperature are shifted to the left due to exchange bias (Appendix C). They are similar to those obtained for platinum.* ***d)*** *SEM image of the sample.*

The ZFC-FC curves are depicted in Figure 4.31. They show that the transformation of wustite to maghemite which was induced by the plasma process (chapter 4.6.1.3.1) is continued but has not proceeded as much as for the platinum sample with the same plasma duration (Figure 4.25). In addition the Verwey transition described above cannot be observed. Hence there is no magnetite. For the reason that the duration between sample preparation, plasma treatment and MPMS measurement was identical this difference cannot originate from a phase transition during storage due to a metastable state. Indeed, the cause can be different energy impacts during the sputtering process, since the boiling point of gold is approximately 800 K lower than the one of platinum [124] [125].

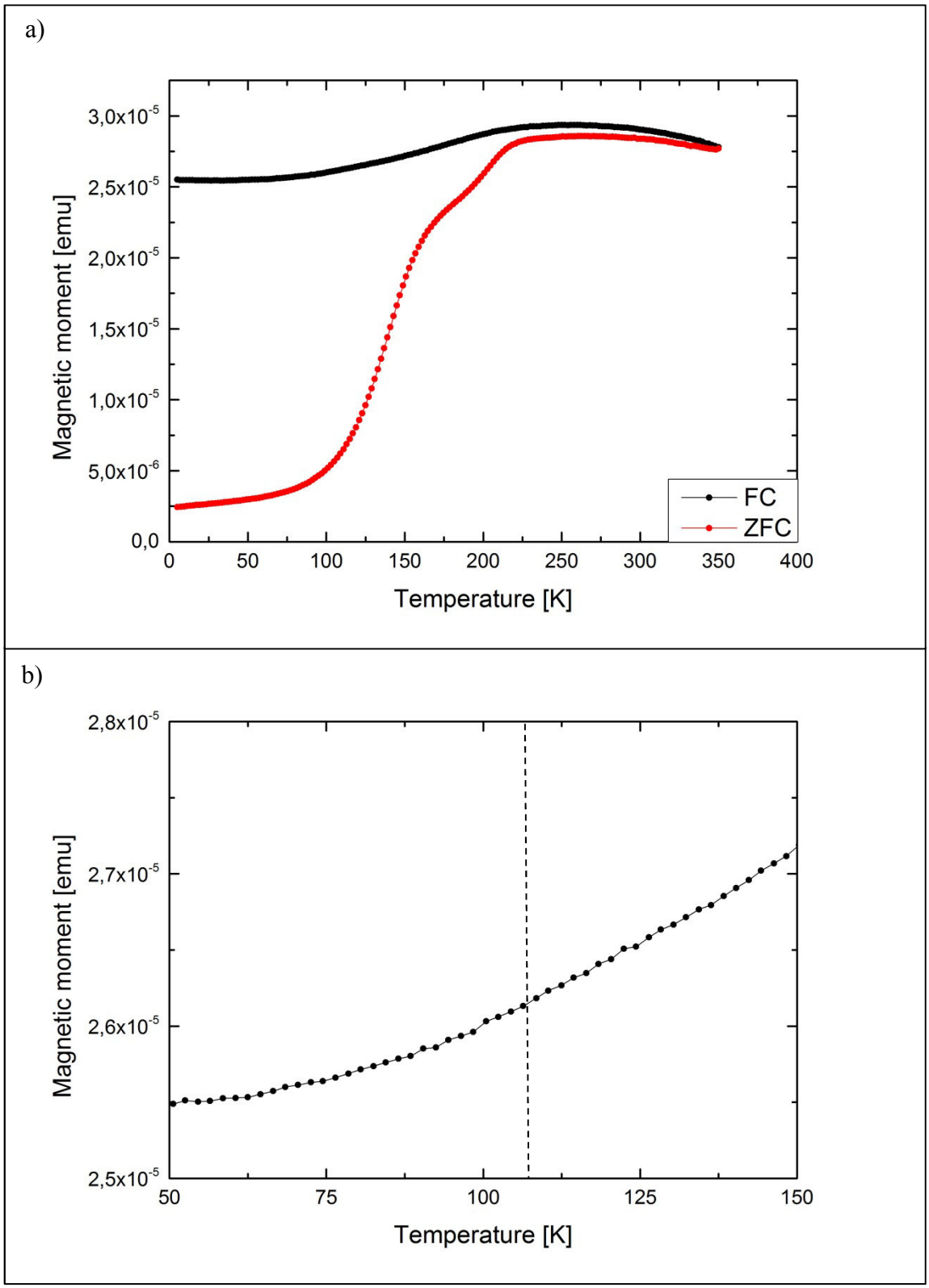

Figure 4.31: a) *ZFC (red) and FC (black) curve of a sample diluted with toluene at a ratio of 1:30 that was treated with oxygen plasma for 2 min prior to the deposition of 20 nm of gold by magnetron sputtering. The measurements were performed in a field of 50 Oe. The curves are similar to those obtained for the sample treated with oxygen plasma for 10 min without metal deposition.* ***b)*** *Magnification of the FC curve to show that there is no Verwey transition.*

If the plasma duration is increased to 10 min or even to 30 min the phase transition of wustite to maghemite is proceeded as much as if there was not metal deposition on a sample treated with oxygen plasma for 30 min (Figure 4.32). Hence the energy impact upon gold sputtering is sufficient for the transition to maghemite but not high enough to produce magnetite.

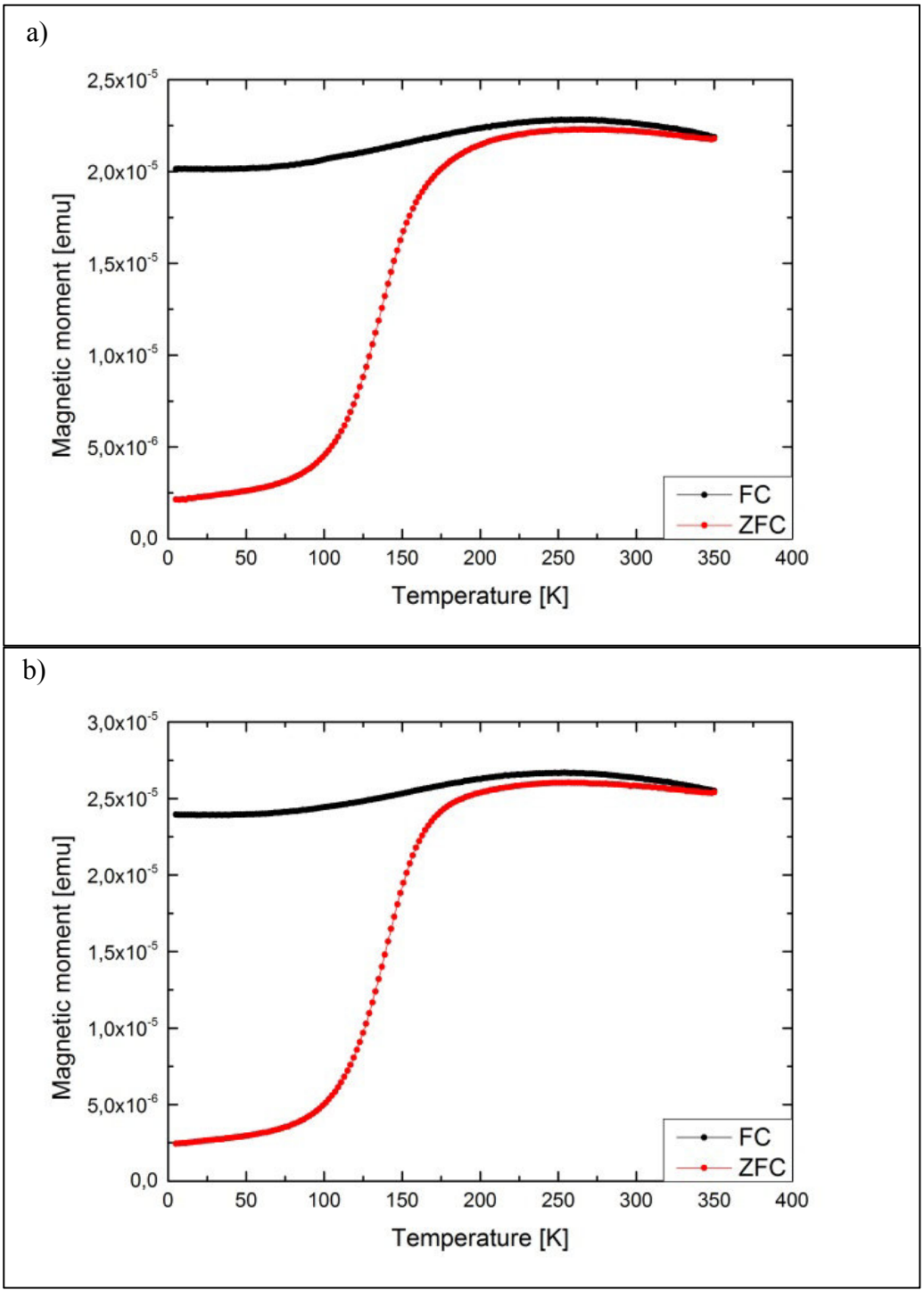

Figure 4.32: *ZFC (red) and FC (black) curves of samples diluted with toluene at a ratio of 1:30 on which 20 nm of gold were deposited by magnetron sputtering after oxygen plasma treatment for* ***a)*** *10 min and* ***b)*** *30 min, respectively. The measurements were performed in a field of 50 Oe. The curves are similar to those obtained for the sample treated with oxygen plasma for 30 min only.*

The hysteresis curves which are depicted in Figure 4.33 also show the same behavior as the ones obtained for the platinum samples: A superparamagnetic behavior can be observed as well as exchange bias and a low blocking temperature.

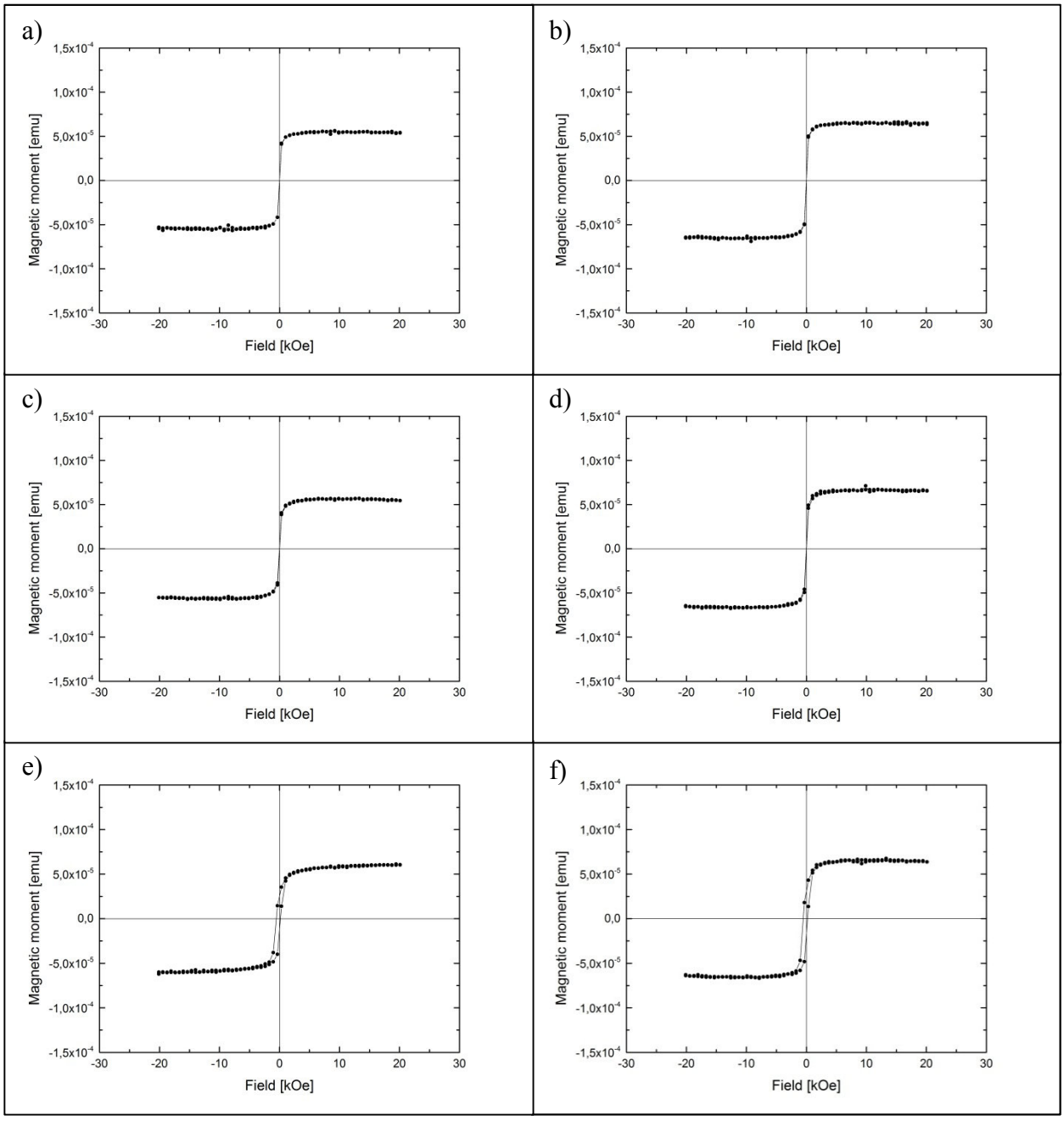

Figure 4.33: *Hysteresis curves of samples diluted with toluene at a ratio of 1:30 and treated with oxygen plasma for* ***a,c,e)*** *10 min or* ***b,d,f)*** *30 min prior to the deposition of 20 nm gold by magnetron sputtering. The measurements were performed at* ***a,b)*** *300 K,* ***c,d)*** *100 K or* ***e,f)*** *5 K, respectively. They show superparamagnetic behavior and the curves obtained below the blocking temperature are shifted to the left due to exchange bias (Appendix C). They are similar to those obtained for platinum.*

4.6.2 Interactions

To analyze the magnetic interactions of nanoparticles the so-called 'memory effect' can be examined. Therefore the ZFC curve is once measured in a regular way as shown in the previous chapter. Afterwards a second ZFC curve is recorded with an aging stop during cool down at a temperature T_a above the blocking point for a certain time t_a. During that time the spin configuration gets arranged towards the equilibrium state which is frozen when the temperature is subsequently lowered to 5 K. On reheating the memory is retrieved. If the system behaves as spin glass or super spin glass the aged ZFC curve shows a little dip close to the aging temperature. To better illustrate the effect the difference function of the measurements is plotted [29] [30].

All samples that were supposed to be investigated with this method were treated with oxygen plasma for 30 min and exhibited a blocking temperature below 100 K (chapter 4.6.1). Since the effect is stronger at lower T_a and with large t_a, a temperature of 140 K and an aging time of 10000 s were chosen.

The result for the sample diluted with toluene at a proportion of 1:30 that was treated with oxygen plasma for 30 min is depicted in Figure 4.34. Since the peak is clearly visible and the particles are superparamagnetic (chapter 4.6.1.3.3), the system is a super spin glass. Hence the nanoparticles are in a disordered, collective state with strong dipole-dipole interaction what agrees with the assumption made in chapter 4.3.

Unfortunately the field cannot be set to a value of exactly zero. Therefore the conditions during cool down are not identical leading to an overall offset of approximately $2 \cdot 10^{-7}$ emu between the ZFC curves.

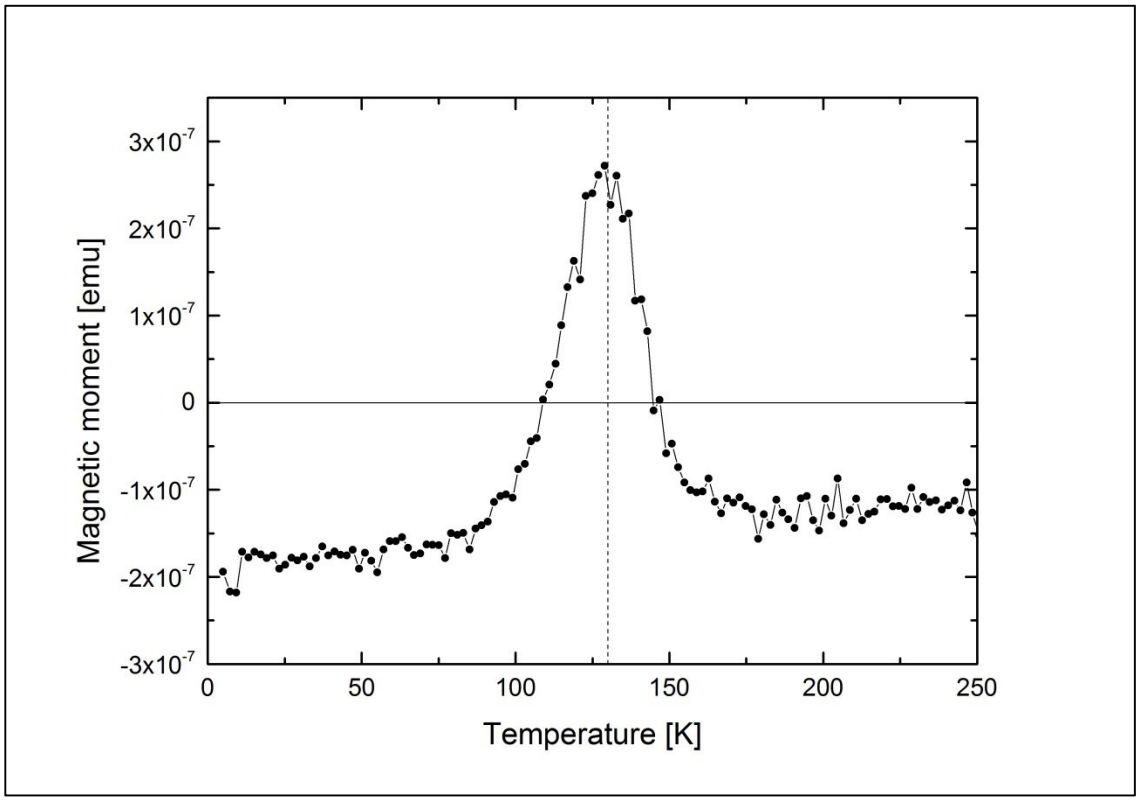

Figure 4.34: *Difference between regular ZFC curve and the ZFC curve obtained with an aging stop at 140 K for 10000 s of a sample diluted with toluene at a proportion of 1:30 and 30 min oxygen plasma treatment. The peak is caused by super spin glass behavior.*

To further confirm the assumption of strong dipolar interactions between the particles so-called 'delta-M' measurements were performed [126]. Therefore two curves were required: For the so-called 'dc-demagnetization remanence' (DCD) curve, which is measured at a temperature of 5 K, a strong magnetic field of -10 000 Oe is applied to magnetize the sample in negative saturation. Subsequently a certain positive magnetic field is applied for 10 s, then set to zero and the remanent magnetization is measured after a delay of 10 s. This procedure is then repeated with a magnetic field increased by ΔH until saturation is observed in the emerging curve. For this thesis ΔH = 100 Oe was chosen, starting at 0 Oe. The second curve is called 'isothermal remanence' (IRM). The measurement procedure is the same as for the DCD curve but the sample is demagnetized instead of negatively magnetized at the beginning. Finally the delta-M curve is calculated as follows [126] [127]:

$$M_r(H) = \frac{M_{IRM}(H)}{M_s} \tag{4-1}$$

$$M_d(H) = \frac{M_{DCD}(H)}{M_s} \tag{4-2}$$

$$delta\text{-}M(H) = 2M_r(H) + M_d(H) - 1 \tag{4-3}$$

Where M_s is the saturation magnetization which is $-2.38753 \cdot 10^{-5}$ for the sample without metal coating. The coercive field strength obtained after demagnetization is 172 Oe. As shown in Figure 4.35 the peak in the delta-M curve is negative, hence there is a *demagnetizing* interaction between the particles which is attributed to dipole-dipole interaction in literature [128] [129] [130] [131]. This complies with the results obtained from the memory-effect measurements.

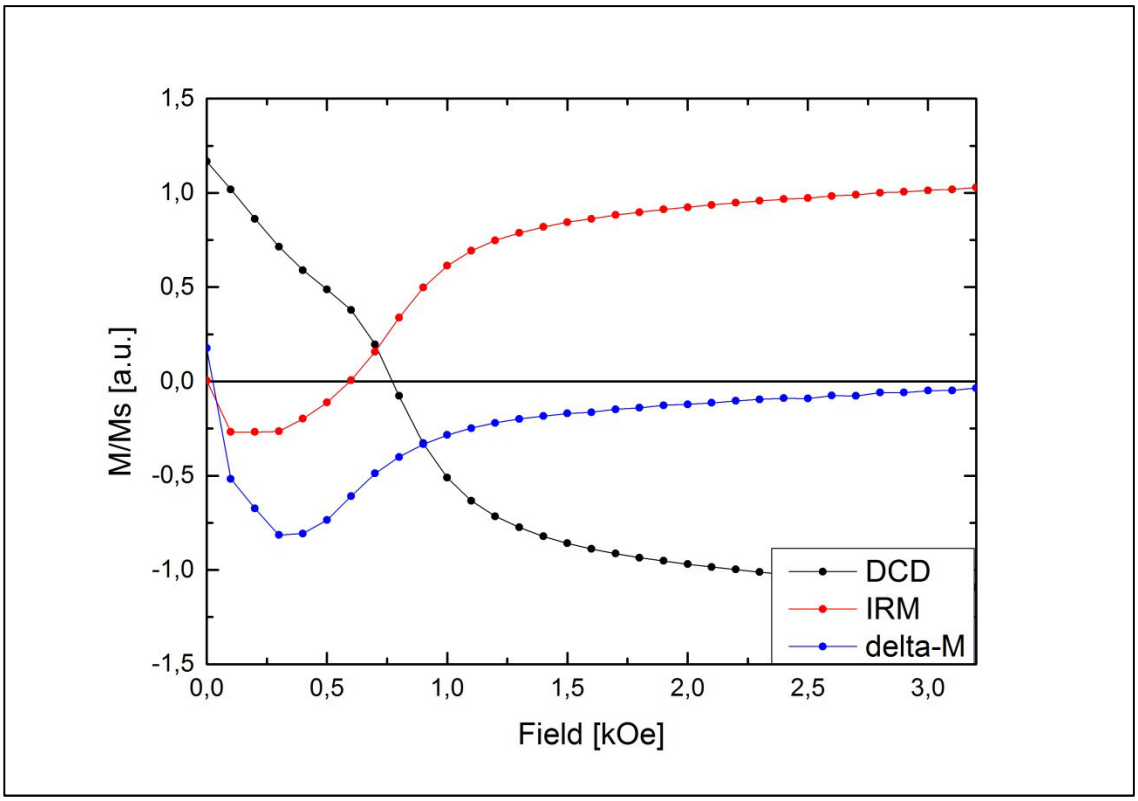

Figure 4.35: *DCD (black), IRM (red) and delta-M (blue) curves of a sample diluted with toluene at a proportion of 1:30 and treated with oxygen plasma for 30 min. Since the peak in the delta-M curve is negative there is a demagnetizing interaction which is attributed to dipolar interactions.*

Subsequently an identical sample was produced but additionally covered with 20 nm of platinum by magnetron sputtering. Figure 4.36 shows the memory-effect measurement. It exhibits a peak at the same position as the sample without Pt but has only half the height; hence the super spin glass order is partially suppressed. A larger distance of the nanoparticles can be excluded as cause due to identical preparation. In addition the sample contains a small amount of magnetite, unlike the sample without metal coating. This would rather increase the effect due to larger magnetic moments (M_s = -5,26659·10^{-5}). Hence the reduced dipole-dipole interaction seems to be caused by the platinum matrix.

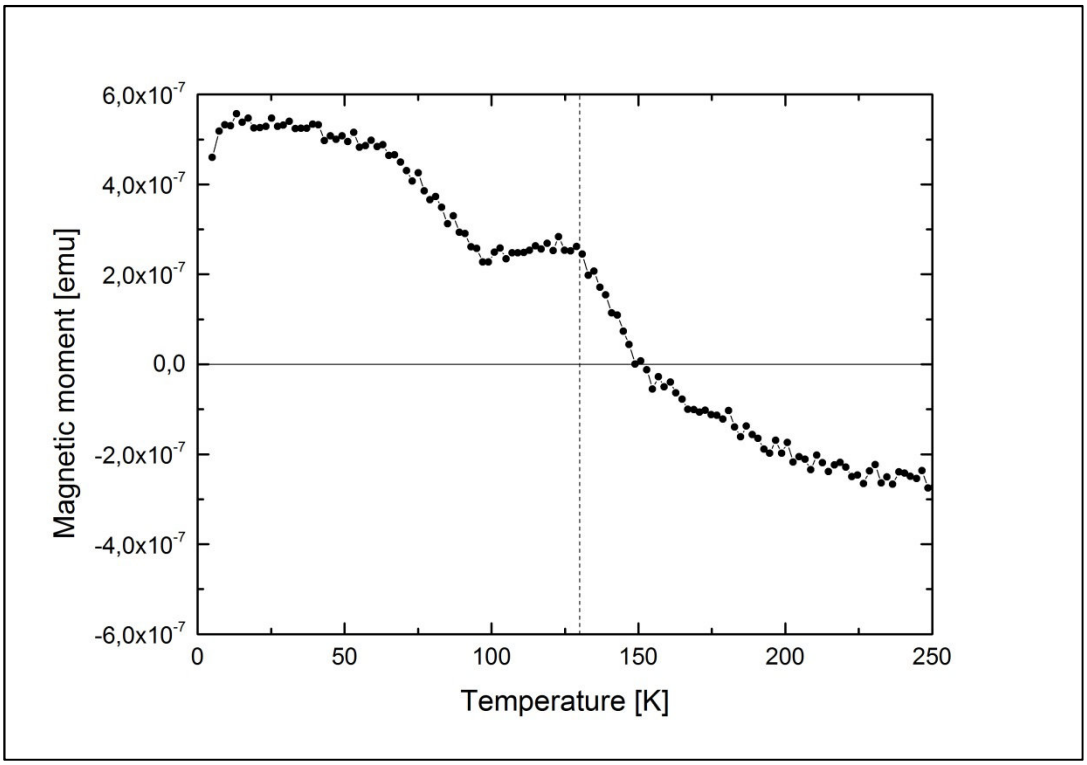

Figure 4.36: *Difference between regular ZFC curve and the ZFC curve obtained with an aging stop at 140 K for10000 s of a sample diluted with toluene at a proportion of 1:30 and 30 min oxygen plasma treatment prior to the deposition of 20 nm of platinum by magnetron sputtering. The peak is caused by super spin glass behavior but its height is reduced by Pt which weakens the dipole-dipole interaction.*

Figure 4.37 shows the corresponding delta-M measurement. The peak is positive, hence there is a *magnetizing* interaction which is often attributed to exchange interaction in literature [128] [129] [130] [131]. Since the particles are not in direct contact this seems to be caused by the platinum layer which becomes polarized by the nanoparticles [15] [49] [132].

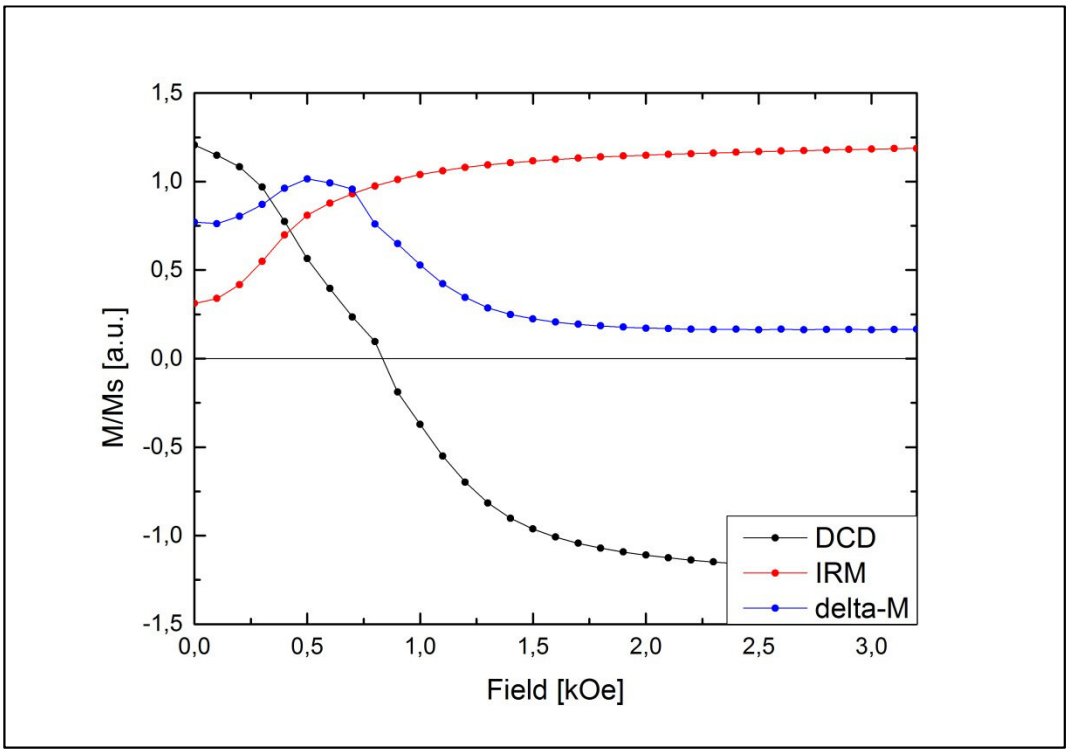

Figure 4.37: *DCD (black), IRM (red) and delta-M (blue) curves of a sample diluted with toluene at a proportion of 1:30 and treated with oxygen plasma for 30 min prior to the deposition of 20 nm of platinum by magnetron sputtering. Since the peak in the delta-M curve is positive there is a magnetizing interaction which is attributed to exchange interaction.*

5 Summary

Commercially available iron oxide nanoparticles, supplied by Ocean NanoTech LLC, with a diameter of approximately 20 nm and a spherical shape were studied in this thesis. The nanoparticles were delivered with an oleic acid shell of 0-5 nm for steric stabilization and dispersed in toluene.

This colloid was transferred onto silicon wafers by three deposition routes: Sedimentation, drop-casting and spincoating. For the reason that the latter was the only one that provided a smooth, homogeneous surface, it was chosen to prepare all the samples with this method. In addition the film thickness is easily controllable by rotational speed and spinning duration.

For the reason that metal was supposed to be deposited later on, it was important to produce a (sub-)monolayer of nanoparticles upon the substrate to ensure that every particle is in contact with the metal. Therefore the colloid was diluted with toluene in different proportions. The best result was achieved for a ratio of 1:30 which was therefore used for all subsequent samples.

To allow the nanoparticles to interact the oleic acid shell had to be removed in the next step. Hence the colloid was diluted with acetone instead of toluene. Unfortunately, its volatility is higher than for toluene in such an extent that the liquid surface became unstable due to disjoining pressure during the spincoating process. This led to hole formation with rings of highly ordered nanoparticles and particle accumulation at the edge. It was shown that this behavior was not caused by the ultrasonic bath that was applied to avoid agglomeration after adding acetone. As explained above, such an inhomogeneous particle distribution was not suitable for further sample preparation. Therefore another approach in the form of oxygen plasma was chosen. For the reason that it was not possible to quantify the oleic acid shell, different treatment durations (2 min, 10 min, 30 min) were applied. Only for the sample treated for 30 min a visual change could be observed: The particles had become more cubic, hence a phase transition seemed to have occurred.

To further investigate the effect of the plasma treatment, all the samples were measured in a SQUID magnetometer. Therefore the ZFC-FC curves were obtained, as well as hysteresis curves at three different temperatures: 300 K, 100 K and 5 K. It was demonstrated that there were no differences in those measurements for samples diluted with toluene or acetone. In comparison to the undiluted sample the behavior also stayed the same except for the saturation magnetization which was reduced due to a lower number of nanoparticles. The hysteresis curves showed superparamagnetic behavior and a horizontal shift which was attributed to exchange bias. The ZFC-FC curves of the untreated sample in combination with literature data revealed that the particles consisted of maghemite and wustite. It had been demonstrated that with increasing oxygen plasma duration the amount of maghemite was increased at the expense of wustite with no effect on the superparamagnetic behavior or exchange bias except for a reduced blocking temperature with increasing amount of maghemite.

In the next step 20 nm of platinum, gold, palladium or niobium were deposited on the samples by different deposition routes (magnetron sputtering, molecular beam evaporation or IBS, respectively). For the reason that the oleic acid shell could not be established, four samples were prepared for every metal: 2 min, 10 min and 30 min of plasma treatment and an additional sample without plasma prior to metal deposition as reference. Unfortunately only the Pt and Au

samples could be measured by MPMS due to restricted measurement time. While the reference sample for Pt exhibited the same behavior as the sample without platinum coating, the sample treated with oxygen plasma for two minutes prior to metal deposition seemed to be comparable to the sample treated with plasma for 30 min without metal coating. Hence it was assumed that the transformation of wustite to maghemite could be initiated by plasma and sputtering but a critical energy impact had to be overcome. Therefore plasma treatment on its own was not sufficient but in combination with 2 min of plasma a metastable state was created, hence the transformation could occur. This assumption was further confirmed by the measurements with increased plasma duration. Additionally a Verwey transition was observed for plasma durations of 10 min or 30 min, respectively, indicating a transition from maghemite to magnetite. This was assumed to arise from the increased total energy impact. For the samples covered with gold a similar behavior could be observed. But for the reason that the energy impact on gold sputtering is lower the effect is attenuated. Hence 2 min of plasma treatment were not sufficient for an almost complete wustite transformation and there was no Verwey transition at all, hence there was no magnetite.

Finally the interactions between the nanoparticles were specifically investigated by memory and delta-M measurements. Therefore a sample treated with plasma for 30 min was compared to a similar sample that was additionally covered with 20 nm of Pt. For the reference sample a memory effect could clearly be established hence the particles behave as super spin glass with a strong dipole-dipole interaction in a disordered, collective state. This assumption was further confirmed by the delta-M measurement that also exhibited dipolar interactions. For the sample covered with Pt the memory effect occurred to be less intense indicating weaker super spin glass ordering. Excluding larger particle distance and smaller magnetic moments the cause seemed to be the platinum matrix. This was further confirmed by the delta-M measurement that revealed a positive peak which is attributed to exchange interaction in literature. For the reason that the particles are not in direct contact the effect still seems to be caused by the matrix.

Since the measurement time at the MPMS was restricted, several measurements have to be complemented such as the ZFC-FC and hysteresis curves for the reference sample for gold or all the samples covered with palladium and niobium. Additional memory-effect and delta-M measurements of a sample covered with palladium or niobium would be interesting to compare the effect on interactions. The gold sample could serve as valuable reference matrix-system, hence there is no effect on the interactions expected. For the reason that results obtained for the platinum sample seem to be better than expected they should be confirmed for example by XMCD measurements. Furthermore it would be interesting to observe if the transformation process is reversible for example by hydrogen plasma treatment.

6 References

[1] B. S. Baigrie, Electricity and magnetism: a historical perspective, USA: Greenwood Publishing Group, Inc., 2007.

[2] J. M. D. Coey, "Magnetism in future," *Journal of Magnetism and Magnetic Materials,* Vols. 226-230, pp. 2107-2112, 2001.

[3] W. Gilbert, De Magnete, UK, 1600.

[4] W. Wu, Q. He and C. Jiang, "Magnetic Iron Oxide Nanoparticles: Synthesis and Surface Functionalization Strategies," *Nanoscale Research Letters,* vol. 3, pp. 397-415, 2008.

[5] M. N. Baibich, J. Broto, A. Fert, F. Nguyen Van Dau, F. Petroff, P. Eitenne, G. Creuzet, A. Friederich and J. Chazelas, "Giant Magnetoresistance of (100)Fe/(001)Cr Magnetic Superlattices," *Physical Review Letters,* vol. 61, pp. 2472-2474, 1988.

[6] G. Binasch, P. Grünberg, F. Saurenbach and W. Zinn, "Enhanced magnetoresistance in layered magnetic structures with antiferromagnetic interlayer exchange," *Physical Review B,* vol. 39, pp. 4828-4830, 1989.

[7] G. Bacher, *Einführung in die Nanotechnologie,* Germany: Vorlesungsmanuskript (Universität Duisburg-Essen), 2009.

[8] U. Schiele-Trauth, „ingenieur.de,“ [Online]. Available: http://www.ingenieur.de/Fachbereiche/Mikro-Nanotechnik/Nano-Gold-im-Kirchenfenster.

[9] M. M. Freundlich, "Origin of the Electron Microscope," *Science,* vol. 142, no. 3589, p. 185188, 2008.

[10] P. A. Zawislak, L. F. Marques, P. Esteves and F. Rublescki, "Technological trajectories and multidimensional impacts: further remarks on the nanotechnology industry," *Journal of Business Chemistry,* pp. 47-64, 2010.

[11] O. Petracic, "Superparamagnetic nanoparticle ensembles," *Superlattices and Microstructures,* vol. 47, pp. 569-578, 2010.

[12] B. D. Terris and T. Thomson, "Nanofabricated and self-assembled magnetic structures as data storage media," *Journal of Physics,* vol. 38, pp. R199-R222, 2005.

[13] M. P. Pileni, "Self-Assembly of Inorganic Nanocrystals: Fabrication and Collective Intrinsic properties," *Accounts of Chemical Research,* vol. 40, pp. 685-693, 2007.

[14] S. Disch, E. Wetterskog, R. P. Hermann, G. Salazar-Alvarez, P. Busch, T. Brückel, L. Bergström and S. Kamali, "Shape Induced Symmetry in Self-Assembled Mesocrystals of Iron Oxide Nanocubes," *Nano Letters,* vol. 11, pp. 1651-1656, 2011.

[15] S. Sun, "Recent Advances in Chemical Synthesis, Self-Assembly, and Applications of FePt Nanoparticles," *Advanced Materials,* vol. 18, pp. 393-403, 2006.

[16] B. A. Korgel and D. Fitzmaurice, "Condensation of Ordered nanocrystal Thin Films," *Physical Review Letters,* vol. 80, pp. 3531-3534, 1998.

[17] T. P. Bigioni, X. M. Lin, T. T. Nguyen, E. I. Corwin, T. A. Witten and H. M. Jaeger, "Kinetically driven self assembly of highly ordered nanoparticle monolayers," *Nature Materials,* vol. 5, pp. 265-270, 2006.

[18] C. Antoniak, A. Warland, M. Darbandi, M. Spasova, A. Trunova, K. Fauth, E. F. Aziz, M. Farle and H. Wende, "X-ray absorption measurements on nanoparticle systems: self-assembled arrays and dispersions," *Journal of Physics D,* vol. 43, p. 474007, 2010.

[19] D. Mishra, *Structural and magnetic characterization of self-assembled magnetic nanoparticles,* Germany: PhD Thesis (Universität Bochum), 2012.

[20] R. Overney, *Nanoscience and molecular engineering,* USA: Vorlesungsmanuskript (University of Washington), 2010.

[21] E. Arunan, "Molecule Matters van der Waals molecules," *Resonance,* pp. 667-674, 2010.

[22] A. P. Guimaraes, Principles of Nanomagnetism, Brazil: Springer, 2009.

[23] C. P. Bean and J. D. Livingston, "Superparamagnetism," *Journal of Applied Physics,* vol. 30, pp. 120S-129S, 1959.

[24] K. Sato, T. Fukushima and H. Katayama-Yoshida, "Super-Paramagnetic Blocking Phenomena and Room-Temperature Ferromagnetism in Wide Band-Gap Dilute Magnetic Semiconductor (Ga, Mn)N," *Japanese Journal of Applied Physics,* vol. 46, pp. L682-L684, 2007.

[25] S. Soeya, "Distribution of blocking temperature in bilayered Ni81FE19/NiO films," *Journal of Applied Physics,* vol. 76, pp. 5356-5360, 1994.

[26] E. E. Carpenter, "Effects Of Shell Thickness on Blocking Temperature Of Nanocomposites Of Metal Particles With Gold Shells," *Transactions on Magnetics,* vol. 35, pp. 3496-3499, 1999.

[27] J. Dai, J. Q. Wang, C. Sangregorio, J. Fang, E. Carpenter and J. Tang, "Magnetic coupling induced increase in the blocking temperature of Gamma-Fe2O3 nanoparticles," *Journal of Applied Physics,* vol. 87, pp. 7397-7399, 2000.

[28] C. Radhakrishnamurty and S. D. Likhite, "Hipkinson effect, blocking temperature and Curie point in basalts," *Earth and Planetary Science Letters,* vol. 7, pp. 389-396, 1970.

[29] S. Bendanta, O. Petracic, X. Chen, J. Rhensius, E. Kentzinger, U. Rücker, T. Brückel, A. Doran, A. Scholl, S. Cardoso, P. P. Freitas and W. Kleemann, "Single-particle blocking and collective magnetic states in discontinuous CoFe/Al2O3 multilayers," *Journal of Physics D,* vol. 43, p. 474002, 2010.

[30] M. Suzuki, S. I. Fullem and I. S. Suzuki, "Observation of superspin-glass behavior in Fe3O4 nanoparticles," *Condensed Matter,* Vols. arXiv:cond-mat/0608297v4, 2008.

[31] S. A. Majetich and M. Sachan, "Magnetostatic interactions in magnetic nanoparticle assemblies: energy, time and length scales," *Journal of Physics D,* vol. 39, pp. R407-R422, 2006.

[32] O. Petracic, X. Chen, S. Bedanta, W. Kleemann, S. Sahoo, S. Cardoso and P. P. Freitas, "Collective states of interacting ferromagnetic nanoparticles," *Journal of Magnetism and Magnetic Materials,* vol. 300, pp. 192-197, 2006.

[33] Varón, M., M. Beleggia, T. Kasama, R. J. Harrison, R. E. Dunin-Borowski, V. F. Puntes and C. Frandsen, "Dipolar Magnetism in Ordered and Disordered Low-Dimensional Nanoparticle Assemblies," *Scientific Reports,* vol. 3, 2013.

[34] D. L. Leslie-Pelecky, "Magnetic Properties of Nanostructured Materials," *Chemistry of Materials,* vol. 8, pp. 1770-1783, 1996.

[35] P. J. Jensen and G. M. Pastor, "Low-energy properties of two-dimensional magnetic nanostructures: interactions and disorder effects," *New Journal of Physics,* vol. 5, pp. 68.1-68.22, 2003.

[36] J. B. Kortright, O. Hellwig, K. Chesnel, S. Sun and E. E. Fullerton, "Interparticle magnetic correlations in dense Co nanoparticle assemblies," *Physical Review B,* vol. 71, p. 012402, 2005.

[37] J. Lopes and Y. G. Pogorelov, "Indirect interactions between magnetic nanoparticles in granular alloys," *Journal of Magnetism and Magnetic Materials,* Vols. 272-276, pp. e1249-e1250, 2004.

[38] S. A. Sebt, A. Bakhshayeshi and M. R. Abilhassani, "Magnetic properties of core/shell nanoparticles with magnetic or nonmagnetic shells," *Journal of Statistical Mechanics: Theroy and Experiment,* vol. P09006, 2012.

[39] L. Wang, J. Luo, M. M. Maye, Q. Fan, Q. Rendeng, M. H. Engelhard, C. Wang, Y. Lin and C. J. Zhong, "Iron oxide-gold core shell nanoparticles and thin film assembly," *Journal of Materials Chemistry,* vol. 15, pp. 1821-1832, 2005.

[40] X. Teng and H. Yang, "Synthesis of Face-Centered Tetragonal FePt Nanoparticles and Granular Films from Pt@Fe2O3 Core-Shell Nanoparticles," *Jornal of the American Chemical Society,* vol. 125, pp. 14559-14563, 2003.

[41] X. Teng and H. Yang, "Synthesis of magnetic nanocomposites and alloys from platinum-iron oxide core-shell nanoparticles," *Nanotechnology,* vol. 16, pp. S554-S561, 2005.

[42] X. Teng, D. Black, N. J. Watkins, Y. Gao and H. Yang, "Platinum-Maghemite Core-Shell nanoparticles Using a Sequential Synthesis," *Nano Letters,* vol. 3, pp. 261-264, 2002.

[43] X. B. Zhang, J. M. Yan, S. Han, H. Shioyama and Q. Xu, "Magnetically Recyclable Fe@Pt Core-Shell Nanoparticles and Their Use as Electrocatalysts for Ammonia Borane Oxidation: The Role of Crystallinity of the Core," *Journal of the American Chemical Society,* vol. 131, pp. 2778-2779, 2009.

[44] L. T. Kuhn, A. Bojesen, L. Timmermann, M. M. Nielsen and S. Morup, "Structural and magnetic properties of core-shell iron-iron oxide nanoparticles," *Journal of Physics,* vol. 14, pp. 13551-13567, 2002.

[45] C. Antoniak, M. E. Gruner, M. Spasova, A. V. Trunova, F. M. Römer, A. Warland, B. Krumme, K. Fauth, S. Sun, P. Entel, M. Farle and H. Wende, "A guideline for atomistic design and understanding of ultrahard nanomagnets," *Nature Communications,* vol. 1538, 2011.

[46] A. Uheida, M. Iglesias, C. Fontàs, M. Hidalgo, V. Salvadó, Y. Zhang and M. Muhammed, "Sorption of palladium(II), rhodium(III), and platinum(IV) on Fe3O4 nanoparticles," *Colloid and Interface Science,* vol. 301, pp. 402-408, 2006.

[47] A. Ebbing, O. Hellwig, L. Agudo, G. Eggeler and O. Petracic, "Tuning the magnetic properties of Co nanoparticles by capping," *Physical Review B,* vol. 84, p. 12405, 2011.

[48] P. Gambardella, S. Rusponi, M. Veronese, S. S. Dhesi, C. Grazioli, A. Dallmeyer, A. Cabria, R. Zeller, P. H. Dederichs, K. Kern, C. Carbone and H. Brune, "Giant Magnetic Anisotropy of Single Cobalt Atoms and Nanoparticles," *Science,* vol. 300, pp. 1130-1133, 2003.

[49] E. Navarro, Y. Huttel, C. Clavero, A. Cebollada and G. Armelles, "Magnetic coupling between Fe nanoislands induced by capping-layer magnetic polarization," *Physical Review B,* vol. 69, p. 224419, 2004.

[50] F. Meier, S. Lounis, J. Wiebe, L. Zhou, S. Heers, P. Mavropoulos, P. H. Dederichs, S. Blügel and R. Wiesendanger, "Spin polarization of platinum (111) induced by the proximity to cobalt nanostripes," *Physical Review B,* vol. 83, p. 075407, 2011.

[51] Y. M. Lu, Y. Choi, C. M. Ortega, X. M. Cheng, J. W. Cai, S. Y. Huang, L. Sun and C. L. Chien, "Pt Magnetic Polarization on Y3Fe5O12 and Magnetotransport Characteristics," *Physical Review Letters,* vol. 110, p. 147207, 2013.

[52] S. Geprägs, S. Meyer, S. Altmannshofer, M. Opel, F. Wilhelm, A. Rogalev, R. Gross and S. T. B. Goennenwein, "Investigation of induced Pt magnetic polarization in Pt/Y3Fe5O12 bilayers," *Applied Physics Letters,* vol. 101, p. 262407, 2012.

[53] R. M. Cornell and U. Schwertmann, The Iron Oxides: Structure, Properties, Reactions, Occurences and Uses, Germany: Wiley, 2003.

[54] H. M. Lu and X. K. Meng, "Morin Temperature and Néel Temperature of Hematite Nanocrystals," *Journal of Physical Chemistry C,* vol. 114, pp. 21291-21295, 2010.

[55] A. P. C. Teixeira, J. C. Tristao, M. H. Araujo, L. C. A. Oliveira, F. C. C. Moura, J. D. Ardisson, C. C. Amorim and R. M. Lago, "Iron: a Versatile Element to Produce Materials for Environmental Applications," *Journal of Brazilian Chemistry,* vol. 23, no. 9, pp. 1579-1593, 2012.

[56] A. H. Morrish, Canted antiferromagnetism: hematite, USA: World Scientific Publishing Co. Pte. Ltd, 1994.

[57] S. P. Gubin (Ed.), Magnetic Nanoparticles, Germany: WILEY-VCH, 2009.

[58] M. A. Legodi and D. de Waal, "The preparation of magnetite, goethite, hematite and maghemite of pigment quality from mill scale iron waste," *Dyes and Pigments,* vol. 74, pp. 161-168, 2007.

[59] M. Allahmad and N. N. Moghaddam, "Synthesis of maghemite nanoparticles by thermal-decomposition of magnetite nanoparticles," *Material Science,* vol. 31, pp. 264-268, 2013.

[60] Y. Cudennec and A. Lecerf, "Topotactic transformations of goethite and lepidocrocite into hematite and maghemite," *Solid State Sciences,* vol. 7, pp. 520-529, 2005.

[61] M. Friák, A. Schindlmayr und M. Scheffler, „Ab initio study of the half-metal to metal transition in strained magnetite,“ *New Journal fo Physics,* Bd. 9, 2007.

[62] M. Yin, Z. Chen, B. Deegan and S. O'Brien, "Wüstite nanocrystals: Synthesis, structure and superlattice formation," *Journal of Materials Research,* vol. 22, pp. 1987-1995, 2007.

[63] C. A. McCammon and L. Liu, "The Effects of Pressure and Temperature on nonstoichiometric Wüstite, FexO: The Iron-rich Phase Boundary," *Physics and Chemistry of Minerals,* vol. 10, pp. 106-113, 1984.

[64] D. S. Tannhauser, "Conductivity in iron oxides," *Journal of Physics and Chemistry of Solids,* vol. 23, pp. 25-34, 1962.

[65] G. E. Kugel, B. Hennion and C. Carabatos, "Low-energy magnetic excitations in wustite (Fe1-x O)," *Physical Review B,* vol. 18, pp. 1317-1321, 1978.

[66] W. N. Unertl, Physical Structure, Netherlands: Elsevier, 1996.

[67] D. R. Askeland, P. P. Fulay and W. J. Wright, The Science & Engineering of Materials, USA: Cenage Learning Inc, 2010.

[68] S. Hunklinger, Festkörperphysik, Germany: Oldenbourg Wissenschaftsverlag GmbH, 2009.

[69] C. Kittel, Einführung in die Festkörperphysik, Germany: Oldenbourg Wissenschaftsverlag GmbH, 2006.

[70] T. Koyama, D. Chiba, K. Ueda, K. Kondou, H. Tanigawa, S. Fukami, T. Suzuki, N. Ohshima, N. Ishiwata, Y. Nakatani, K. Kobayashi and T. Ono, "Observation of the intrinsic pinning of a magnetic domain wall in a ferromagnetic nanowire," *Nature Materials,* vol. 10, pp. 194-197, 2011.

[71] D. Kölle, *Experimentalphysik V - Festkörperphysik,* Germany: Vorlesungsmanuskript (Universität Tübingen), 2003.

[72] H. Hattendorf, *Weichmagnetische Werkstoffe auf Ni-Fe-Basis,* Germany: VDM Report (ThyssenKrupp VDM GmbH).

[73] H. Daniel, Physik 2: Elektrodynamik, Relativistische Physik, Walter de Gruyter GmbH, 1997.

[74] N. Spaldin, Magnetic Materials: Fundamentals and Device Applications, UK: Cambridge University Press, 2003.

[75] J. A. Mydosh, Spin Glasses: An Experimental Introduction, UK: Burgess Science Press, 1993.

[76] F. C. Pu, Y. J. Vang and C. H. Shang, Aspects of Modern Magnetism - Lecture Notes of the Eighth Chinese International Summer School of Physics, China: World Scientific Publishing Co Pte Ltd, 1996.

[77] S. Blundell, Magnetism in Condensed Matter, USA: Oxford University Press, 2001.

[78] C. Kittel und H. Krömer, Thermodynamik, Germany: Oldenbourg Wissenschaftsverlag, 2013.

[79] M. Opel, *Magnetismus,* Germany: Vorlesungsmanuskript (TU München), 2003.

[80] Dzyaloshinsky, "A thermodynamic theory of "weak" ferromagnetism of antiferromagnetics," *Journal of Physics and Chemistry of Solids,* vol. 4, pp. 241-255, 1957.

[81] T. Moriya, "Anisotropic Superexchange Interaction and Weak Ferromagnetism," *Physical Review,* vol. 120, pp. 91-98, 1960.

[82] C. D. Hu, "The Dzyaloshinskii-Moriya interaction in metals," *Journal of Physics: Condensed*

Matter, vol. 24, 2012.

[83] C. Ederer and C. J. Fennie, "Electric-field switchable magnetization via the Dzyaloshinskii-Moriya interaction: FeTiO3 versus BiFeO3," *Journal of Physics: Condensed Matter,* vol. 20, p. 434219, 2008.

[84] P. O'Brian, Nanoscience: Nanostructures Through Chemistry, UK: The Royal Society of Chemistry, 2013.

[85] R. L. Stamps, "Mechanisms for exchange bias," *Journal of Applied Physics,* vol. 33, pp. 247-268, 2000.

[86] W. H. Meikelejohn and C. P. Bean, "New Magnetic Anisotropy," *Journal of Applied Physics,* vol. 102, pp. 1413-1414.

[87] K. J. M. Bishop, C. E. Wilmer, S. Soh and B. A. Grzybowski, "Nanoscale Forces and Their Uses in Self-Assembly," *small,* vol. 5, pp. 1600-1630, 2009.

[88] H. J. Butt and M. Kappl, Surface and Interfacial Forces, Germany: Wiley, 2010.

[89] P. Joos, Dynamic Surface Phenomena, Netherlands: Ridderprint, 1999.

[90] H. J. Butt, K. Graf and M. Kappl, Physics and Chemistry of Interfaces, Germany: Wiley, 2003.

[91] M. D. Eldridge, P. A. Madden and D. Frenkel, "Entropy-driven formation of a superlattice in a hard-sphere binary mixture," *Letters to Nature,* vol. 356, pp. 35-37, 1993.

[92] T. Keller und G. Wei, *Grundlagen der Rasterkraftmikroskopie,* Germany: Praktikumsmanuskript (Universität Jena), 2011.

[93] W. Daumann, *InP-Kurzkanal-Heterostruktur-Feldeffekttransistoren mit elektronenstrahldefinierten Gate-Kontakten,* Germany: PhD Thesis (Universität Duisburg-Essen), 2000.

[94] "TU Delft," [Online]. Available: http://www.tnw.tudelft.nl/index.php?id=33723&L=1.

[95] M. McElfresh, *Fundamentals of magnetism and magnetic measurements featuring Quantum Design's magnetic measurement system,* USA: Primer (Purdue University), 1994.

[96] P. J. Kelly and R. D. Arnell, "Magnetron sputtering: a review of recent developments and applications," *Vacuum,* vol. 56, pp. 159-172, 1999.

[97] B. A. Joyce, "Molecular beam epitaxy," *Reports on Progress in Physics,* vol. 48, pp. 1637-1697, 1985.

[98] *Ion Beam Sputtering: Practical Applications to Electron Microscopy,* USA: Applications Laboratory Report 91 (South Bay Technology Inc.).

[99] S. Laurent, D. P. M. Forge, A. Roch, C. Robic, L. V. Elst and R. N. Muller, "Magnetic Iron Oxide Nanoparticles: Synthesis, Stabilization, Vectorization, Physicochemical Characterizations and Biological Applications," *Chemical Reviews,* vol. 108, no. 6, pp. 2064-2110, 2008.

[100] A. K. Gupta and M. Gupta, "Synthesis and surface engineering of iron oxide nanoparticles for biomedical applications," *Biomaterals,* vol. 26, pp. 3995-4021, 2005.

[101] W. Wu, Q. He and C. Jiang, "Magnetic Iron Oxide Nanoparticles: Synthesis and Surface Functionalization Strategies," *Nanoscale Resolution Letters,* vol. 3, pp. 397-415, 2008.

[102] S. Ganguly and S. Chakraborty, "Sedimentation of nanoparticles in nanoscale colloidas suspensions," *Physics Letters A,* vol. 375, pp. 2394-2399, 2011.

[103] D. Mishra, D. Greving, G. A. B. Confalonieri, J. Perlich, B. P. Z. H. Toperverg and O. Petracic, "Growth modes of nanoparticle superlattice thin films".*arXiv:1307.4693.*

[104] P. Y. Yunker, T. Still, M. A. Lohr and A. G. Yodh, "Suppression of the coffee-ring effect by shape-dependent capillary interactions," *Nature,* vol. 476, pp. 308-3011, 2011.

[105] S. Singameneni, V. N. Bliznyuk, C. Binek and E. Y. Tsymbal, "Magnetic nanoparticles: recent advances in synthesis, self-assembly and applications," *Journal of Materials Chemistry,* vol. 21, pp. 16819-16845, 2011.

[106] R. D. Beegan, O. Bakajin, T. F. Dupont, G. Huber, S. R. Nagel and T. A. Witten, "Capillary flow as the cause of ring stains from dried liquid drops," *Nature,* vol. 389, pp. 827-829, 1997.

[107] S. W. J. Narayanan, "Dynamical Self-Assembly of nanocrystal Superlattices during Colloidal Droplet Evaporation by in situ Small Angle X-Ray Scattering," *Physical Review Letters,* vol. 93, p. 135503, 2004.

[108] F. Völklein und T. Zetterer, Praxiswissen Mikrosystemtechnik, Germany: Vieweg, 2006.

[109] H. Colina and P. Acker, "Drying cracks: Kinematics and scale laws," *Materials and Structures,* pp. 101-107, 2000.

[110] M. Li, S. Johnson, H. Guo, E. Dujardin and S. Mann, "A Generalized Mechanism for Ligand-Induced Dipolar Assembly of Plasmonic Gold Nanoparticle Chain Networks," *Advanced Functional Materials,* vol. 21, pp. 851-859, 2011.

[111] P. Ohara and W. M. Gelbart, "Interplay between Hole Instability and Nanoparticle Array Formation in Ultrathin Liquid Films," *Langmuir,* vol. 14, pp. 3418-3424, 1998.

[112] P. Ohara, J. R. Heath and W. Gelbart, "Self-Assembly of Submicrometer Rings of Particles from Solutions of Nanoparticles," *Angewandte Chemie International Edition,* vol. 36, pp. 1077-1080, 1997.

[113] R. Houghton, Emergency Characterization of Unknown Materials, USA: CRC Press, 2008.

[114] D. D. Ebbing and S. D. Gammon, General Chemistry: Media Enhanced Edition, USA: Houghton Mifflin Company, 2008.

[115] F. Li, D. P. Josephson and A. Stein, "Colloidal Assembly: The Road from Particles to Colloidal Molecules and Crystals," *Angewandte Chemie,* vol. 50, pp. 360-388, 2011.

[116] O. Petracic, "Superparamagnetic nanoparticle ensembles," *Superlattices and Microstructures,* vol. 47, pp. 569-587, 2010.

[117] J. E. T. Channell and C. McCabe, "Comparison of magnetic hysteresis parameters of unremagnetized and remagnetized limestones," *Journal Geophysical Research,* vol. 99, pp. 4613-4623, 1994.

[118] M. J. Benitez, O. Petracic, F. Schüth, H. Tüysüz and H. Zabel, "Fingerprinting the magnetic behavior of antiferromagnetic nanostructures using remanent magnetization curves," *Physical Review B,* vol. 83, p. 134424, 2011.

[119] M. Monínquez, D. Ortega, J. S. Garitaonandia, R. Litràn, C. Barrera-Solano, E. Blanco and M. Ramírez-del-Solar, "Magneto-Optic Faraday Effect in Maghemite Nanoparticles/Silica Matrix Nanocomposites," *Journal of Magnetism and Magnetic Materials,* vol. 320, pp. 725-729, 2008.

[120] J. R. Jeong, S. J. Lee, J. K. Kim and S. C. Shin, "Magnetic properties of Gamma-Fe2O3 nanoparticles made by coprecipitation method," *Physica Status Solidi,* vol. 241, pp. 1593-1596, 2004.

[121] D. Fiorani, A. M. Testa, F. Lucari, F. D'Orazio und H. Romero, „Magnetic properties of maghemite nanopartice systems: surface anisotropy and interparticle interaction effects," *Physica B,* Bd. 320, pp. 122-126, 2002.

[122] M. J. Benitez, D. Mishra, P. Szary, G. A. B. Confalonieri, M. Feyen, A. H. Lu, L. Agudo, G. Eggeler, O. Petracic and H. Zabel, "Structural and magnetic characterization of self-assembled iron oxide nanoparticle arrays," *Journal of Physics: Condensed Matter,* vol. 23, 2011.

[123] F. Walz, "The Verwey transition - a topical review," *Journal of Physics: Condensed Matter,* vol. 14, pp. R285-R340, 2002.

[124] R. Ramotowski, Lee and Gaensslen's Advances in Fingerprint Technology, 2013: CRC Press, France.

[125] Y. Bentor. [Online]. Available: http://www.chemicalelements.com/elements/pt.html.

[126] S. Wang, A. F. Khapikov, S. Brown and J. W. Harrell, "Thermal Effects on Delta-M Measurements in Magnetic Thin Films," *IEEE Transactions on Magnetics,* vol. 37, pp. 1518-1520.

[127] J. W. Harrell, S. Wang and H. Fujiwara, "Field step dependence of delta-M curves," *Journal of Applied Physics,* vol. 91, pp. 8605-8607, 2002.

[128] Y. Gao, X. W. Zhang, Z. G. Yin, J. B. Qu and N. F. Chen, "Magnetic Properties of FePt Nanoparticles Prepared by a Micellar Method," *Nanoscale Resolution Letters,* vol. 5, pp. 1-6.

[129] V. Repain, J.-P. Jamet, N. Vernier, M. Bauer, J. Ferré, C. Chappert, J. Gierak and D. Mailly, "Magnetic interactions in dot arrays with perpendicular anisotropy," *Journal of Applied Physics,* vol. 95, pp. 2614-2618.

[130] A. Ludwig, L. Agudo, G. Eggeler, A. Ludwig, A. D. Wieck and O. Petracic, "Interaction effects and transport properties of Pt capped Co nanoparticles," *Journal of Applied Physics,* vol. 113, p. 043917, 2013.

[131] P. E. Kelly, K. O'Grady, P. I. Mayo and R. W. Chantrell, "Switching Mechanisms in Cobalt-Phosphorus Thin Films," *IEEE Transactions on Magnetics,* vol. 25, pp. 3881-3883, 1989.

[132] J. Bartolomé, L. M. García, F. Bartolomé, F. Luis, F. Petroff, C. Deranlot, F. Wilhelm and A. Rogalev, "Magnetic properties of Co nanoparticle granular films capped with Pt," *Journal of*

Magnetism and Magnetic Materials, vol. 316, pp. e09-e11, 2007.

[133] M. Hayakawa, J. B. Cohen and T. B. Reed, "Measurement of the Lattice Parameter of Wustite at High Temperatures," *Journal of The American Ceramic Society,* vol. 55, pp. 160-164, 1972.

[134] C. R. Barry, *Electrostatic Force Directed Integration of Nanomaterials,* USA: PhD Thesis (University of Minnesota), 2008.

[135] E. Matijevic and M. Borkovec, Surface and colloid science, USA: Kluwer Academic / Plenum Publishers, 2004.

[136] L. Pauling and S. B. Hendricks, "The crystal structures of hematite and corundum," *Journal of the American Chemical Society,* vol. 47, pp. 781-790, 1925.

[137] U. Schwertmann and R. M. Cornell, Iron Oxides in the Laboratory, Germany, Switzerland: Wiley, 2000.

[138] R. G. Wells, "Microscopic Identification of Wustite In Presence of Other Oxides of Iron," *Analytical Chemistry,* vol. 26, pp. 715-717, 1954.

[139] Y. Lalatonne, J. Richardi and M. P. Pileni, "Van der Waals versus dipolar forces controlling mesoscopic organizations of magnetic nanocrystals," *Nature Materials,* vol. 3, pp. 121-125, 2004.

Appendix

A. Datasheet nanoparticles by Ocean NanoTech LLC

Ocean NanoTech, LLC
2143 Worth Lane, Springdale, AR 72764
Phone : (479) 751-5500; Fax: (479) 751-5502
E-mail: orders@oceannanotech.com

Cetificate of Analysis-Product ID

Catalog number:	SOR-20-0050
Product name:	Iron Oxide Nanocrystals with Oleic Acid Coating
Lot number:	010411
Solvent:	Toluene
Size tolerance:	±2.5 nm
Surface group:	Oleic Acid
Storage:	4-25°C
Shelf life:	6 months
Volume:	2 mL
Concentration:	25 mg/mL

Analysis

PROPERTY	SPECIFICATIONS	METHOD
IO Size	20 nm	TEM
Absorbance	N/A	Spectrophotometry

TEM Image

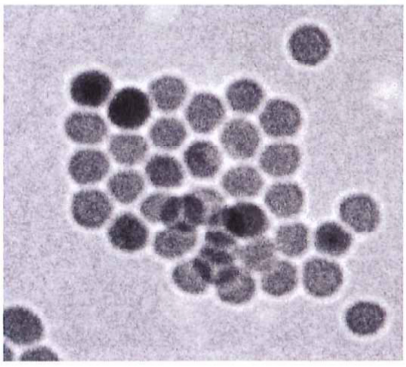

Absorption Spectra

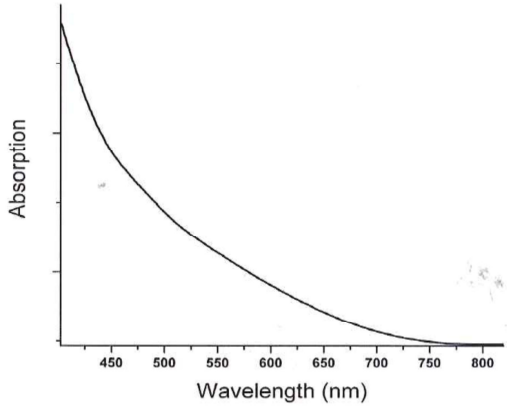

Signature: John DiXa

Date: 5-1-13

Disclaimer: For R&D only. Not intended for food, drug, household, agricultural, or cosmetic use. Ocean NanoTech, LLC shall not be held liable for any damage resulting from handling or contact with the above product.

B. Diamagnetic correction

Figure	Tangent slope
Figure 4.14a	-1.25e-9
Figure 4.14b	-1.3686e-9
Figure 4.14c	-1.154e-9
Figure 4.16a	-5.006759378e-9
Figure 4.16b	-5.325032991e-9
Figure 4.16c	-5.258355927e-9
Figure 4.17a	-4.87595041e-9
Figure 4.17b	-4.866985935e-9
Figure 4.17c	-4.796898752e-9
Figure 4.19a	-5,165457157e-9
Figure 4.19b	-5,259535678e-9
Figure 4.19c	-5,358436768e-9
Figure 4.20a	-5,330271541e-9
Figure 4.20b	-5,574589499e-9
Figure 4.20c	-5,562043128e-9
Figure 4.23a	-8,99262079e-10
Figure 4.23b	-5,598555684e-9
Figure 4.23c	-5,690422955e-9
Figure 4.24a	-5,334236546e-9
Figure 4.24b	-5,439769875e-9
Figure 4.24c	-5,142616946e-9
Figure 4.25a	-6.075653048e-9
Figure 4.25b	-6.396314062e-9
Figure 4.25c	-6.418433682e-9
Figure 4.27a	-7.618946464e-9
Figure 4.27b	-7.618746026e-9
Figure 4.27c	-7.694938377e-9
Figure 4.29a	-6.328487067e-9
Figure 4.29b	-6.387559317e-9
Figure 4.29c	-6.3311512851e-9
Figure 4.30a	-7,93759478e-9

Figure 4.30b	-7,792191428e-9
Figure 4.30c	-7,835950981e-9
Figure 4.33a	-5,909847747e-9
Figure 4.33b	-7,589366841e-9
Figure 4.33c	-6,076453413e-9
Figure 4.33d	-7,747624518e-9
Figure 4.33e	-6,3e-9
Figure 4.33f	-7,595494594e-9

C. Coercive field strength of hysteresis loops (5 K)

Figure	Coercive field [Oe]		Shift [Oe]
Figure 4.14	-1554	691	296.5
Figure 4.16	-2368	1491	438.5
Figure 4.17	-2252	1271	490.5
Figure 4.19	-2317	1710	303.5
Figure 4.20	-1052	458	297
Figure 4.23	-561	110	225
Figure 4.24	-1826	690	568
Figure 4.25	-613	394	109.5
Figure 4.27	-498	174	160
Figure 4.29	-637	368	134.5
Figure 4.30	-639	200	219,5
Figure 4.33e	-536	135	200,5
Figure 4.33f	-471	200	135,5